THE MORPHOLOGY AND KINEMATICS OF STAR FORMING REGIONS

ALISON M CRAIGON

DEPARTMENT OF PHYSICS
UNIVERSITY OF STRATHCLYDE

A thesis presented in fulfilment of the requirements for the degree of

DOCTOR OF PHILOSOPHY

2016

This thesis is the result of the author's original research. It has been composed by the author and has not been previously submitted for examination which has led to the award of a degree.

The copyright of this thesis belongs to the author under the terms of the United Kingdom Copyright Acts as qualified by University of Strathclyde Regulation 3.50. Due acknowledgement must always be made of the use of any material contained in, or derived from, this thesis.

Signed:

Date:

Patience and perseverance

ACKNOWLEDGEMENTS

I am grateful to all who have helped and encouraged me in the course of this PhD. In particular I thank my supervisor, Helen Fraser, for introducing me to astrochemistry and many amazing opportunities: presenting my work at conferences around the world, teaching undergraduate physics and performing experiments for the public at science festivals, which led me to develop an interest in science communication. I am indebted to Wing-Fai Thi and Bill Dent, my unofficial supervisors at the Royal Observatory Edinburgh, for their invaluable guidance in all aspects of observational astronomy and for introducing me to the work of Edward Tufte, whose books on data visualisation have been an inspiration.

I also thank my fellow students at Strathclyde and across SUPA who made my PhD a memorable experience, especially Jenny with whom I shared many interesting discussions and amazing conference trips.

I learned a great deal from the members of the Astronomical Society of Glasgow (2007 - 2013); 'amateur' astronomers in the best sense of the word. Their passion for astronomy enthuses all who attend their events and I remember my time with them fondly.

My colleagues at Shaw Pipeline Services (2010 - 2013) and Sonomatic (2013 - 2016), with whom I began my career in industry, were supportive of my ongoing PhD work. Meanwhile, my postgraduate tutors and viva committee have been understanding of the challenges involved in completing a thesis while establishing a career in a different field.

Special thanks to Mum and Dad, who have always encouraged and supported me in pursuing this ambition, and others. My family and friends who wished me success in this PhD have helped me more than they know.

Finally, I thank Doug for his love, support and unwavering confidence in my ability to complete this thesis. What will we do with all the free time I have now?

ABSTRACT

To develop a complete picture of the early stages of star and planet formation, it is necessary to understand the molecular clouds from which they form. The physical properties of these clouds and the interactions between their gas and solid constituents are not well known. This thesis presents an observational study of the morphology and kinematics of carbon monoxide (CO) gas in molecular clouds. It forms part of a wider project to produce the first coupled gas-solid maps of a broad sample of starless and star forming clouds.

Nine molecular clouds were observed with the James Clerk Maxwell Telescope, the Institut de Radio Astronomie Millimétrique 30 m Telescope and the Nobeyama 45 m Radio Telescope to produce large scale (14.6×14.6 arcmin), high resolution (15.3 arcsec) maps of CO emission.

The COROLINE software was developed to derive maps from the observations which show how the CO gas is distributed; the temperature and density structures of the clouds; and how the morphology and kinematics of CO gas is influenced by embedded and nearby stars.

A comprehensive analysis is made of Barnard 35A: a cloud heavily processed both internally by a young stellar object and externally by massive stars. The temperature, density and velocity structures of this cloud are explored in detail. Observational evidence is proposed for photoelectric heating through a correlation between the gas temperature and emission from PolyAromatic Hydrocarbons. A clump of enhanced emission ahead of a Herbig–Haro object is thought to be due to photodesorption of CO ice from the surface of dust grains. A chain of similar clumps, following an arc equidistant from the YSO, suggest that the outflow is precessing. This work concludes with the first coupled gas-solid maps.

This thesis demonstrates the importance of understanding the often complex morphology and kinematics of a star forming region prior to considering the interactions between its gas and solid-phase species.

CONTENTS

LIST OF FIGURES

List of Tables

CHAPTER 1

INTRODUCTION

SYNOPSIS

This chapter begins by describing the astronomical objects and chemical mechanisms referred to in subsequent chapters. It then introduces the 'gas-solid mapping project', which aims to better understand the early stages of star formation by defining the physical and chemical conditions in a sample of starless and star forming molecular clouds. Using observational astrochemistry to probe the composition and evolution of molecular clouds provides important insights into the formation of stars, disks and their constituents from which planets form and on which life may someday arise.

Three key questions are addressed in this thesis for the sample of molecular clouds observed for the gas-solid mapping project:

- *How is CO gas distributed?*
- *What are the temperature and density structures?*
- *How are the morphology and kinematics of CO gas influenced by embedded and nearby stars?*

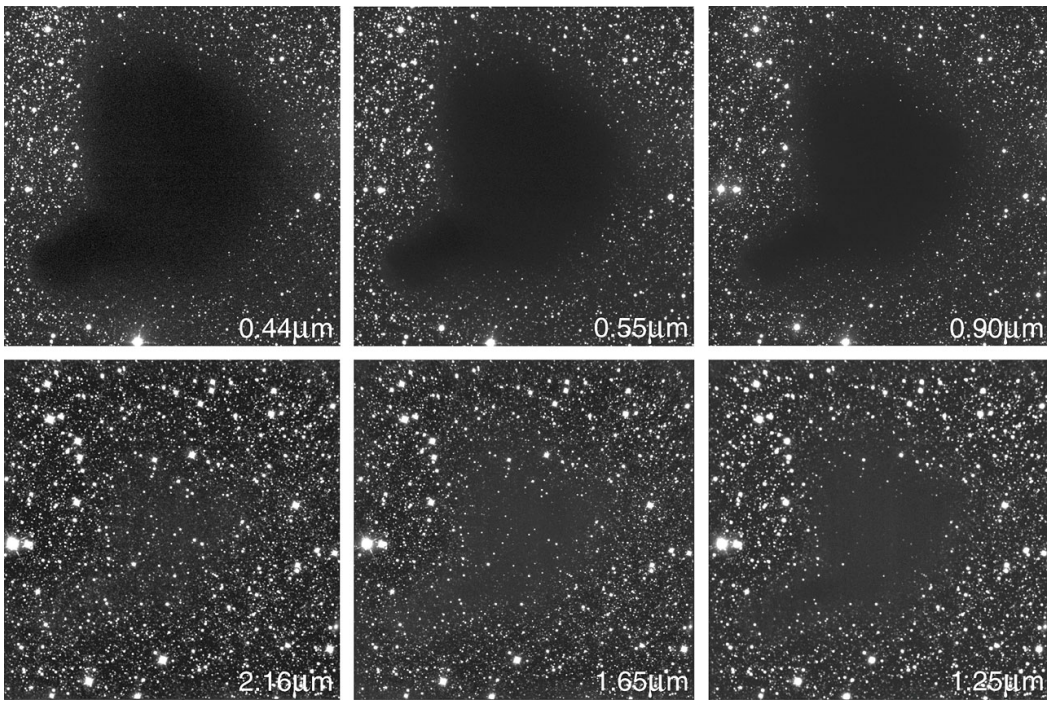

FIGURE 1.1. Dark nebula Barnard 68 imaged at six wavelengths. The short wavelength light from background stars is obscured by dense cloud, while longer wavelengths penetrate the dust and gas. The upper three frames were obtained using the FORS1 instrument at the VLT ANTU telescope and the lower three with SOFI at the NTT through near-infrared filters. Image credit: ESO PR Image eso9934b.

1.1 MOLECULAR CLOUDS

William Herschel's 1785 paper, 'On the Construction of the Heavens', describes his observation of a dark region devoid of stars in the constellation of Scorpius: 'in the body of the Scorpion there is an opening, or hole' (Herschel, W., 1785). E. E. Barnard observed a similar dark feature while photographing the great nebula of ρ Ophiuchi in 1910 but noted that 'the thinning out ... of stars in this region ... is not due to a chance vacancy', the nebula 'seems to show a veiling of the stars' (Barnard, 1910). He correctly identified these 'starless' regions as dark nebulae: dense clouds of gas and dust blocking the light from more distant stars. Fig. 1.1 shows Barnard 68, one of the most studied dark nebulae in his catalogue (Barnard, 1927). It is opaque at visible wavelengths but background stars can be seen in the near-infrared images (0.90 – 2.16 µm). Dark nebulae are also referred to as 'molecular clouds' and are now known to be sites of star formation.

1.1.1 PHYSICAL PROPERTIES

The space between the stars is known as the InterStellar Medium (ISM). Molecular clouds are regions of the ISM characterised by cold ($\sim$10 K), dense molecular gas. They range in size from small isolated Bok globules (Bok & Reilly, 1947) with radius 0.2 – 1 pc to Giant Molecular Clouds (GMCs) $\sim 10^2$ pc (Grabelsky et al., 1988) which extend over a large fraction of a constellation. Bok globule densities are typically 10^3 cm^{-3} and masses are 5 – 50 $M_\odot$. Embedded dense cores have size and mass approximately 10 per cent of the host globule and density $\sim 10^7$ cm^{-3} (Launhardt et al., 2010). GMCs and their cores have densities similar to Bok globules but their masses range from 10^3 – 10^7 $M_\odot$ (Murray, 2011).

1.1.2 COMPOSITION

Molecular hydrogen (H_2) is by far the most abundant molecule in the ISM. It dominates the gas-phase with $\sim$90 per cent by number density and $\sim$75 per cent by mass. At present, the Cologne Database for Molecular Spectroscopy reports that almost 200 different molecules have been detected in the ISM or circumstellar shells. Most of these species are found in the gas-phase.

Carbon monoxide (CO) is the second most abundant gas-phase species in molecular clouds (H_2/CO = 10^4 – 10^5) and is a good tracer of cold gas. It forms the basis of this thesis and is discussed further in Section 1.3.1. Other less abundant species, such as NH_3, CS, H_2D^+ and N_2H^+, are used to probe the densest regions of molecular clouds (e.g Taylor et al. (1996), Roberts & Millar (2007)).

Around 1 per cent of the mass of molecular clouds is dust. It is mainly composed of silicates and carbonaceous compounds, which condensed in the atmospheres of red-giant stars and carbon stars and were subsequently ejected into the ISM by stellar winds. The particles range in size from large molecules to small grains the size of smoke particles (Fig. 1.2).

Dust grains are the primary site of interstellar molecule formation. The low temperatures and relatively high pressures in molecular clouds allow gas-phase atomic and molecular species to condense onto the surface of dust grains, forming an icy mantle. Water ice was first observed in the 1970s (Gillett & Forrest, 1973); since then a range of solid molecular species has been discovered including CO, CO_2, CH_3OH, CH_4,

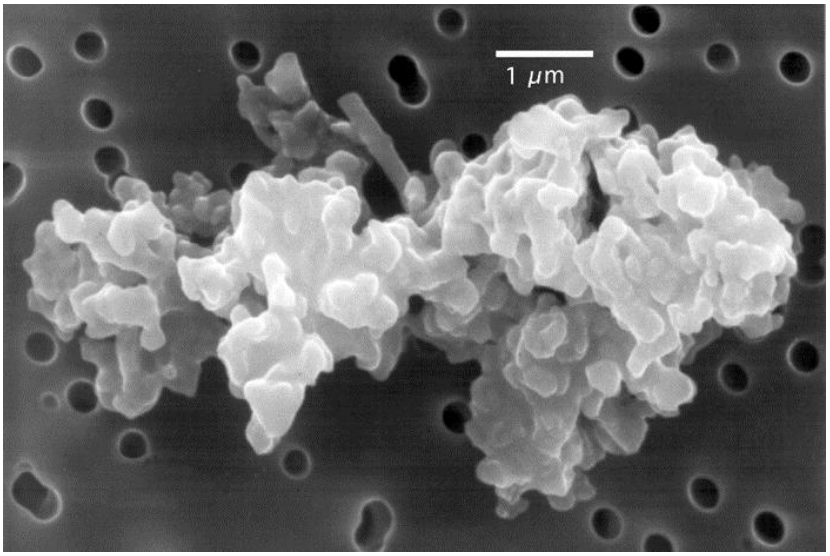

FIGURE 1.2. A scanning electron microscope image of an interplanetary dust grain, thought to be similar to interstellar dust grains found in molecular clouds. Its rough structure indicates formation from a cluster of submicron-sized grains. Image credit: Donald E. Brownlee, University of Washington, Seattle, and Elmar Jessberger, Institut für Planetologie, Münster, Germany.

NH_3, H_2CO, HCOOH, SO_2 and OCS (e.g. Gerakines et al. (1999), Nummelin et al. (2001), Pontoppidan et al. (2003), Gibb et al. (2004), Knez et al. (2005), Boogert et al. (2008), Öberg et al. (2008)). The composition of these icy mantles is modified through processing by various mechanisms such as ultraviolet (UV) and cosmic ray irradiation, catalysed formation of molecular species and desorption into the gas-phase.

The existence of dust grains and their icy mantles is inferred by their influence on starlight. In dark nebulae dust absorbs and scatters light from background stars causing total or wavelength-selective extinction (dimming, e.g Fig. 1.1). The grains and ice absorb background starlight in specific silicate and ice bands, giving insights into the composition of the grains and their icy mantles (e.g. Noble et al. (2013)). In reflection nebulae foreground starlight is reflected by dust grains, lighting up the nebula. This was first noted by Slipher (1912) following observations of the Pleiades.

Dust grains in molecular clouds are also detected directly at mid- to far-IR wavelengths from thermal continuum emission where they are in radiative equilibrium with the local radiation field. Heated grains also show a range of IR emission bands, although many have not yet been positively identified. Dust emission is discussed further in Section 1.3.2.

1.2 STAR FORMATION

Figs. 1.3 & 1.4 illustrate the vast extent of the GMC complex in the Orion constellation. Areas of ionized atomic hydrogen (H II) are traced by hydrogen-alpha (Hα) emission, shown in red. A feature, once described by Ptolemy as 'the mistiness in Orion's head' (Ptolemy, 144), appears at the top of Fig. 1.3. It is now named after λ Orionis, the group of massive stars at its centre which ionize the region. The λ Orionis region contains several bright-rimmed clouds including Barnard 35A, which is found at its eastern (left) edge. This object is explored in detail in Chapters 4 and 5. The Orion GMC is also home to many dark nebulae including the well known Horsehead Nebula (Barnard 33) which lies just south of Alnitak, the easternmost of the belt stars. Further south of the belt stars, in the sword, is the Orion Nebula. It is one of the brightest sites of star formation in the constellation and can be seen with the naked eye. Located at a distance of 1425 $\pm$ 62 light-years (Hirota et al., 2007), it has been well studied and found to contain stars at various stages of evolution (e.g. Clarke (2012), Mann et al. (2014), Safron et al. (2015)).

Fig. 1.5 describes the four stages of low mass star formation. They are known as Class 0 to Class III Young Stellar Objects, or YSOs, (Lada & Wilking (1984), Lada (1987), Shu et al. (1987), Andre et al. (1993), Andre & Montmerle (1994)). These classifications are based on the shapes of the Spectral Energy Distributions (SEDs); graphs of the energy emitted by the YSO as a function of wavelength. The SED slope is used to define the class of an object.

Star formation begins in a cold (10 – 20 K), dense molecular core when turbulent motions and magnetic fields dissipate, allowing it to collapse (Fig. 1.5a). Alternatively, triggered star formation can occur when a molecular cloud is perturbed by an external force (e.g. nearby massive stars or supernovae) and becomes gravitationally unstable. Inhomogeneities can cause the cloud to fragment, resulting in several collapsing cores.

There are three stages of collapse. The first is the isothermal phase where the temperature is low ($\sim$ 10 K) and the density is tenuous. The contraction continues as the energy escapes by thermal emission at far-IR and submillimetre wavelengths and the temperature remains low. During the adiabatic phase the density and opacity increase until it becomes opaque and the energy released by contraction cannot radiate out. The contraction stops when the temperature rises high enough to balance the gravitational collapse. When this hydrostatic equilibrium is reached it becomes a 'protostar' and is

FIGURE 1.3. An image by Rogelio Bernal Andreo (DeepSkyColors.com) showing the many nebulae and star forming regions in the Orion constellation including the Horsehead Nebula and Orion Nebula below the belt stars, the giant arc of Barnard's Loop on the left and the large circular λ Orionis region containing B35A at the head. The image is a mosaic of broadband telescopic images with additional Hα images tracing the ionized atomic hydrogen.

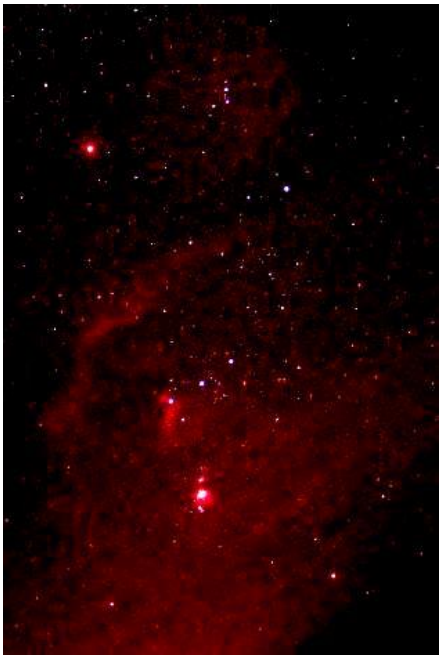

FIGURE 1.4. An image of Orion taken in Scotland by astrophotographer Douglas Cooper and the author using an Hα filter to trace the ionized atomic hydrogen.

classified as a Class 0 YSO (Fig. 1.5b). This stage lasts around 10^4 yr and involves the accretion of most of the mass that will form the star. The SED shows only long wavelength emission from the dust and gas in the cloud.

The core spins slowly and as it collapses the rotational velocity increases due to conservation of angular momentum. The rotation opposes collapse perpendicular to the rotation axis so the core flattens to a disk with a central bulge and it becomes a Class I YSO (Fig. 1.5c). Mass transfers onto the central object more slowly during this phase, spiralling in through the accretion disk. The angular momentum and gravitational energy of the infalling material is released by bipolar jets, which eject material perpendicular to the disk. The age of the YSO is around 10^5 yr. Although the SED is still dominted by dust and gas emission, the central object is also evident at shorter wavelengths. The dip in the SED at around 10 μm is due to absorption by silicates in the dust.

Accretion slows further in Class II YSOs (Fig. 1.5d). These objects are also known as 'Classical T Tauri stars', named after their prototype: T Tauri. The cloud begins to clear and clumps of dust may start to collide and stick in the inner region of the disk. The age of the YSO is around 10^6 yr and most of the emission in the SED comes from the central object, although the optically thick disk is also evident.

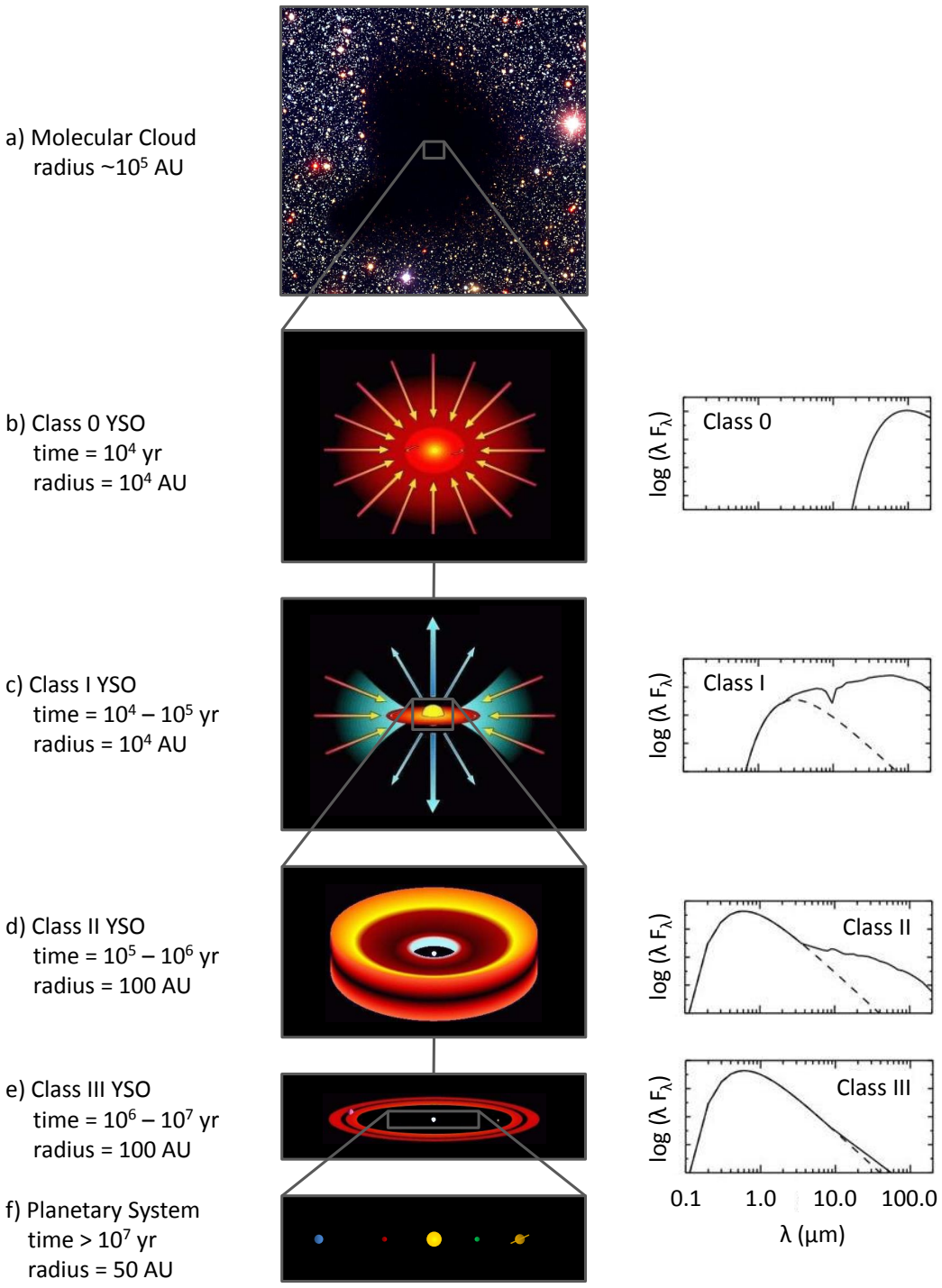

FIGURE 1.5. The stages of low mass star formation. a) Stars form in dense cores within molecular clouds. b) The cores collapse when gravity overcomes the internal gas pressure. c) Rotation causes the dust and gas to flatten into a disk and bipolar jets release the angular momentum of the accreted material. d) Accretion slows and the cloud clears. e) Accretion stops and collisions between dust particles form planetesimals. f) Nuclear fusion begins and the planetesimals reach the size of planets. Plots show the spectral energy distributions for each class of YSO; the dashed line indicates the contribution from the central object. Figure adapted from Isella (2006).

Class III YSOs (or 'Weak-Lined T Tauri stars') have started developing internally and do not accrete new material. Collisions between dust particles in the disk form planetesimals which then grow as they continue to encounter and accrete other material. The accretion disk has become a protoplanetary disk (Fig. 1.5e). The age of the YSO is 10^6 – 10^7 yr and the SED of this final stage is dominated by the central object but shows a small contribution from the optically thin disk.

It is important to note that the physical interpretation of the SED slope is the degree of embeddedness of the central object within the natal cloud. The accuracy of the ages associated with the classes can be affected by various factors including: binarity, rotation rate, accretion rate and the inclination of the system to the line of sight (i.e. an edge-on Class III may appear like a Class II).

The continuing gravitational pressure compresses the central object. When the temperature becomes high enough, nuclear fusion begins and the star is born. The ongoing aggregation of planetesimals results in objects the size of planets. The region around the star is swept clean and a planetary system, like our solar system, is formed after around 10^7 yr (Fig. 1.5f).

The low mass star continues to evolve and in the final stage of its life expels its outer layers in an expanding shell of low density gas known as a planetary nebula. This term was coined in 1785 by William Herschel who discussed their resemblance to planets, nebulae and stars but concluded that they could not be classified as any of these heavenly bodies (Herschel, W., 1785). The planetary nebula enriches the ISM with material that will go on to form the next generation of stars.

1.2.1 MOLECULAR OUTFLOWS

Since their discovery 35 years ago (Snell et al., 1980), molecular outflows in the region of YSOs have proved to be a common phenomenon, with several hundred identified so far (Wu et al., 2004). Highly collimated molecular outflows form in young low-mass systems where YSO bipolar jets, which have speeds of 100 – 300 kms^{-1} and densities of order 10^3 cm^{-3}, entrain the molecular gas and accelerate it along their length (e.g. Richer et al. (1992), Bachiller et al. (1995), Narayanan et al. (2012)). Wide angle winds are also important drivers of outflows. Arce & Sargent (2006) demonstrated that the outflow opening angle widens during the evolution of the YSO. Various models have been suggested to explain the range of observed outflow morphologies and kinematics

Arce et al. (2007).

Outflows can significantly affect their parent clouds as they carve out cavities and add energy and momentum into the surrounding medium (e.g. Shu et al. (2000), Bally et al. (2007)). The clearing out of dust and gas can terminate the YSO infall stage (Velusamy & Langer, 1998) and influence the star formation efficiency of the cloud (Matzner & McKee, 2000).

Molecular outflows are easily identified in maps of CO emission, where the gas velocity is shifted with respect to the cloud velocity. This is explored in detail in Chapter 5. Although it is a good method for determining the physical parameters of the outflows, several uncertainties are unavoidable. Firstly, the outflow and quiescent cloud emission often appear as a double-peaked line profile, which can be difficult to accurately separate. Secondly, as the observations can only detect the velocity component in the line-of-sight, a correction must be made for the estimated inclination angle of the outflows. Thirdly, the CO/H_2 ratio in shocked regions is not well known which introduces uncertainty into the mass estimate.

Typical molecular outflows have lengths ranging from less than 0.1 pc to several pc, velocities from a few km s^{-1} to a few 10^2 km s^{-1} and masses between 10^{-4} $M_\odot$ and 10^2 $M_\odot$ (Arce et al., 2007).

1.2.2 HERBIG–HARO (HH) OBJECTS

When high velocity bipolar jets collide with the surrounding molecular cloud, the shock causes strong atomic line emission. These regions are known as Herbig–Haro (HH) objects, after astronomers George Herbig and Guillermo Haro. Fig. 1.6 shows the Carina Nebula containing both molecular outflows and HH objects (HH 901 and HH 902) with their classic bow-shock structure. HH objects are ubiquitous in star forming regions and several may be associated with a single YSO, forming a bright string along the outflow. Over 400 HH objects, or groups of objects, have been catalogued (Reipurth, 2000).

HH object shocks compress and heat the gas and induce gas-phase chemical reactions, modifying the chemistry of the region. Atoms and molecules are also ejected from dust grains, enhancing gas-phase abundances in shocked regions (e.g. Tielens (1999)). Clumps of enhanced HCO^+ and NH_3 emission have been observed ahead of HH objects (e.g. Rudolph & Welch (1988), Torrelles et al. (1992), Girart et al. (1994)).

FIGURE 1.6. Bipolar outflows and HH objects (HH 901 and HH 902) in the Carina Nebula. This image is a combination of Hubble observations using three WFC3 filters: blue - 502 nm [OIII]; green - 657 nm Hα & [N II]; red - 673 nm [S II]. Image credit: NASA, ESA, M. Livio and the Hubble 20th Anniversary Team (STScI).

However, these clumps are cold ($\sim$10 K) and quiescent, showing no sign of shocks. It is thought that UV radiation from the HH object shock causes icy mantles to be released from dust grains into the gas-phase, a process called photodesorption. Studying enhanced emission for a range of species can provide insights into the nature of both solid and gas-phase species in molecular clouds. These clumps are likely to be transient as the bipolar jets will reach them within a timescale of the order of 10^4 yr or less Raga & Williams (2000). An HH object and enhanced clumps of CO emission are investigated in Chapter 5.

1.2.3 PHOTODISSOCIATION REGIONS (PDRS)

Groups of hot, massive stars of type 'O' and 'B' form in GMCs, such as the λ Orionis OB association shown in Fig. 1.3. Their energetic stellar winds disperse the surrounding molecular cloud and UV radiation ionizes the gas, forming an H II region

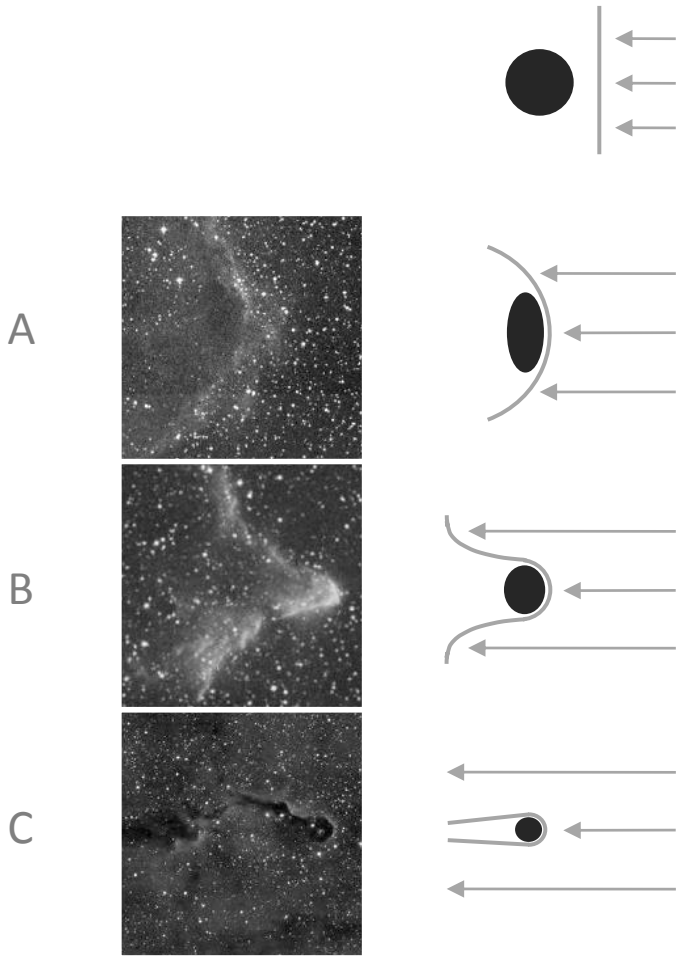

FIGURE 1.7. The evolution of bright-rimmed cloud morphologies (adapted from De Vries et al. (2002)). The first diagram shows a dense clump with a planar shock approaching from the right. The shock front then slows as it hits and flattens the clump, forming a type-A cloud. The dense region contracts as the shock passes, resulting in a type-B morphology and protecting the gas behind from ionization. The contraction continues, forming a type-C (or cometary) bright-rimmed cloud.

(or Strömgren sphere). PhotoDissociation regions (PDRs) are found at the boundary between the H II region and molecular cloud, where the heating and chemistry are controlled by far-ultraviolet photons (6 eV $<$ hν $<$ 13.6 eV) (Hollenbach & Tielens, 1999).

'Bright-rimmed' molecular clouds (BRCs) are so called due to the emission from a PDR along one edge. Their morphologies are split into three categories, with 'Type A' describing the shape of a cloud with a moderately curved rim where the ionization front has collected the gas into a ridge. It is thought that type A clouds will continue to

evolve, with the curved rim becoming tighter, leading to type B and C clouds (Ogura & Sugitani, 1998). A schematic of this evolution is shown in Fig. 1.7 (based on Fig.1. of De Vries et al. (2002)). Sugitani et al. (1991) conducted a survey of 44 bright-rimmed clouds and classified them according to their rim morphology.

This thesis focuses on Barnard 35A (B35A), a type A bright-rimmed cloud (BRC) found within the Strömgren sphere of the λ Orionis (λ Ori) OB association. It is also known as B35, BRC18, SFO18 and L1594. Chapter 4 explores its PDR.

1.3 OBSERVATIONAL TRACERS OF STAR FORMING REGIONS

Although molecular clouds are dominated by H_2 gas, it is difficult to detect. The symmetry of the homonuclear H_2 molecule means that the centre of mass and centre of charge coincide so it has no permanent electric dipole moment (Fig. 1.8). The low mass of the protons and small size of the molecule also give it a low moment of inertia. It requires a temperature of 511 K to excite it above its ground rotational state for the $J = 2 \rightarrow 0$ transition ($\Delta J = 1$ is forbidden for H_2). The low temperature of the cloud ($\sim$10 K) means that very few H_2 molecules are excited into that state. CO, the second most abundant gas-phase species, has neither of these issues.

1.3.1 CARBON MONOXIDE

The majority of species observed in molecular clouds form in the solid-phase on the surface of dust grains. CO is one of very few which form in the gas-phase and subsequently freeze-out on dust grains. It has a relatively high abundance in both gas and solid-phases.

CO has a strong triple bond and dipole moment that make it both chemically stable and easily observed in the gas-phase. These observations can be used to infer the H_2 column density since the CO/H_2 fractional abundance is around 10^{-4}. A range of environments within a molecular cloud can be investigated by observing three CO isotopologues: ^{12}CO, ^{13}CO and C^{18}O. Emission from the most abundant isotopologue, ^{12}CO, traces the optically thick cloud surface. ^{13}CO is less abundant which means that emission from deeper in the cloud is observable. The least abundant of the three isotopologues, C^{18}O, probes even deeper into the dense regions of the cloud.

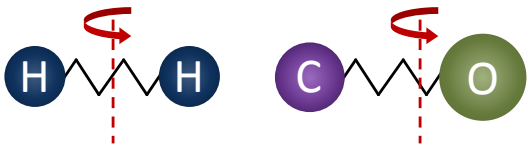

FIGURE 1.8. The rotation of H_2 and CO molecules about their centre of mass. For H_2, the centre of charge coincides with the centre of mass and it has no dipole moment.

CO is a simple diatomic molecule with a permanent electric dipole moment. When the molecules transition from a high rotational energy level to a lower one, energy is released. This CO emission is one of the primary cloud coolants and is observed at defined frequencies. The rotational energy levels for CO are given by,

$$E_{\rm J} = {\rm B}J(J+1) \qquad J = 0, 1, 2, ..., \tag{1.1}$$

where J is the rotational quantum number and B is the rotational constant for the particular CO isotopologue.

$${\rm B} = \frac{{\rm h}^2}{8\pi^2 I}, \tag{1.2}$$

where h is Planck's constant and I is the moment of inertia,

$$I = \mu r^2, \tag{1.3}$$

r is the bond length and μ is the reduced mass of the molecule,

$$\mu = \frac{m_1 m_2}{m_1 + m_2}. \tag{1.4}$$

The selection rule for energy level transitions in rotational spectroscopy is $\Delta J = \pm 1$. Fig. 1.9 shows the energy levels for CO rotational transitions $J = 3 \rightarrow 2$, $J = 2 \rightarrow 1$ and $J = 1 \rightarrow 0$.

CO is an excellent tracer of the gas morphology and kinematics in molecular clouds, and indeed in a wide variety of astrophysical environments. For example: Dame et al. (2001) made a composite CO survey of entire Milky Way; Najita et al. (2003) surveyed CO emission from T Tauri stars; Greve et al. (2005) conducted interferometric

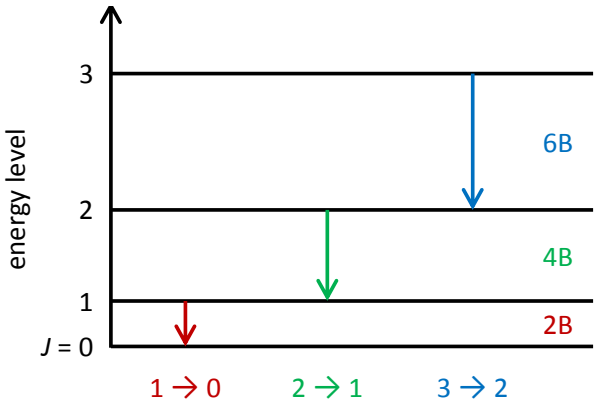

FIGURE 1.9. The rotational energy levels for the CO transitions $J = 1 \rightarrow 0$, $J = 2 \rightarrow 1$ and $J = 3 \rightarrow 2$.

CO observations towards galaxies; Huggins et al. (2005) detected CO in 40 planetary nebulae; Oka et al. (2007) surveyed CO towards the Galactic centre; Narayanan et al. (2008) observed CO towards quasars; and Salak et al. (2014) mapped CO in a nearby starburst galaxy. Several large scale CO surveys have also been conducted. The COMPLETE Survey Goodman (2004) mapped ^{12}CO and ^{13}CO for the Perseus, Ophiuchus and Serpens regions to provide data complementary to the *Spitzer* Legacy Program 'From Molecular Cores to Planet Forming Disks' (c2d) (Evans et al., 2003). The Gould Belt Survey also obtained CO maps, in 3 isotopologues, of a large typical sample of pre-stellar and star forming sources (Ward-Thompson et al., 2007).

In the solid-phase CO is postulated as the key source of carbon, and a precursor necessary for the formation of CO_2; a molecular ice ubiquitous in star forming regions (Fraser et al. (2004), Bergin et al. (2005)). In the gas-phase CO reacts with H_3^+ to form HCO^+; a key tracer of cold dense gaseous material in pre-stellar cores (Di Francesco et al., 2002). As CO gas is depleted, the HCO^+ abundance also falls and the reaction $N_2 + H_3^+ \rightarrow N_2H^+$ dominates and N_2H^+ becomes the key density tracer. Eventually even N_2H^+ is depleted (van der Tak et al., 2005) and the only remaining tracer molecule of cold dense gas is H_2D^+ (Hogerheijde et al., 2006).

1.3.2 POLYAROMATIC HYDROCARBONS (PAHS)

PolyAromatic Hydrocarbons (PAHs) are planar molecules composed of hexagonally arranged carbon atoms with peripheral hydrogen atoms. Fig. 1.10 illustrates the grouping of PAHs to form clusters and platelets, which then randomly combine to create

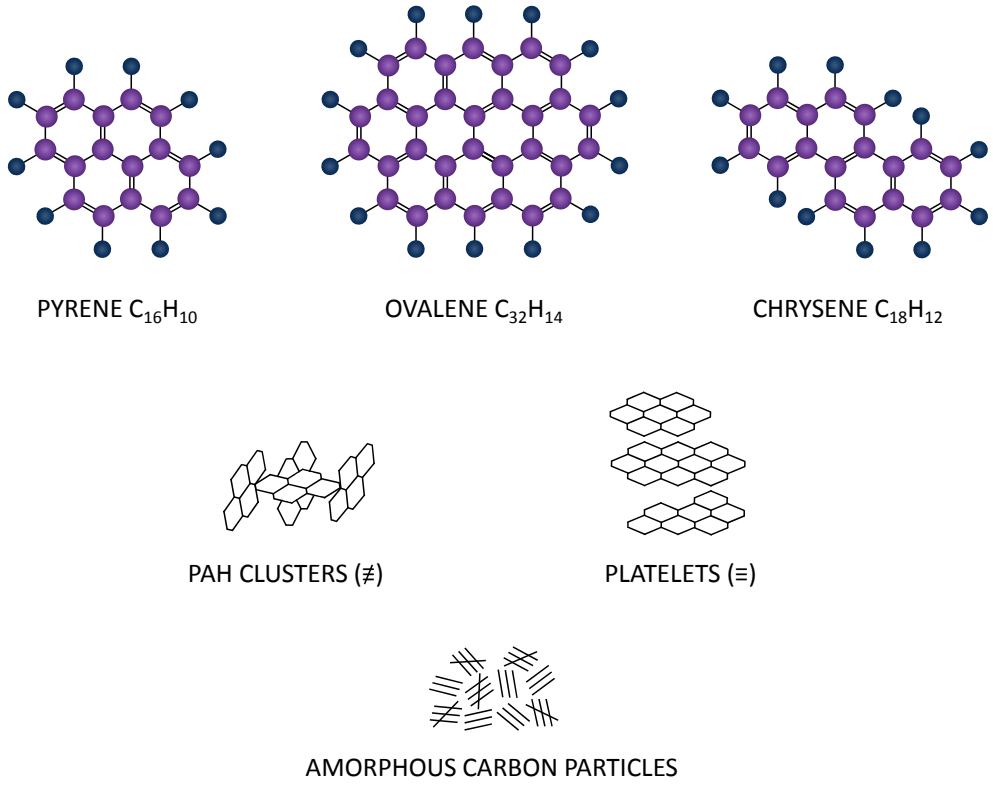

FIGURE 1.10. The link between individual PAH molecules and amorphous carbon particles. Multiple PAH molecules join together to form clusters or platelets, which then combine in random orientations to create amorphous carbon particles. Figure adapted from Allamandola et al. (1989).

soot-like amorphous carbon particles. PAHs are ubiquitous in the ISM and abundant. More than 20 per cent of the carbon in the universe is thought to be tied up in PAHs. They play a major role in the ionization balance and gas heating in molecular clouds, influencing the chemical processes in these regions (Tielens, 2008).

The stretching and bending vibrations of PAHs produce IR emission features at 3.3, 6.2, 7.7, 8.6 and 11.3 μm (Allamandola et al., 1989). The exact wavelength of PAH emission depends on the number of neighbouring hydrogen atoms, so each mode covers a range of wavelengths. The C-C stretching modes (7.6 and 7.8 μm) and the C-H in-plane bending modes (8.6 μm) (Tielens, 2005), shown in Fig.1.11, are particularly relevant to the analysis in Chapter 4. PAH cations greatly enhance the emission in the 8 μm band since the strength of the C-C stretching modes is an order of magnitude higher than that of the neutral PAH molecules (Tielens, 2008).

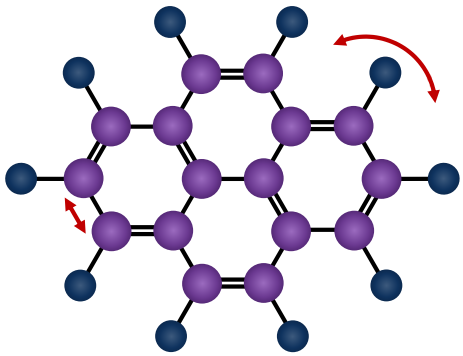

FIGURE 1.11. Pyrene, a small PAH molecule, illustrating the C-C stretching mode (seen at 7.6 and 7.8 μm) and the C-H in-plane bending mode (seen at 8.6 μm).

1.4 CHEMICAL MECHANISMS IN STAR FORMING REGIONS

1.4.1 ADSORPTION AND DESORPTION

In cold dense clouds, gas-phase CO molecules collide with and stick to small dust grains, producing a layer of CO ice on these submicron-sized particles Boogert & Ehrenfreund (2004). Chemical models of this adsorption process have determined that ice mantle growth is very efficient and would result in the freeze-out of all gas-phase molecules (except H_2) within $\sim 10^9/n_H$ yr (where n_H is the hydrogen number density Willacy & Millar (1998)). CO should therefore be completely removed from the gas-phase during the lifetime of a cloud with typical density (10^4 cm^{-3}). However, numerous observations demonstrate its ubiquity (e.g. Buckle et al. (2010)). The gas-phase population is thought to be maintained by a variety of desorption processes. These mechanisms are key to understanding the evolution of molecular clouds.

Where temperatures are low ($\sim$10 K), thermal desorption is negligible and other processes dominate. UV photons, originating either externally from the interstellar radiation field or internally from embedded protostars, cause CO molecules to photodesorb from the surface of the ice, without dissociation. Cosmic rays and X-rays add to the UV field through their interactions with H_2. Other desorption mechanisms involve impulsive heating of the dust grains. These include cosmic ray or X-ray impacts (Leger et al., 1985), cosmic ray photodesorption (where cosmic rays create UV photons) and the formation of H_2 on the dust grain (an exothermic reaction). Photodesorption of CO ice is discussed further in Section 5.4.

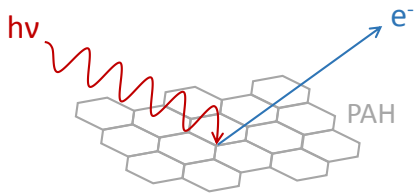

FIGURE 1.12. The ejection of a photoelectron from a PAH molecule (figure adapted from Hollenbach & Tielens (1999).

1.4.2 PHOTOELECTRIC HEATING

Photoelectric heating is thought to occur where far-UV (FUV) photons (6 eV $<$ hν $<$ 13.6 eV) from a nearby star electronically excite PAH molecules. Most of this energy is then re-emitted in the infrared, through vibrational relaxation of the PAHs, although around 0.1 – 1 per cent of the energy is converted to energetic ($\sim$1 eV) photoelectrons, which are ejected from the molecule and heat the gas, PAH + hν $\rightarrow$ PAH$^+$ + e, (Hollenbach & Tielens, 1999; Tielens, 2008). Fig. 1.12 illustrates the ejection of a photoelectron from a PAH molecule. The contribution to gas heating depends on the size of the grain. PAHs and PAH clusters ($<$ 10^3 atoms) are responsible for around half the heating and the other half is due to very small grains (15 – 100 Å). In larger grains, the FUV absorption depth ($\sim$100 Å) can mean that the electron loses all of its kinetic energy as it diffuses towards the surface, resulting in a low yield. Bakes & Tielens (1994) showed that only grains smaller than 100 Å make a significant contribution to the photoelectric heating rate. Grain charge also affects the photoelectric heating efficiency due to the Coulomb attraction. The efficiency is related to the charging parameter, $\gamma = G_0 T^{1/2}/n_e$, which is proportional to the ionization rate divided by the recombination rate.

As PAHs are the most efficient species for ejecting photoelectrons, it is widely accepted that gas temperature and PAH emission are linked in photodissociation regions of molecular clouds (D'Hendecourt & Leger (1987), Lepp & Dalgarno (1988), Verstraete et al. (1990), Bakes & Tielens (1994), Weingartner & Draine (2001)). The first observational evidence for photoelectric heating is proposed in Chapter 4.

1.5 GAS-SOLID MAPPING PROJECT

While much is known about the processes involved in star and planet formation, many of the details are yet to be explored. To develop a full picture of the early stages, it is necessary to understand the physical properties of molecular clouds and the interaction between their gas and solid constituents.

Over the past two decades, observations of pre-stellar molecular clouds have shown them to be cold (T $<$ 10 K) and quiescent. Their chemistry is dominated by the freeze-out of molecular species onto dust grains, depleting their gas-phase abundances. Fig. 1.13 is a schematic of a pre-stellar molecular cloud, based on theory and observations of L1544 (Caselli, 2011). It depicts five zones, each with a distinctive chemistry. At the centre of the cloud, with the highest density, is the 'complete depletion' zone. A little further out is the 'deuteration zone', where deuterated molecules such as N_2D^+ peak in abundance. Next is the 'CO freeze-out' zone, where most of the CO molecules are in the solid-phase on dust grains. Further out still lies the 'dark cloud chemistry' zone. In this region, UV photons allow carbon atoms to form carbon-chain molecules like CCH and CCS. The outer region of the cloud is the PDR, where molecules are dissociated by FUV photons. The sizes of these zones and their physical and chemical properties are likely to vary between clouds, depending on their environment.

In dense molecular cores over half the species (excluding H_2) are thought to be condensed onto dust grains. The connection between this icy material and gas-depletion in star forming regions is now widely accepted (Jørgensen et al. (2002), Tafalla et al. (2004)). However, gas and solid abundance maps of the same regions do not exist for even the most abundant molecules (e.g. CO). Such a comparison would test the theory of freeze-out as the cause of gas-phase depletion as well as identifying the ice formation chemistry occurring at the cloud edges.

CO has a relatively high abundance in both gas and solid-phases. On lines of sight towards highly extincted background stars, such as CK2, it is easy to detect deep CO ice bands (Pontoppidan et al. (2003), Knez et al. (2005)). The abundance of CO gas has been found to drop by at least an order of magnitude in the centres of pre-stellar cores where temperatures are below 20 K and densities (n(H_2)) are greater than 10^5 cm^{-3} (Tafalla et al. (2006)). The first CO ice 'map' confirmed this, showing that CO ice forms in Oph-F at densities of n(H_2) $\sim$1.5 $\times$ 10^5 cm^{-3} in a sharp transition region, after the onset of the H_2O ice (Pontoppidan (2006), Fig. 1.14). This plot provides

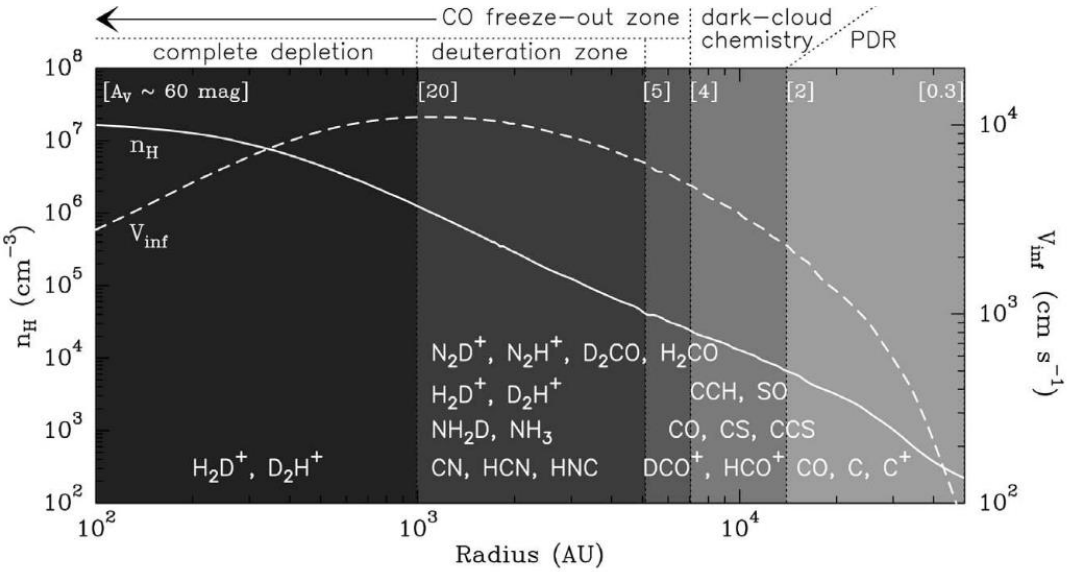

FIGURE 1.13. The physical and chemical structure of a pre-stellar molecular cloud, based on observations and modelling of L1544. Each of five zones, defined by their density and distance from the centre of the cloud, contain particular chemical species. Image reproduced from Caselli (2011), Fig. 1.

valuable one-dimensional information on ice abundances with respect to distance from the centre of the core along five lines of sight. However, more extensive maps using many more background stars are required to fully map the ice distributions.

This thesis is part of a wider investigation into the interaction between the solid and gas-phase molecules present in molecular clouds, known as the 'gas-solid mapping project'. Combining gas and solid-phase CO maps will provide valuable information on the relative spatial distributions of the gas and solid-phase molecules. The CO gas observations also constrain the physical conditions across the cloud. When investigating the connection between gas and solid-phase abundances, it is important to understand the variation in physical conditions and processing histories throughout the cloud. Certain regions may be influenced by shocks and radiation, either from protostars within the cloud or by massive stars nearby. This thesis presents CO gas abundance maps and also constrains the physical properties of the clouds for the gas-solid mapping project. Defining the composition of molecular clouds provides important insights into the formation of protoplanetary disks and the constituents from which planets and life may arise

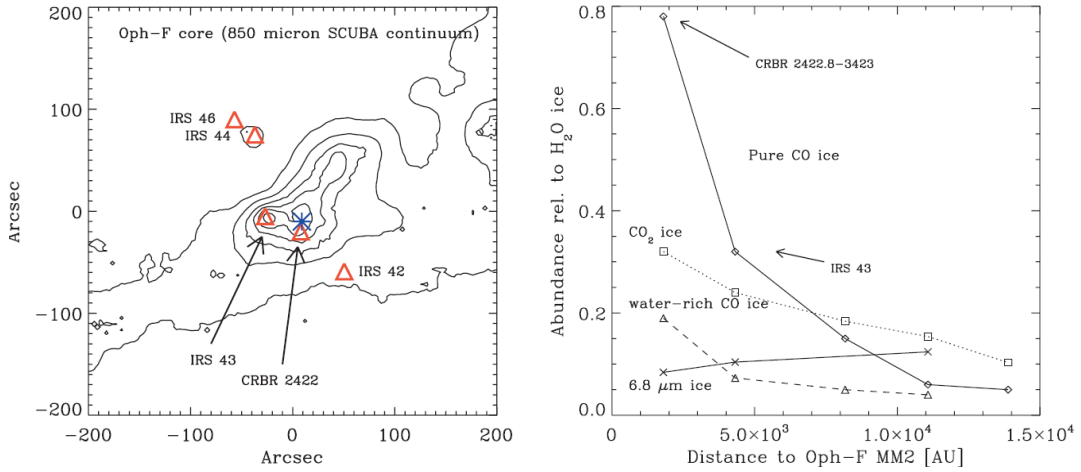

FIGURE 1.14. Left: JCMT-SCUBA 850 μm map from the COMPLETE survey of star forming regions. The red triangles indicate the locations of the infrared sources in the core used to construct the ice map. The (*) symbol shows the centre of the core. Right: Ice abundances relative to water ice in the Oph-F core as a function of projected distance to the core centre as observed with VLT-ISAAC, ISOCAM-CVF and *Spitzer* IRS. Image reproduced from Pontoppidan (2006), Fig. 2 & 3.

1.6 RECENT ADVANCES

The majority of the work laid out in this thesis was completed between 2006 and 2010. Since then, the field has advanced with many new observations and significant results, most notably from the Atacama Large Millimeter/submillimeter Array (ALMA) which began observations in 2011 and became fully operational in 2013.

ALMA is a state-of-the-art interferometer located at an altitude of 5000 m on the Chajnantor plateau in Northern Chile. It operates at millimetre and submillimetre wavelengths, imaging gas-phase molecules with high angular and spectral resolution. In its most compact configuration, the resolution of ALMA is 3.5 arcsec at 115 GHz. Increasing the baseline to 1 km gives 0.5 arcsec resolution and using the most extended 16 km baseline increases it to 0.03 arcsec. In its first few years of operation, ALMA has provided a wealth of new information on the morphology and kinematics of various gas-phase species across molecular clouds and protoplanetary disks.

1.6.1 MOLECULAR CLOUDS

Friesen et al. (2014) report ALMA observations of H_2D^+ 1_{10}-1_{11} emission and the

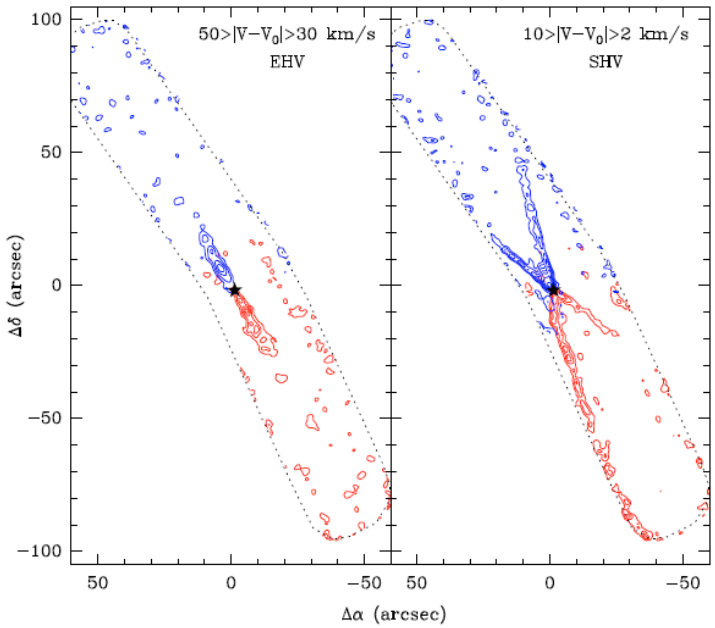

FIGURE 1.15. Interferometric observations of CO ($J = 2 \rightarrow 1$) emission towards IRAS 04166+2706, reproduced from Santiago-García et al. (2009), Fig. 3. Left: Extremely High Velocity (EHV) emission showing a collimated jet structure. Right: Standard High Velocity (SHV) emission outlining shells which surround the EHV jet. The first contour and interval are 6 K km s $^{-1}$ for the EHV map and 5 K km s $^{-1}$ for the SHV map. The beamsize is approximately 2.5 $\times$ 2.0 arcsec.

submillimetre dust continuum towards two molecular cores (SM1 and SM1N) within the Ophiuchus cloud. Both cores contain condensations with masses M $\lesssim$ 0.02 $M_{\odot}$; no substructure is found and a Jeans analysis indicates that both will form single stars. This work is the first interferometric detection of H_2D^+ towards a star forming region. The H_2D^+ emission is offset from the peak of the dust continuum in core SM1N by $\sim$150 – 200 AU. Two possibilities are proposed for the offset: heating by a young undetected protostar, or HD (and consequently H_2D^+) depletion in the cold centre of the core. Identifying these cores as protostellar suggests that in high extinction environments, such as Ophiuchus, infrared surveys may produce incomplete catalogues. This has clear implications for the gas-solid mapping project, where the clouds are identified as 'starless' or 'star forming' based on infrared surveys.

1.6.2 MOLECULAR OUTFLOWS

The large scale CO observations made by Ward-Thompson et al. (2007) for the Gould Belt Survey contain a wealth of information on the gas kinematics. Drabek-Maunder

et al. (2016) performed a meta-analysis of the outflows and energetics of several star forming regions in the Gould Belt clouds. A correlation between the outflow and turbulent kinetic energies would suggest that outflows drive an increase in turbulence. They found no evidence for this but determined that outflows may make a significant contribution to maintaining turbulence against dissipation.

Over the years a range of models have been proposed to explain the observed properties of molecular outflows. Historically they were separated into two classes: wind-blown (e.g. Shu et al. (1991), Li & Shu (1996) and Lee et al. (2001)) and jet-driven (e.g. Canto & Raga (1991), Masson & Chernin (1993) and Chernin & Masson (1995)). These early models successfully described some of the observations: shell outflows were modelled by wide-angle winds while collimated outflows were explained by jet models. However, none of the models could explain the full range of observed outflow morphologies and kinematics. As shells and collimated outflows are now known to coexist (e.g. Santiago-García et al. (2009), Fig. 1.15), more sophisticated models are required. Shang et al. (2006) developed a model which unified the jet- and wind-driven outflows. Li et al. (2013) present a 'wind-driven turbulent entrainment' model which includes turbulent motions in the ambient gas and turbulent mixing with the protostellar wind.

1.6.3 PROTOPLANETARY DISKS

The most recent results from ALMA map the protoplanetary disk of FU Ori object V883 Ori (Cieza et al., 2016). FU Ori objects are T Tauri stars (low mass YSOs) which display an abrupt increase in temperature and luminosity caused by a large transfer of mass from their accretion disk (Hartmann & Kenyon, 1996). The disk radii at which the temperatures are low enough for abundant volatiles to condense are known as snow-lines. In most protoplanetary disks the water snow-line, where the temperature is > 100 K, is too close to the star to be resolved (< 5 AU for solar-type stars). However, the FU Ori outburst caused sublimation of water-ice out to 40 AU, allowing a high angular resolution beam (0.03 arcsec, 12 AU) to detect the water snow-line for the first time. Particle growth is enhanced by various processes beyond the snow-line, improving planet formation efficiencies (Ros & Johansen, 2013). Determining the locations of snow-lines in protoplanetary disks is therefore key to understanding the formation process and composition of planets.

Experimental investigations into the effect of water-ice composition on the growth of planetesimals have recently begun. It is thought that collisional properties may be influenced by the ice species present on the surface of dust grains. Hill et al. (2015) looked at collisions involving ice spheres of pure crystalline water ice, water ice with 5 per cent methanol and water ice with 5 per cent formic acid. The experiments were carried out in an instrument designed to simulate the conditions in protoplanetary disks: temperatures between 131 and 160 K, a pressure of around 10^{-5} mbar and impact velocities between 0.01 and 0.19 m s^{-1}. The instrument was flown on parabolic flights to simulate microgravity. No sticking occurred and no correlation was found between ice composition and coefficient of restitution. The ices contaminated at the 5 per cent level are likely dominated by crystalline water ice, meaning the collisional properties are unaffected. It is inferred that the inclusion of other species at 5 per cent will produce similar results.

The CO snow-line has also been investigated recently with ALMA. Gas-phase CO reduces the rate of N_2H^+ formation and increases the rate of N_2H^+ destruction, so a correlation is predicted between the presence of N_2H^+ and CO depletion. This relationship was first observed in molecular cloud Barnard 68 by Bergin et al. (2002). It was therefore expected that N_2H^+ would be found beyond the CO snow-line in protoplanetary disks. The spatial resolution available with ALMA has allowed detailed imaging of the N_2H^+ emission. Qi et al. (2013) used ALMA to observe the dust continuum and N_2H^+ ($J = 4 \rightarrow 3$) emission with 0.6 arcsec resolution in the disk around TW Hya, a T-Tauri star similar to the solar nebula and oriented almost face-on. Complementary observations of CO ($J = 3 \rightarrow 2$) emission were made with the Submillimeter Array in Hawai'i. Fig. 1.16 shows a ring of N_2H^+ emission with a hole towards the centre of the disk where CO is abundant. The inner edge of the ring traces the onset of CO freeze-out, the CO snow-line.

Other recent results from ALMA (with 0.6×0.5 arcsec resolution) show a ring of complex molecules (methyl formate ($HCOOCH_3$), carbonyl sulphide (OCS) and methanol (CH_3OH)) around protostar IRAS 16293-2422A (Oya et al., 2016). OCS was mapped across the 200 AU envelope while the methyl formate was mainly found in the boundary between the envelope and disk, 50 AU from the protostar. The the methyl formate velocity was used to identify rotation of the ring structure. These high resolution maps provide the first direct evidence for the transport of saturated organic molecules from a molecular cloud into a rotating protoplanetary disk. Previous ALMA observations of protostar L1527 showed a similar physical structure but a different chemical com-

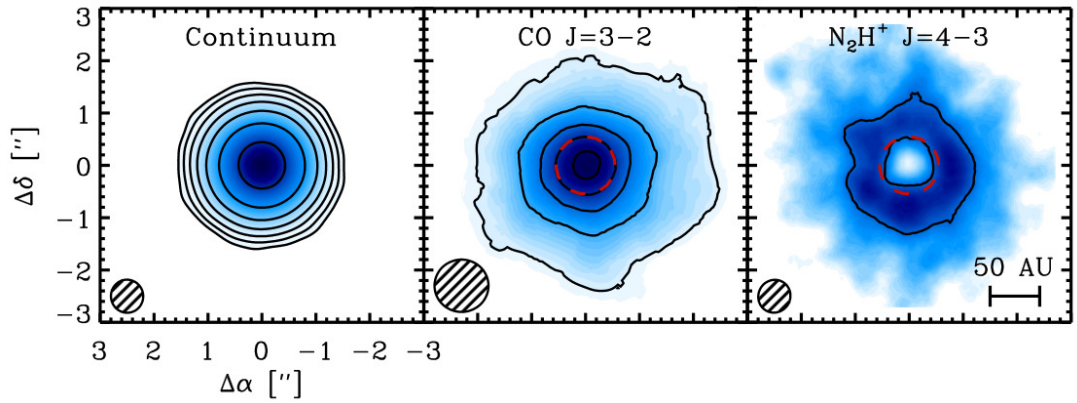

FIGURE 1.16. Observations of dust, CO and N_2H^+ emission towards TW Hya. Left: ALMA 372 GHz continuum. Centre: CO $J = 3 \rightarrow 2$ emission mapped with the Submillimeter Array. Right: ALMA map of N_2H^+ $J = 4 \rightarrow 3$. Beamsizes are shown in the bottom left of each panel. The inner edge of the N_2H^+ ring traces the CO snow-line. Image reproduced from Qi et al. (2013), Fig. 1.

position (Sakai et al., 2014). This demonstrates the variation in materials delivered to planetary systems during their formation and highlights the importance of understanding the chemical and physical properties of molecular clouds where they originate.

The chemical history of the ice species on planetesimals is still debated. They may be inherited from the parent molecular cloud, form in the protostellar envelope, or arise from processing within the protoplanetary disk. Previous detections of simple volatile molecules (e.g. H_2O, HCN) in protoplanetary disks suggest that they survive disk formation or are re-formed in situ (e.g. Cleeves et al. (2014)). Until recently it was not known whether the same is true for complex organic molecules, which are defined as consisting of six or more atoms (Herbst & van Dishoeck, 2009). Öberg et al. (2015) report ALMA observations of the disk around young star MWC 480 which show the first detection of a complex molecule, CH_3CN. Abundance ratios for nitrogen-bearing molecules CH_3CN/HCN are between $\approx$ 5 and 20 per cent. This is similar to the ratio detected towards cometary comae by Mumma & Charnley (2011) ($\approx$ 10 per cent) and suggests that organic-rich comets are not unique to our Solar System.

Further insights into the composition of the primordial solar nebula have been made by the recent *Rosetta* mission, which visited comet 67P/Churyumov-Gerasimenko. Its *Philae* lander discovered a range of complex organic molecules beneath the surface, including CH_3CN, NH_2CHO, CH_3COCH_3 and CH_3OCN (Goesmann et al., 2015). The COmetary SAmpling and Composition (COSAC) experiment measured the CH_3CN/HCN ratio as 30 per cent, in line with the ALMA observations of MWC 480.

The most recent results from the *Rosetta* mission show the presence of amino acid, glycine, in the coma of comet 67P (Altwegg et al., 2016). This is a significant discovery as one theory for the emergence of life on Earth, panspermia, involves the delivery of micro organisms or pre-biotic molecules such as glycine on comets (Wesson, 2010).

1.7 THIS THESIS

The aim of this thesis is to define the morphology and kinematics of a sample of pre-stellar and star forming molecular clouds through observations of CO gas. This work is an integral part of the gas-solid mapping project, exploring the interaction between gas and solid-phase CO in a sample of molecular clouds. Three key questions are addressed:

- *How is CO gas distributed?*
- *What are the temperature and density structures?*
- *How are the morphology and kinematics of CO gas influenced by embedded and nearby stars?*

Nine clouds were mapped over 14.6 $\times$ 14.6 arcmin on scales of 10 – 20 arcsec, or a few 10^3 AU. They range in complexity from isolated and quiescent to extended with active star formation. The CO gas observations were analysed to produce density, temperature and velocity maps of the clouds. This thesis focuses on one cloud, B35A, which has been heavily processed by both internal and external sources.

Chapters 2 and 3 detail the observations and analysis methods. Chapter 2 introduces the procedures for planning and conducting CO observations at the James Clerk Maxwell Telescope (JCMT), the Institut de Radio Astronomie Millimétrique (IRAM) 30 m Telescope and the Nobeyama 45 m Telescope. Chapter 3 describes the analysis methods used and the software written to map the column densities of CO and H_2 gas, the temperature and kinematic structures of the clouds.

Chapters 4 and 5 focus on molecular cloud B35A, a site of active star formation. Chapter 4 describes a correlation between the gas temperature and PAH emission consistent with photoelectric heating. Chapter 5 details the gas morphology and kinematics and explores the theory that photodesorption ahead of a precessing outflow has resulted in an arc of clumps of enhanced CO emission.

Chapter 6 summarises the work undertaken in the course of this PhD. It also shows CO velocity channel maps for starless cloud L158 and presents the first combined maps of CO gas and ice in B35A. The chapter concludes by proposing addional work which would complement and expand on that presented in this thesis.

REFERENCES

Allamandola L. J., Tielens A. G. G. M., Barker J. R., 1989, ApJS, 71, 733 16

Altwegg K., Balsiger H., Bar-Nun A., Berthelier J.-J., Bieler A., Bochsler P., et al. 2016, Science Advances, 2 26

Andre P., Montmerle T., 1994, ApJ, 420, 837 5

Andre P., Ward-Thompson D., Barsony M., 1993, ApJ, 406, 122 5

Arce H. G., Sargent A. I., 2006, ApJ, 646, 1070 9

Arce H. G., Shepherd D., Gueth F., Lee C., Bachiller R., Rosen A., Beuther H., 2007, in B. Reipurth, D. Jewitt, & K. Keil ed., Protostars and Planets V Molecular Outflows in Low- and High-Mass Star-forming Regions. pp 245–260 10

Bachiller R., Guilloteau S., Dutrey A., Planesas P., Martin-Pintado J., 1995, A&A, 299, 857 9

Bakes E. L. O., Tielens A. G. G. M., 1994, ApJ, 427, 822 18

Bally J., Reipurth B., Davis C. J., 2007, Protostars and Planets V, pp 215–230 10

Barnard E. E., 1910, ApJ, 31, 8 2

Barnard E. E., 1927, Catalogue of 349 dark objects in the sky. University of Chicago Press, 1927 2

Bergin E. A., Alves J., Huard T., Lada C. J., 2002, ApJL, 570, L101 24

Bergin E. A., Melnick G. J., Gerakines P. A., Neufeld D. A., Whittet D. C. B., 2005, ApJL, 627, L33 15

Bok B. J., Reilly E. F., 1947, ApJ, 105, 255 3

Boogert A. C. A., Ehrenfreund P., 2004, in Witt A. N., Clayton G. C., Draine B. T., eds, Astrophysics of Dust Vol. 309 of Astronomical Society of the Pacific Conference Series, Interstellar Ices. p. 547 17

Boogert A. C. A., Pontoppidan K. M., Knez C., Lahuis F., Kessler-Silacci J., van Dishoeck E. F., Blake G. A., Augereau J.-C., Bisschop S. E., et al., 2008, ApJ, 678, 985 4

Buckle J. V., Curtis E. I., Roberts J. F., White G. J., Hatchell J., Brunt C., Butner H. M., Cavanagh B., Chrysostomou A., Davis C. J., Duarte-Cabral A., Etxaluze M., di Francesco J., et al., 2010, MNRAS, 401, 204 17

Canto J., Raga A. C., 1991, ApJ, 372, 646 23

Caselli P., 2011, in Cernicharo J., Bachiller R., eds, The Molecular Universe Vol. 280 of IAU Symposium, Observational Studies of Pre-Stellar Cores and Infrared Dark Clouds. pp 19–32 19, 20

Chernin L. M., Masson C. R., 1995, ApJ, 455, 182 23

Cieza L. A., Casassus S., Tobin J., Bos S. P., Williams J. P., Perez S., Zhu Z., Caceres C., Canovas H., Dunham M. M., Hales A., Prieto J. L., Principe D. A., Schreiber M. R., Ruiz-Rodriguez D., Zurlo A., 2016, ArXiv e-prints 23

Clarke D. A., 2012, Nature, 492, 52 5

Cleeves L. I., Bergin E. A., Alexander C. M. O. ., Du F., Graninger D., Öberg K. I., Harries T. J., 2014, Science, 345, 1590 25

Dame T. M., Hartmann D., Thaddeus P., 2001, ApJ, 547, 792 14

De Vries C. H., Narayanan G., Snell R. L., 2002, ApJ, 577, 798 12, 13

D'Hendecourt L. B., Leger A., 1987, A&A, 180, L9 18

Di Francesco J., Hogerheijde M. R., Welch W. J., Bergin E. A., 2002, AJ, 124, 2749 15

Drabek-Maunder E., Hatchell J., Buckle J. V., Di Francesco J., Richer J., 2016, MNRAS, 457, L84 22

Evans II N. J., Allen L. E., Blake G. A., Boogert A. C. A., Bourke T., Harvey P. M., Kessler J. E., Koerner D. W., et al., 2003, PASP, 115, 965 15

Fraser H. J., Collings M. P., Dever J. W., McCoustra M. R. S., 2004, MNRAS, 353, 59 15

Friesen R. K., Di Francesco J., Bourke T. L., Caselli P., Jørgensen J. K., Pineda J. E., Wong M., 2014, ApJ, 797, 27 21

Gerakines P. A., Whittet D. C. B., Ehrenfreund P., Boogert A. C. A., Tielens A. G. G. M., Schutte W. A., Chiar J. E., van Dishoeck E. F., Prusti T., Helmich F. P., de Graauw T., 1999, ApJ, 522, 357 4

Gibb E. L., Whittet D. C. B., Boogert A. C. A., Tielens A. G. G. M., 2004, ApJS, 151, 35 4

Gillett F. C., Forrest W. J., 1973, ApJ, 179, 483 3

Girart J. M., Rodriiguez L. F., Anglada G., Estalella R., Torrelles J. M., Marti J., Pena M., Ayala S., Curiel S., Noriega-Crespo A., 1994, ApJL, 435, L145 10

Goesmann F., Rosenbauer H., Bredehöft J. H., Cabane M., Ehrenfreund P., Gautier T., Giri C., Krüger H., Le Roy L., MacDermott A. J., et al., 2015, Science, 349 25

Goodman A. A., 2004, in Johnstone D., Adams F. C., Lin D. N. C., Neufeeld D. A., Ostriker E. C., eds, Star Formation in the Interstellar Medium: In Honor of David Hollenbach Vol. 323 of Astronomical Society of the Pacific Conference Series, The COMPLETE Survey of Star-Forming Regions on its Second Birthday. p. 171 15

Grabelsky D. A., Cohen R. S., Bronfman L., Thaddeus P., 1988, ApJ, 331, 181 3

Greve T. R., Bertoldi F., Smail I., Neri R., Chapman S. C., Blain A. W., Ivison R. J., Genzel R., Omont A., Cox P., Tacconi L., Kneib J.-P., 2005, MNRAS, 359, 1165 14

Hartmann L., Kenyon S. J., 1996, ARAA, 34, 207 23

Herbst E., van Dishoeck E. F., 2009, ARAA, 47, 427 25

Herschel, W. 1785, Phil. Trans. R. Soc. Lond., 75, 213 2, 9

Hill C. R., Heißelmann D., Blum J., Fraser H. J., 2015, A&A, 575, A6 24

Hirota T., Bushimata T., Choi Y. K., Honma M., Imai H., Iwadate K., Jike T., Kameno S., Kameya O., Kamohara R., Kan-Ya Y., Kawaguchi N., Kijima M., Kim M. K., Kobayashi H., et al., 2007, PASJ, 59, 897 5

Hogerheijde M. R., Caselli P., Emprechtinger M., van der Tak F. F. S., Alves J., Belloche A., Güsten R., Lundgren A. A., Nyman L.-Å., Volgenau N., Wiedner M. C., 2006, A&A, 454,

L59 15
Hollenbach D. J., Tielens A. G. G. M., 1999, Reviews of Modern Physics, 71, 173 12, 18
Huggins P. J., Bachiller R., Planesas P., Forveille T., Cox P., 2005, ApJS, 160, 272 15
Isella A., 2006, PhD Thesis, The University of Milan 8
Jørgensen J. K., Schöier F. L., van Dishoeck E. F., 2002, A&A, 389, 908 19
Knez C., Boogert A. C. A., Pontoppidan K. M., Kessler-Silacci J., van Dishoeck E. F., Evans II N. J., Augereau J.-C., Blake G. A., Lahuis F., 2005, ApJL, 635, L145 4, 19
Lada C. J., 1987, in Peimbert M., Jugaku J., eds, Star Forming Regions Vol. 115 of IAU Symposium, Star formation - From OB associations to protostars. pp 1–17 5
Lada C. J., Wilking B. A., 1984, ApJ, 287, 610 5
Launhardt R., Nutter D., Ward-Thompson D., Bourke T. L., Henning T., Khanzadyan T., Schmalzl M., Wolf S., Zylka R., 2010, ApJS, 188, 139 3
Lee C.-F., Stone J. M., Ostriker E. C., Mundy L. G., 2001, ApJ, 557, 429 23
Leger A., Jura M., Omont A., 1985, A&A, 144, 147 17
Lepp S., Dalgarno A., 1988, ApJ, 335, 769 18
Li G.-X., Qiu K., Wyrowski F., Menten K., 2013, A&A, 559, A23 23
Li Z.-Y., Shu F. H., 1996, ApJ, 472, 211 23
Mann R. K., Di Francesco J., Johnstone D., Andrews S. M., Williams J. P., Bally J., Ricci L., Hughes A. M., Matthews B. C., 2014, ApJ, 784, 82 5
Masson C. R., Chernin L. M., 1993, ApJ, 414, 230 23
Matzner C. D., McKee C. F., 2000, in American Astronomical Society Meeting Abstracts 195 Vol. 32 of Bulletin of the American Astronomical Society, The nature of bipolar outflows and the fates of stellar cluster-forming regions. p. 135.07 10
Mumma M. J., Charnley S. B., 2011, ARAA, 49, 471 25
Murray N., 2011, ApJ, 729, 133 3
Najita J., Carr J. S., Mathieu R. D., 2003, ApJ, 589, 931 14
Narayanan D., Li Y., Cox T. J., Hernquist L., Hopkins P., Chakrabarti S., Davé R., Di Matteo T., Gao L., Kulesa C., Robertson B., Walker C. K., 2008, ApJS, 174, 13 15
Narayanan G., Snell R., Bemis A., 2012, MNRAS, 425, 2641 9
Noble J. A., Fraser H. J., Aikawa Y., Pontoppidan K. M., Sakon I., 2013, ApJ, 775, 85 4
Nummelin A., Whittet D. C. B., Gibb E. L., Gerakines P. A., Chiar J. E., 2001, ApJ, 558, 185 4
Öberg K. I., Boogert A. C. A., Pontoppidan K. M., Blake G. A., Evans N. J., Lahuis F., van Dishoeck E. F., 2008, ApJ, 678, 1032 4
Öberg K. I., Guzmán V. V., Furuya K., Qi C., Aikawa Y., Andrews S. M., Loomis R., Wilner D. J., 2015, Nature, 520, 198 25
Ogura K., Sugitani K., 1998, PASA, 15, 91 13
Oka T., Nagai M., Kamegai K., Tanaka K., Kuboi N., 2007, PASJ, 59, 15 15

Oya Y., Sakai N., López-Sepulcre A., Watanabe Y., Ceccarelli C., Lefloch B., Favre C., Yamamoto S., 2016, ApJ, 824, 88 24

Pontoppidan K. M., 2006, A&A, 453, L47 19, 21

Pontoppidan K. M., Fraser H. J., Dartois E., Thi W.-F., van Dishoeck E. F., Boogert A. C. A., d'Hendecourt L., Tielens A. G. G. M., Bisschop S. E., 2003, A&A, 408, 981 4, 19

Ptolemy C., 144, Almagest (trans Peters, C. H. F. and Knobel, E. B.) Carnegie Institution of Washington 5

Qi C., Öberg K. I., Wilner D. J., D'Alessio P., Bergin E., Andrews S. M., Blake G. A., Hogerheijde M. R., van Dishoeck E. F., 2013, Science, 341, 630 24, 25

Raga A. C., Williams D. A., 2000, A&A, 358, 701 11

Reipurth B., 2000, VizieR Online Data Catalog, 5104, 0 10

Richer J. S., Hills R. E., Padman R., 1992, MNRAS, 254, 525 9

Roberts H., Millar T. J., 2007, A&A, 471, 849 3

Ros K., Johansen A., 2013, A&A, 552, A137 23

Rudolph A., Welch W. J., 1988, ApJL, 326, L31 10

Safron E. J., Fischer W. J., Megeath S. T., Furlan E., Stutz A. M., Stanke T., Billot N., Rebull L. M., Tobin J. J., Ali B., Allen L. E., Booker J., Watson D. M., Wilson T. L., 2015, ApJL, 800, L5 5

Sakai N., Oya Y., Sakai T., Watanabe Y., Hirota T., Ceccarelli C., Kahane C., Lopez-Sepulcre A., Lefloch B., Vastel C., Bottinelli S., Caux E., Coutens A., Aikawa Y., Takakuwa S., Ohashi N., Yen H.-W., Yamamoto S., 2014, ApJL, 791, L38 25

Salak D., Nakai N., Kitamoto S., 2014, PASJ, 66, 96 15

Santiago-García J., Tafalla M., Johnstone D., Bachiller R., 2009, A&A, 495, 169 22, 23

Shang H., Allen A., Li Z.-Y., Liu C.-F., Chou M.-Y., Anderson J., 2006, ApJ, 649, 845 23

Shu F. H., Adams F. C., Lizano S., 1987, ARAA, 25, 23 5

Shu F. H., Najita J. R., Shang H., Li Z.-Y., 2000, Protostars and Planets IV, pp 789–814 10

Shu F. H., Ruden S. P., Lada C. J., Lizano S., 1991, ApJL, 370, L31 23

Slipher V. M., 1912, Lowell Observatory Bulletin, 2, 26 4

Snell R. L., Loren R. B., Plambeck R. L., 1980, ApJL, 239, L17 9

Sugitani K., Fukui Y., Ogura K., 1991, ApJS, 77, 59 13

Tafalla M., Myers P. C., Caselli P., Walmsley C. M., 2004, A&A, 416, 191 19

Tafalla M., Santiago-García J., Myers P. C., Caselli P., Walmsley C. M., Crapsi A., 2006, A&A, 455, 577 19

Taylor S. D., Morata O., Williams D. A., 1996, A&A, 313, 269 3

Tielens A. G. G. M., 1999, in Greenberg J. M., Li A., eds, NATO Advanced Science Institutes (ASI) Series C Vol. 523 of NATO Advanced Science Institutes (ASI) Series C, The destruction of interstellar dust. p. 331 10

Tielens A. G. G. M., 2005, The Physics and Chemistry of the Interstellar Medium. Cambridge

University Press 16
Tielens A. G. G. M., 2008, ARAA, 46, 289 16, 18
Torrelles J. M., Rodriguez L. F., Canto J., Anglada G., Gomez J. F., Curiel S., Ho P. T. P., 1992, ApJL, 396, L95 10
van der Tak F. F. S., Caselli P., Ceccarelli C., 2005, A&A, 439, 195 15
Velusamy T., Langer W. D., 1998, Nature, 392, 685 10
Verstraete L., Leger A., D'Hendecourt L., Defourneau D., Dutuit O., 1990, A&A, 237, 436 18
Ward-Thompson D., Di Francesco J., Hatchell J., Hogerheijde M. R., Nutter D., Bastien P., Basu S., Bonnell I., Bowey J., Brunt C., Buckle J., Butner H., Cavanagh B., et al., 2007, PASP, 119, 855 15, 22
Weingartner J. C., Draine B. T., 2001, ApJS, 134, 263 18
Wesson P. S., 2010, Space Sci. Rev., 156, 239 26
Willacy K., Millar T. J., 1998, MNRAS, 298, 562 17
Wu Y., Wei Y., Zhao M., Shi Y., Yu W., Qin S., Huang M., 2004, A&A, 426, 503 9

CHAPTER 2

OBSERVATIONS OF CO GAS IN MOLECULAR CLOUDS

SYNOPSIS

This chapter describes the work carried out to map the distribution of CO gas across several starless and star forming molecular clouds. It begins by introducing the clouds selected for the gas-solid mapping project. The procedure for applying for time on world-class telescopes is then outlined and considerations such as the cloud elevation and atmospheric conditions are described.

Time was awarded on three telescopes; the James Clerk Maxwell Telescope (JCMT), the Institut de Radio Astronomie Millimétrique (IRAM) 30 m Telescope and the Nobeyama 45 m Radio Telescope. Technical details of these telescopes and their heterodyne receiver arrays are laid out. The observing strategies implemented at each telescope are also described in this chapter.

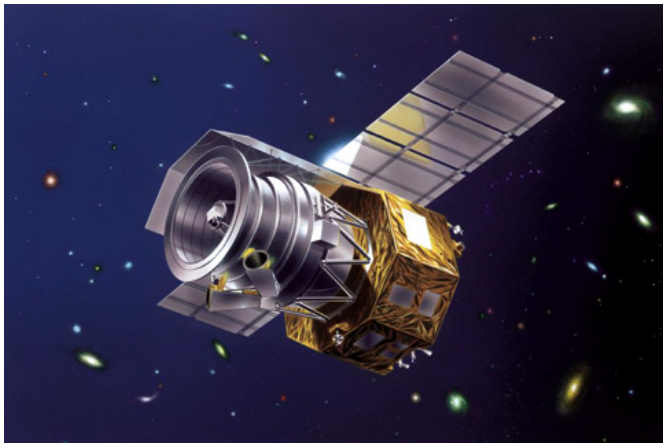

FIGURE 2.1. The *AKARI* satellite, developed by the Japan Aerospace Exploration Agency (JAXA) and used to study ice abundance in molecular clouds (image courtesy of JAXA).

2.1 MOLECULAR CLOUD SELECTION

2.1.1 ICE MAPS

The gas-solid mapping project began with a study of ice abundance across 19 prestellar and star forming clouds. Near-InfraRed (NIR) spectroscopic observations of the three most abundant solid-phase molecular species (H_2O, CO_2 and CO) were made with the Japan Aerospace Exploration Agency (JAXA) *AKARI* satellite (Fig. 2.1). The 2.5 – 5 μm region is associated with the stretching vibration of each of these molecules and shows the strongest absorption for all three. These absorption bands were observed along lines of sight to relatively bright background stars (1 mJy where $A_V > 10$) and embedded YSOs. One of the spectra, with three distinct absorption bands: H_2O at 3.0 μm, CO_2 at 4.25 μm and CO at 4.67 μm, is shown in Fig. 2.2. The InfraRed Camera (IRC) on *AKARI* dispersed the light from all sources in the field of view using a prism (NP) or grism (NG) dispersion element. The grism provided a higher resolution but resulted in more severe 'confusion' in the field, where the spectra from neighbouring sources overlap. As this type of observation had never previously been done, both methods were used to ensure the necessary absorption features could be extracted.

An extensive data reduction pipeline for analysing the *AKARI* 1 × 1 arcmin NG fields of view, *AKARI* REDUCTION FACILITY (ARF), is detailed in Noble (2011) and Noble et al. (2013) where the first ice column density maps are also presented. A further pipeline for the analysis of the *AKARI* 9.5 × 10 arcmin NP fields of view, ARF2, is documented in Suutarinen (2015) along with ice maps of these larger regions.

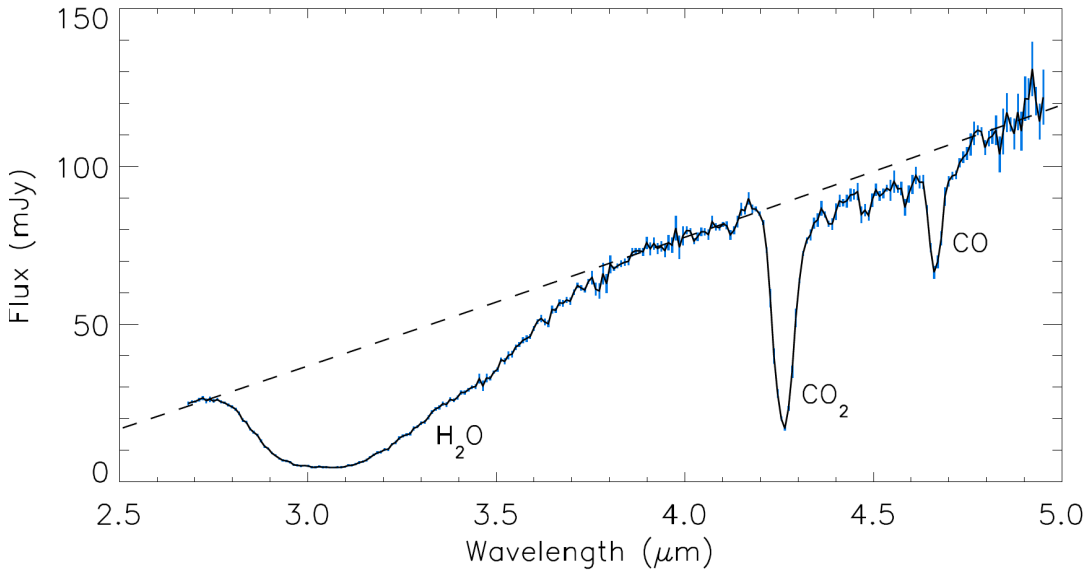

FIGURE 2.2. An *AKARI* spectrum towards an embedded YSO in B35A (Jennifer Noble, private communication). Three ice absorption bands are evident: H_2O at 3.0 μm, CO_2 at 4.25 μm and CO at 4.67 μm. Error bars are shown in blue and the dashed line is a linear fit to the data.

2.1.2 CO GAS MAPS

Twelve of the *AKARI* clouds were selected for CO gas mapping (see Table 2.1). These targets, all visible from three ground based telescopes, are variety of star forming, bright-rimmed and quiescent clouds. The aim of the gas-mapping project was to observe three isotopologues and three transitions of CO (^{12}CO, ^{13}CO and C^{18}O; $J = 3 \rightarrow 2$ and $J = 2 \rightarrow 1$) across 14.6 × 14.6 arcmin regions centred on the coordinates listed in Table 2.1. Observations of the three isotopologues allowed an investigation into a range of environments within the clouds. The ^{12}CO emission showed the optically thick cloud surface. ^{13}CO is less abundant and emission from deeper in the cloud was observed. The least abundant of the three isotopologues, C^{18}O, probed even deeper into the dense regions of the cloud. Maps of multiple CO transitions were made for use with the RADEX radiative transfer code to determine the H_2 volume densities of the clouds. The map dimensions were defined by the *AKARI* field of view in its two spectroscopic observing modes. Assuming an average cloud distance of 200 – 400 pc, the map spatial resolution is ∼3000 – 6000 AU for observations with a beamsize of 15 arcsec.

TABLE 2.1. Target clouds first observed with *AKARI* and visible from the three ground based telescopes used in the course of this PhD

Cloud	RA (J2000)	Dec (J2000)	Distance (pc)	Type
B35A	05 44 37.0	+09 10 13.0	400 ± 40	bright-rimmed & star forming
L158	16 47 03.5	-14 00 12.0	165	starless
L204C-2	16 47 37.8	-12 21 38.4	165	bright-rimmed & starless
L310	18 07 12.0	-18 21 36.0	-	starless
L462-1	18 07 40.1	-04 40 09.7	200	star forming
L438	18 14 06.3	-07 08 00.9	270 ± 50	starless
L492	18 15 51.0	-03 45 19.4	270 ± 50	starless
L429C	18 17 05.4	-08 13 49.5	200	starless
L723	19 17 51.2	+19 12 39.2	-	star forming
CB188	19 20 15.5	+11 35 59.8	300 ± 100	star forming
L694-2	19 41 05.6	+10 56 41.4	-	starless
L1165	22 06 40.4	+59 05 59.7	300	star forming

References: L158 & L204C-2: Chini (1981),
L462-1 & L429(1-4): Dame & Thaddeus (1985), Aquila Rift (200 pc)
L438 & L492: Straižys et al. (2003); CB188: Herbig & Jones (1983), association to L673

2.2 OBSERVING PROPOSALS

The CO gas-mapping project required many hours of observing time on three world-class telescopes: the James Clerk Maxwell Telescope (JCMT), Institut de Radio Astronomie Millimétrique (IRAM) 30 m Telescope and Nobeyama 45 m Radio Telescope. All three are in high demand and 'Time Allocation Committees' (TACs) are responsible for deciding which of the projects, proposed by astronomy groups worldwide, are observed. The author submitted requests for telescope time when TACs issued a 'call for proposals', normally twice a year. The TACs assessed the proposals for scientific and technical merit and allocated telescope time accordingly. The cover pages of a typical proposal submitted by the author are shown in Fig. 2.3. The first page lists the project team members and summarises the aim of the work (a coupled gas-solid map of L438). The second page shows the receiver, spectrometer and frequencies necessary for observation. It also specifies the target position and time requested. Relevant publications by the project team are listed. Two or three written pages are also included in most proposals. They give more background to the project and make a strong scientific case for the observations, putting it in the context of other work and describing the impact of the results on the field; figures are often incorporated in these pages. A technical justification is also included; it describes the mapping strategy, integration (observation) time calculations and suitable grades of weather.

Ver. 4.00

Registration No. 2005. . . Proposal No.

Application Form for 45-m Telescope Time (1/2)

Category 2 1. General Program 2. Short Program 3. others Date: Y 2007 M 2 D 27

Title (Please Type in English) **Comparing Gas and Solid CO Distribution in Molecular Core L438**

Scientific Category: 2 indicate one category into which this proposal falls.
1 Star Formation 2 Astro-chemistry 3 Stellar 4 Galactic System 5 Extragalactic 6 Other

1. Principal Investigator: Name (Family, First Name) Craigon, Alison ***Furigana**

***English Name of P.I.:(Family, Initial)** Craigon, A. ***Present Position** PhD Student ***For Thesis?** yes

2. Institution: Strathclyde University

3. Address: John Anderson Building, 107 Rottenrow, Glasgow, G4 0NG Country: SCOTLAND

Phone: +44 141 548 3059 Fax: +44 141 552 2891 E-mail: alison.craigon@strath.ac.uk

4. Collaborators (Family, First Name)	5. Institution	Country	*6. Present Position*For Th
Fraser, Helen	Strathclyde University	SCOTLAND	
Dent, Bill	Royal Observatory Edinburgh	SCOTLAND	
Thi, Wing-Fai	Royal Observatory Edinburgh	SCOTLAND	
Pontoppidan, Klaus	Caltech	USA	
Aikawa, Yuri	Kobe University	JAPAN	
Kandori, Ryo	National Astronomical Observatory	JAPAN	

7. Contact Person: Name (Family, First Name)

8. Institution:

9. Address:

Phone: Fax: E-mail:

Abstract (Please attach scientific justification within the maximum of 2 pages of A4, including figures and tables.)

We propose to use BEARS to map the distribution of 3 isotopomers of gaseous CO (^{12}CO, ^{13}CO and C^{18}O) in molecular core L438. Background stars will be observed to determine column densities of gas-phase CO across the core. These maps will then be combined with solid-phase CO maps obtained similarly by Akari to produce the first coupled gas-solid map of a starless core.

This proposal is a a) New one, b) Re-submission of previous proposal or c) Continuation of previous observation.

In case of b) or c), please indicate previous proposal No.

Relationship of the previous proposal/observations to the current research

* For Domestic users only

• Sections 1-9 should be typed in ALPHABET by foreign applicants and in KANJI by domestic users.

FIGURE 2.3. An observing proposal for the Nobeyama 45 m Radio Telescope.

Ver. 4.00

Application Form for 45-m Telescope Time (2/2)

Type: S: line C: continuum [S] **Principal Investigator:** Craigon, Alison

Receivers: [ ] H22 [ ] H28/32 [ ] H40 [ ] S40
[ ] S80 [ ] S100 [X] BEARS [ ] NOBA

Frequencies:		
molecule	transition	frequency(GHz)
^{12}CO	1-0	115.271202
^{13}CO	1-0	110.201354
C^{18}O	1-0	109.782173

Spectrometer:
□ AOS High
□ AOS Wide
□ AOS UW
☒ Auto Correlator

List of Objects: total number of objects [1] (Please attach a separate sheet if the list is long.)

Source Name	R.A.(J2000) h m s	Dec.(J2000) ° ′ ″	Velocity (km/s)	Remarks
L438	18 14 06.3	-07 08 00.9	0	

Total hours requested: [20] Hours (including overhead for receiver tuning, pointing calibration, etc.)

Indicate numbers (integer) for each LST range

LST	0	1	2	3	4	5	6	7	8	9	10	11	12	13	14	15	16	17	18	19	20	21	22	23	24
number																	5	5	5	5					

Requests concerning instruments, scheduling, etc.
(e.g. please indicate a season when programme sources are close to the Sun.)

Abstract of Back-Up Program for Poor Observing Conditions (if any)

Receivers for Back-Up Programme
[ ] H22 [ ] H40 [ ] S40

List of your (and collaborators') publications (including submitted papers) related to the present research. (within 5 papers) (Authors, Title, Journal, Vol., First and Last Page, Year)

1. Thi, W.-F. et al., VLT-ISAAC 3-5 micron spectroscopy of embedded young low-mass stars. III. Intermediate mass sources in Vela, A&A, 449,251-265, 2006
2. Pontoppidan, K., Fraser, H.J. et al., The 3-5 micron VLT survey of ices around embedded young low mass stars I, A&A, 408,981-1007, 2003
3. van Dishoeck, E.F., Dartois, E., Pontoppidan, K.M., Thi, W.-F., D'Hendecourt, L., Boogert, A.C.A., Fraser, H.J., et al., Origin and Evolution of Ices in Star-Forming Regions: A VLT ISAAC 3-5 micron Spectroscopic Survey, ESO Messenger, 113,49-55, 2003
4. van Broekhuizen, F., Fraser, H.J., Pontoppidan, K.M., & van Dishoeck, E.F., A 3-5 micron VLT survey of ices around embedded young low mass stars II: OCN, A&A, 441,249-260, 2005
5. Pontoppidan, K.M., van Dishoeck, E.F., Dartois, E., Fraser, H.J., et al., Astrochemistry: Recent Successes and Current Challenges, Proceedings of the 231st Symposium of the International Astronomical Union 2005, Cambridge University Press, pp.319-320, 2005

FIGURE 2.3 CONTINUED. An observing proposal for the Nobeyama 45 m Radio Telescope.

TABLE 2.2. Telescope time awarded to the author for observations of CO gas in molecular clouds

Telescope	Observing Run	Observation Dates	Hours Allocated
JCMT	M07BU025	6th Sep – 9th Sep 2007	45
	M08BU027	27th Sep – 29th Sep 2008	32
IRAM 30 m	088-07	30th Oct – 5th Nov 2007	27 (HERA pool)
	090-08	15th Oct – 21st Oct 2008	50 (HERA pool)
	178-09	15th Dec – 21st Dec 2009	32 (HERA pool)
Nobeyama 45 m	SP68004	27th Apr – 1st May 2007	20
		Total	206

This thesis is based on observations conducted following a series of six successful proposals submitted by the author. Details of the observing time awarded on the JCMT, IRAM 30 m Telescope and Nobeyama 45 m Radio Telescope are listed in Table 2.2.

2.2.1 SOURCE VISIBILITY

Determining which molecular clouds would be visible from each telescope at a certain time of year required calculations based on the telescope latitude (ϕ) and longitude (λ), listed in Table 2.3 (and shown in Fig. 2.4), along with the cloud right ascension (α) and declination (δ). The declination range visible from a telescope depends on its latitude. In the northern hemisphere, where all three telescopes are located, sources with $\delta > 90\text{-}\phi^\circ$ are circumpolar (never set) and those with $\delta < \text{-}(90\text{-}\phi)^\circ$ never rise. The remainder rise and set at different times over the course of a year, depending on their right ascension. Although telescopes at higher latitudes can observe only a small region of the southern sky, they have many circumpolar sources which can be observed for a large part of the year. Telescopes near the equator, however, can observe sources across a much wider range of declinations. Fewer sources are circumpolar at these lower latitudes so there is a much greater seasonal variation in visibility. The optimum observation date for a molecular cloud is when it transits the meridian (reaching its highest point in the sky) around mid-shift, resulting in the longest visibility and shortest path length through the atmosphere. This occurs when the local sidereal time (LST) is equal to the right ascension of the source. The hour angle (h) describes the distance of the source from the meridian, $h = LST - \alpha$. The source altitude above the horizon can then be calculated using: $\sin alt = (\sin \phi \sin \delta) + (\cos \phi \cos \delta \cos h)$.

The local terrain can also affect the visibility of sources at low altitudes. However,

TABLE 2.3. Locations of telescopes used for observations of CO gas in molecular clouds

Telescope	Country	Latitude	Longitude	Altitude (m)
JCMT	Hawai'i	19°49′33″N	155°28′47″W	4092
IRAM 30 m	Spain	37°04′06″N	3°23′56″W	2850
Nobeyama 45 m	Japan	35°56′30″N	138°28′33″E	1350

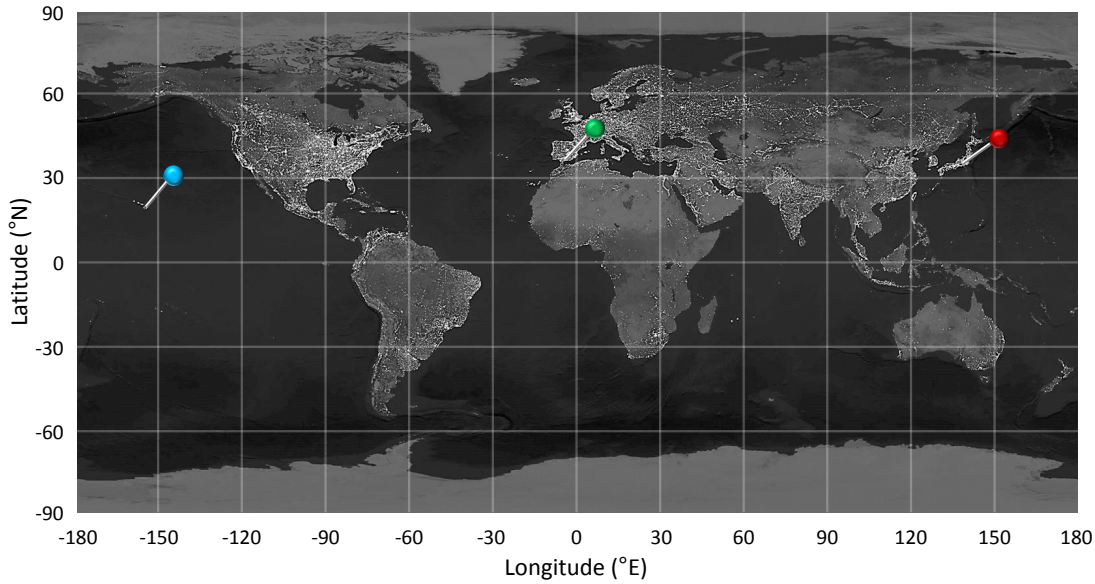

FIGURE 2.4. The locations of three telescopes are indicated by the coloured pins. From left: the JCMT is marked in blue, the IRAM 30 m Telescope in green, and the Nobeyama 45 m Radio Telescope in red. Image credit: Data courtesy Marc Imhoff of NASA GSFC and Christopher Elvidge of NOAA NGDC. Adapted from image by Craig Mayhew and Robert Simmon, NASA GSFC.

most world-class telescopes are sited in locations where the horizon does not interfere with observations. In some cases, the manoeuvring capabilities of the telescope must be taken into account when observing sources with a very high or very low altitude. Ideally, the target molecular clouds will rise to a reasonable altitude above the horizon (i.e. at least 30°) for the duration of the integration time. However, if this is not possible, a map can be built up from several shorter integrations over a few nights.

2.2.2 ATMOSPHERIC TRANSMISSION

Atmospheric water vapour affects observations at submillimetre and millimetre wavelengths. It attenuates the source emission, reducing the signal, and increases the noise

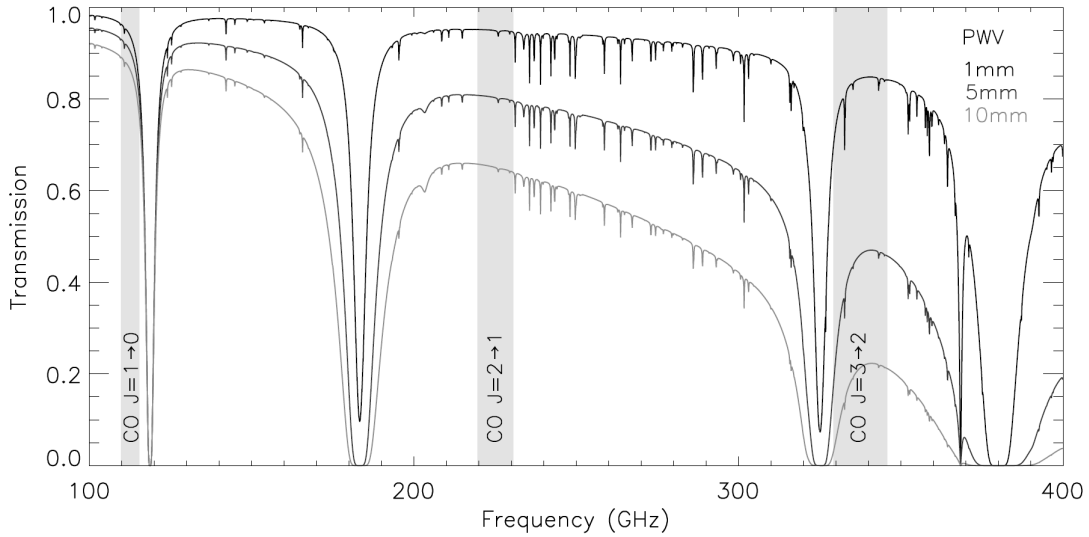

FIGURE 2.5. The atmospheric transmission between 100 and 400 GHz for 1, 5 and 10 mm PWV at the Atacama Large Millimeter Array in Chile. The CO frequency ranges (observed with other telescopes for the the gas-mapping project) are shaded grey.

by thermal radiation. Fig. 2.5 illustrates that the higher CO transitions are more strongly affected by atmospheric water vapour than the lower transitions and therefore require drier observing sites. The transmission data are for the Atacama Large Millimetre Array (ALMA) in Chile. At an altitude of over 5000m, it is one of the highest telescope sites in the world and therefore benefits from a drier atmosphere than all three telescopes used in this work. The plot was produced using the ALMA atmosphere model, which is based on the ATM model (Pardo et al., 2009).

The weather condition at a telescope is often classified in terms of the precipitable water vapour (PWV) in the atmosphere. PWV is defined as the depth of water that would be obtained if a column of atmosphere were condensed into a container of the same cross-sectional area. There can be a large seasonal variation in PWV, for example at the IRAM 30 m Telescope: 7 mm is considered average in summer, while 4 mm is good in summer but only average in winter, 2 mm is excellent in summer but good in winter, and 1 mm is only possible in winter.

Atmospheric opacity is typically measured using a radiometer at 225 GHz (τ_{225}) and scaled to other frequencies (e.g. τ_{345} = 0.05 + 2.5τ_{225}). Atmospheric transmission models (e.g. Liebe (1989)) relate the opacity and PWV at various observing sites, for example: $\tau_{225} \simeq 0.04\text{PWV} + 0.01$ (JCMT) and $\tau_{225} = 0.058\text{PWV} + 0.004$ (IRAM). High opacity and PWV levels require longer integration times to reach the required

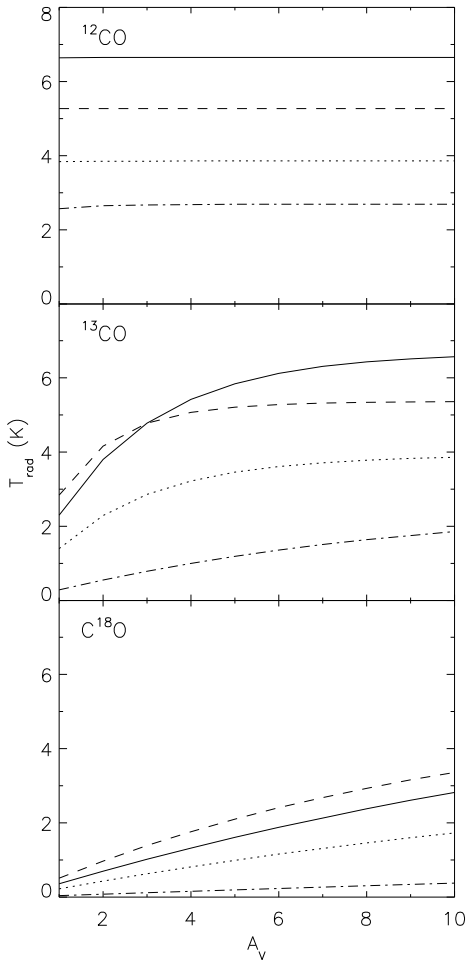

FIGURE 2.6. Radiation temperatures as a function of A_V for ^{12}CO, ^{13}CO and C^{18}O calculated using the RADEX code ($J = 1 \rightarrow 0$ solid, $J = 2 \rightarrow 1$ dash, $J = 3 \rightarrow 2$ dot, $J = 4 \rightarrow 3$ dot-dash).

signal-to-noise ratio.

2.2.3 INTEGRATION TIME

The integration time required for a certain signal-to-noise ratio depends on: the characteristics of the receiver, the source altitude, the mapping strategy and the weather. Since several of these factors are unique to each telescope, an online 'integration time calculator' is often provided. The calculator uses the source altitude, observation frequency and weather grade to estimate the system temperature (T_{sys}). The receiver temperature (T_{rx}) is then used to determine the time required to reach the requested noise level.

FIGURE 2.7. A view from the JCMT of some of the other telescopes on Mauna Kea.

The target molecular clouds have a range of extinctions (A_V) from ∼5 near the edge to ∼30 at the centre. Radiative transfer modelling shows the radiation temperatures for the three isotopologues at a range of extinctions in Fig. 2.6. These results were determined using the RADEX radiative transfer code with a kinetic temperature of 10 K, a molecular hydrogen density of 10^5 cm^{-3} and column densities corresponding to A_V = 1 to 6. RADEX is a one-dimensional radiative transfer code based on the escape probability method (van der Tak et al., 2007).

The excitation temperature (T_{ex}) of the optically thick ^{12}CO emission was estimated as 5 – 20 K since several of the targets are starless and likely to be cold. The main beam temperature (T_{mb}) was therefore also 5 – 20 K for ^{12}CO. A signal-to-noise ratio of 10 – 20 was requested, which is around 0.5 K *rms* T_{mb}.

2.3 JAMES CLERK MAXWELL TELESCOPE

The 15 m James Clerk Maxwell Telescope (JCMT) is the world's largest telescope optimised for observing submillimetre wavelengths. It is located at an altitude of 4092 m near the summit of Mauna Kea, Hawai'i, and was operated by the United Kingdom and Canada when the observations were carried out. The dry and stable atmosphere on Mauna Kea makes it one of the most sought-after observing sites in the world. Fig. 2.7 shows some of the 13 internationally funded telescopes at the summit. The JCMT is housed in a dome, the upper section of which contains the control room and rotates with the antenna (Fig. 2.8). During normal operation the antenna is covered by a Gore-Tex membrane, transparent at submillimetre wavelengths, which provides protection from the sun, wind and dust (Fig. 2.9).

FIGURE 2.8. The James Clerk Maxwell Telescope on Mauna Kea

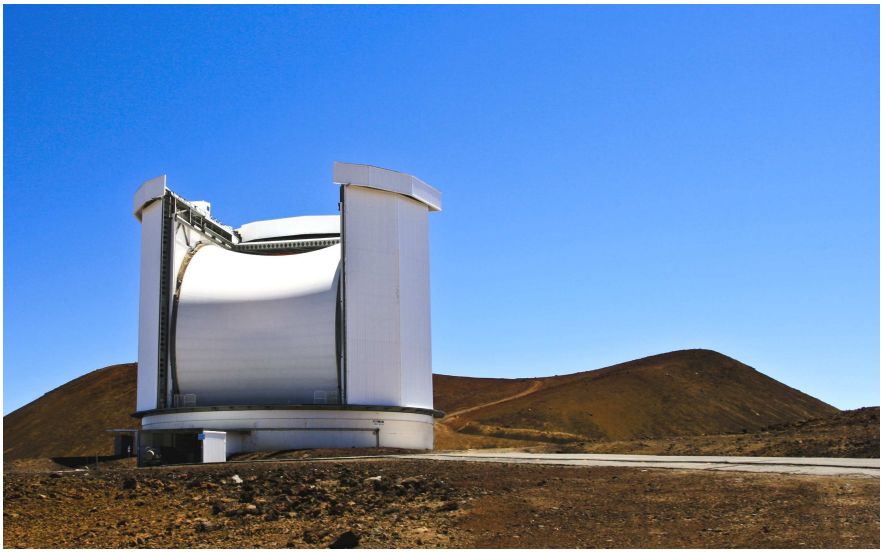

FIGURE 2.9. The James Clerk Maxwell Telescope with its Gore-Tex membrane.

Observers and support scientists live at Hale Pohaku, halfway up the mountain, and make the 30 minute trip to the summit each night. Observations are carried out in a single 12 hour shift running from 7.30pm to 7.30am. Altitude sickness is a serious concern on Mauna Kea so observers must attend a safety briefing and spend a night at Hale Pohaku to acclimatise before travelling to the summit.

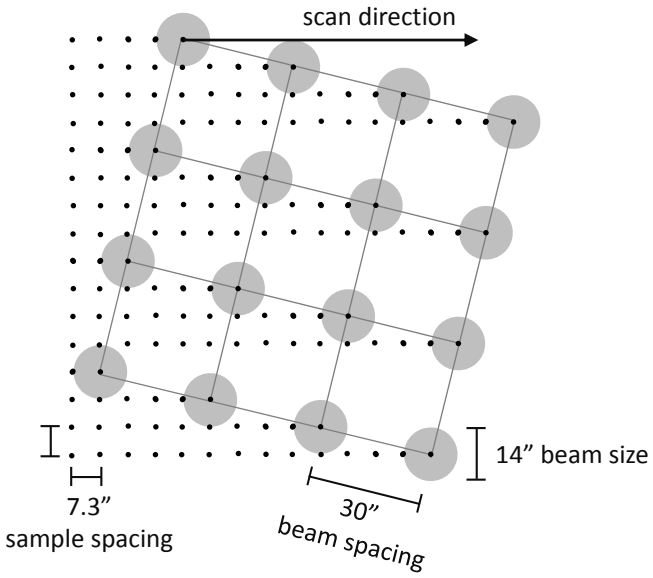

FIGURE 2.10. The HARP mapping pattern with 14 arcsec beamsize, 30 arcsec beam spacing and 7.3 arcsec sample spacing. Figure adapted from (Buckle et al., 2009).

TABLE 2.4. CO $J = 3 \rightarrow 2$ lines observed with HARP at the JCMT

Isotopologue	Frequency (GHz)	Wavelength (mm)
^{12}CO	345.8	0.87
^{13}CO	330.6	0.91
C^{18}O	329.3	0.91

2.3.1 HETERODYNE ARRAY RECEIVER PROGRAM

The Heterodyne Array Receiver Program (HARP) instrument at the JCMT is a 16 (4×4) element heterodyne array receiver operating in the submillimetre range from 325 to 375 GHz (Smith et al. (2008), Buckle et al. (2009)). It is ideally suited to mapping the $J = 3 \rightarrow 2$ transitions of the CO isotopologues listed in Table 2.4. The beamsize of each receiver is around 14 arcsec (and related to the observed frequency); 30 arcsec spacing gives the array a footprint of 2×2 arcmin (see Fig. 2.10). Although the space between receivers is larger than the beamsize, HARP can produce a fully-sampled map by scanning across the sky with the array rotated with respect to the direction of travel, a technique known as raster mapping. Data are collected at 7.3 arcsec intervals. This is the most efficient mapping pattern for observing regions larger than 2×2 arcmin with the JCMT.

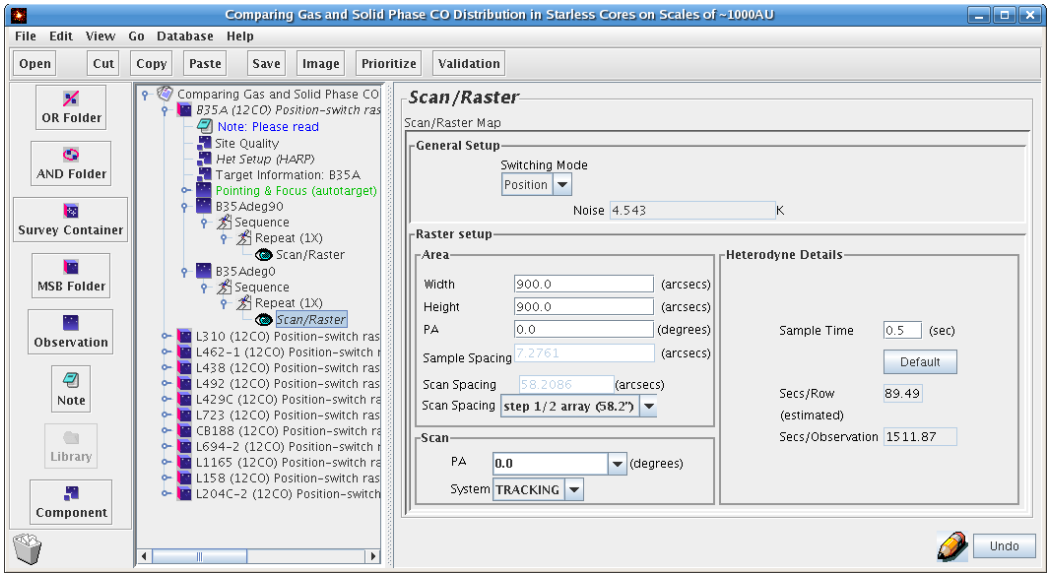

FIGURE 2.11. The JCMT Observing Tool, used to write the set up files for the observations.

2.3.2 JCMT OBSERVATIONS

The author, as 'visiting observer', led both JCMT observing runs for the CO gas mapping project. Observations were set up using Minimum Schedulable Block (MSB) files, written by the author using the JCMT 'Observing Tool', shown in Fig. 2.11. MSBs detail the observing strategy and include the target cloud position, map dimensions, receiver, line frequencies, scan pattern, integration time and weather conditions required. They are the smallest observation blocks the telescope system will schedule and are observed several times until the required signal-to-noise ratio is achieved. During the observing runs, the author selected the MSBs for observation based on their elevation, priority and weather conditions. The JCMT Telescope Support Scientist (TSS) was responsible for operating the telescope and ensuring that efficient use was made of the available time. The TSS calibrated the instruments and adjusted the telescope pointing and focus as necessary between MSBs using nearby sources. The weather was closely monitored throughout the night. Fig. 2.12 is an example of the atmospheric opacity over the course of a shift. The acceptable range for the CO observations is marked in blue. When the weather deteriorated and the atmospheric opacity increased, backup projects from the UK queue were observed.

The CO emission lines listed in Table 2.4 were mapped using HARP and the ACSIS (Auto-Correlation Spectrometer and Imaging System) digital autocorrelation spectrometer across 14.6 $\times$ 14.6 arcmin regions centred on the nine starless and star form-

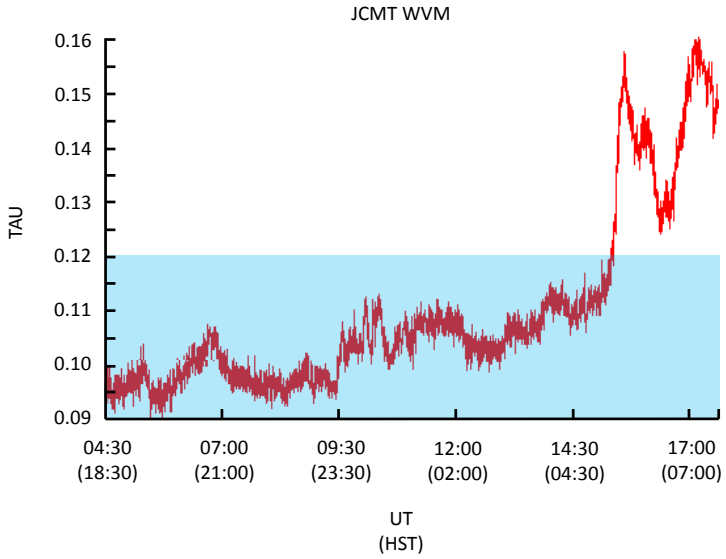

FIGURE 2.12. Atmospheric opacity (τ) measured by the Water Vapor Monitor (WVM) during a shift at the JCMT. The acceptable range for the gas-solid mapping project CO observations is marked in blue. Around 5am the weather deteriorated and a different project was observed until the end of the shift.

TABLE 2.5. Molecular clouds observed with HARP (CO $J = 3 \rightarrow 2$) at the JCMT

Cloud	Isotopologues Observed		
B35A	^{12}CO	^{13}CO	C^{18}O
L158	^{12}CO	^{13}CO	C^{18}O
L204C-2	^{12}CO		
L438	^{12}CO		
L492	^{12}CO		
L429C	^{12}CO		
L723	^{12}CO	^{13}CO	C^{18}O
L694-2	^{12}CO	^{13}CO	C^{18}O
L1165	^{12}CO	^{13}CO	C^{18}O

ing molecular clouds listed in Table 2.5. The targets were observed using the position-switch raster-mapping mode, where a nearby off-source reference position is observed during the run and subtracted from the map to eliminate most instrumental and atmospheric effects. Prior to mapping each target, a brief observation was made of its reference position to ensure it was free of CO emission. Each target region was mapped multiple times in orthogonal directions and the data were combined. This technique is known as 'basket-weaving' and reduces the striping effect, often seen in single-scan maps, which is caused by non-uniform receiver responses. At the time of the first observations in 2007, HARP had two dead receivers so the array was moved

FIGURE 2.13. The IRAM 30 m Telescope coloured by the sunset.

in half-array steps to ensure full coverage. By the second observing run in 2008, two further receivers were dead and the spacing was modified to quarter-array steps. The integration time was reduced by half, resulting in a similar mapping time with slightly reduced signal-to-noise ratio. Observations of the ^{13}CO and C^{18}O $J = 3 \rightarrow 2$ lines were made simultaneously in Single Side Band (SSB) mode with two spectral regions and 250 MHz bandwidth, resulting in a spectral resolution of 60 kHz or 0.06 km s^{-1}. The ^{12}CO observations also used the SSB mode and 250 MHz bandwidth, resulting in a spectral resolution of 31 kHz (0.027 km s^{-1}). These high spectral resolutions allowed rebinning of the data to an acceptable lower resolution, which significantly improved the signal-to-noise ratios of the maps. The full data reduction procedure is described in Section 3.1.1.

2.4 INSTITUT DE RADIO ASTRONOMIE MILLIMÉTRIQUE 30 M TELESCOPE

The Institut de Radio Astronomie Millimétrique (IRAM) 30 m Telescope, shown in Fig. 2.13, is located on Pico Veleta in the Spanish Sierra Nevada mountains at an altitude of 2850 m. It is supported by INSU/CNRS (France), MPG (Germany) and IGN (Spain). The telescope has a diameter of 30 m and, unlike the JCMT, stands open to the elements. Its altitude and location mean the weather conditions are typically less

FIGURE 2.14. The IRAM 30 m Telescope parked on a very wet day.

favourable than at the JCMT; occasionally the telescope must be parked until conditions improve (e.g. Fig. 2.14). However, when the weather is good, the IRAM 30 m Telescope operates continuously and observations are made 24 hours a day.

Observing runs are conducted from a building, a few metres from the telescope, which houses the a control room and accommodation for visiting observers and support staff. In winter, the observatory is reached using the nearby ski lift and IRAM snowcat (Fig. 2.15).

2.4.1 HETERODYNE RECEIVER ARRAY

The HEterodyne Receiver Array (HERA) consists of two arrays of nine (3×3) receivers. These arrays, HERA1 and HERA2, point at the same location but have orthogonal polarisations and separate local oscillators and can therefore be tuned to two frequencies simultaneously. HERA operates between 215 and 272 GHz (Schuster et al., 2004) and is therefore well suited to observing the $J = 2 \rightarrow 1$ transitions of CO, listed in Table 2.6. The receiver spacing is 24 arcsec, around twice the 11 arcsec beamsize at 230 GHz. HERA is used in conjunction with with the VErsatile SPectrometer Array (VESPA).

FIGURE 2.15. During the winter, the IRAM 30 m Telescope is accessed using a ski lift and snowcat.

TABLE 2.6. CO $J = 2 \rightarrow 1$ lines observed with HERA at the IRAM 30 m Telescope

Isotopologue	Frequency (GHz)	Wavelength (mm)
^{12}CO	230.5	1.30
^{13}CO	220.4	1.36
C^{18}O	219.6	1.37

TABLE 2.7. Molecular clouds observed with HERA (CO $J = 2 \rightarrow 1$) at the IRAM 30 m Telescope

Cloud	Isotopologues Observed		
B35A	^{12}CO	^{13}CO	C^{18}O
L158	^{12}CO	^{13}CO	C^{18}O
L204C-2	^{12}CO		
L438	^{12}CO		
L492	^{12}CO		
L429C	^{12}CO		
L723	^{12}CO	^{13}CO	C^{18}O
L694-2	^{12}CO	^{13}CO	C^{18}O
L1165	^{12}CO	^{13}CO	C^{18}O

2.4.2 IRAM 30 M TELESCOPE OBSERVATIONS

The $J = 2 \rightarrow 1$ transitions of the three CO isotopologues listed in Table 2.6 were mapped across the molecular clouds listed in Table 2.7 using HERA. The observations were made during 'HERA pool' weeks, when observers for three or four different projects were present at the IRAM 30 m Telescope. The author was the observer responsible for the CO gas mapping project over the course of three HERA pool weeks. The days were divided into three or four 6 – 8 hour shifts, with each visiting observer on duty when their targets were at their highest elevation. All projects were ranked by the TAC and were observed in order of priority, when weather conditions allowed. This meant that the author was occasionally responsible for observing other projects.

Observing macros were prepared by the author prior to the observing run; examples are shown in Fig. 2.16. They are used by the telescope control system to set up the target clouds, CO line frequencies, receivers used on the frontend, spectrometers used on the backend and the mapping strategy. The dual polarisation feature of the HERA receiver was used for simultaneous observations of the ^{12}CO and ^{13}CO lines with a bandwidth of 80 MHz. The fainter C^{18}O line was similarly observed using both HERA arrays.

Observations were made using the 'oversampled On-The-Fly (OTF) mapping' mode, illustrated in Fig. 2.17. The telescope antenna sweeps over the sky, collecting data at a high rate while recording the position; a fast way of mapping large areas. HERA is rotated by 9.5° to the scan direction, causing the receivers in each row to overlap but leaving a gap between the rows. The array is then moved perpendicular to the scan direction by 12 arcsec and a second scan is done to fill the gaps in the first.

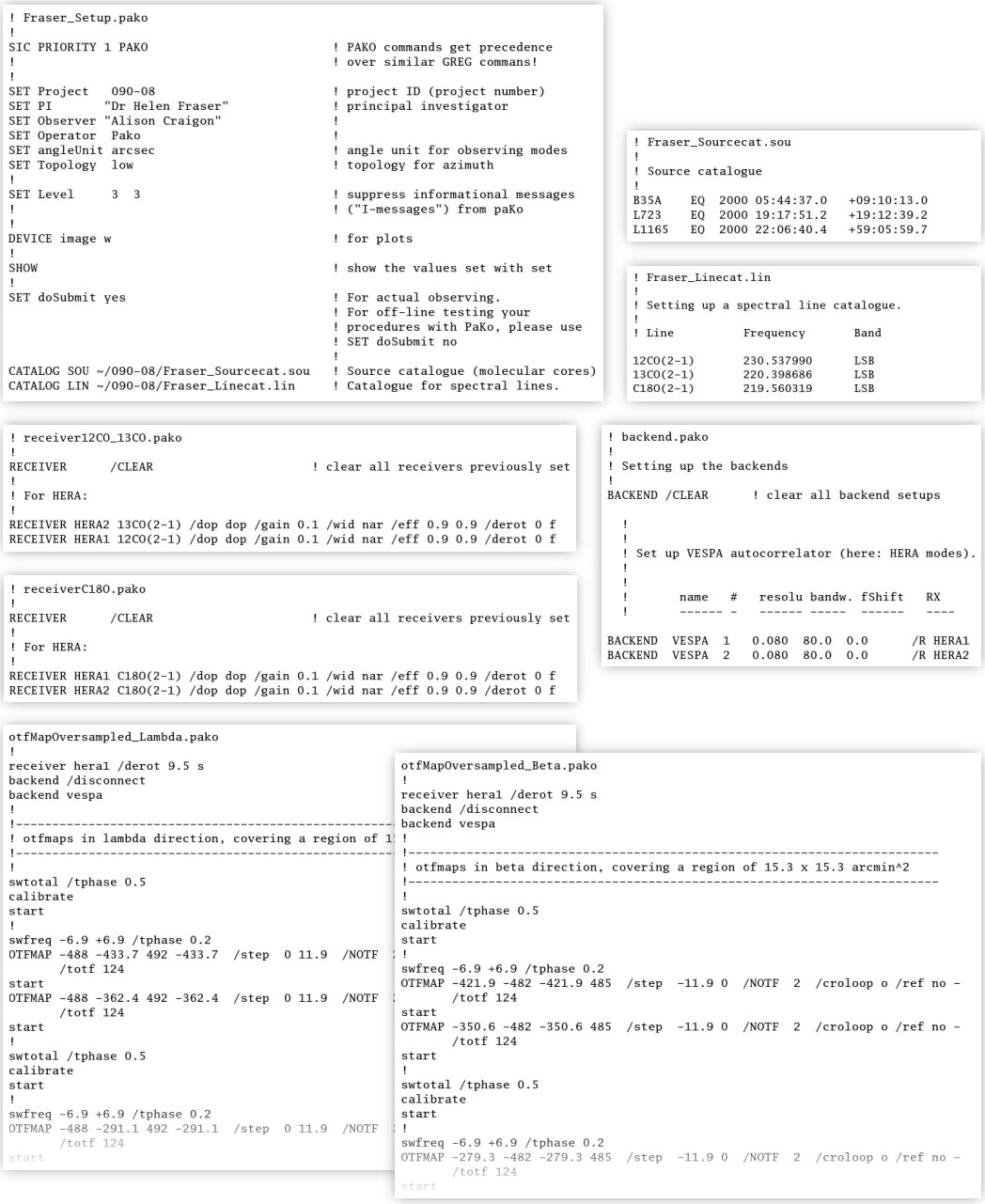

```
! Fraser_Setup.pako
!
SIC PRIORITY 1 PAKO                          ! PAKO commands get precedence
!                                            ! over similar GREG commans!
!
SET Project   090-08                         ! project ID (project number)
SET PI       "Dr Helen Fraser"               ! principal investigator
SET Observer "Alison Craigon"                !
SET Operator  Pako                           !
SET angleUnit arcsec                         ! angle unit for observing modes
SET Topology  low                            ! topology for azimuth
!
SET Level     3  3                           ! suppress informational messages
!                                            ! ("I-messages") from paKo
!
DEVICE image w                               ! for plots
!
SHOW                                         ! show the values set with set
!
SET doSubmit yes                             ! For actual observing.
                                             ! For off-line testing your
                                             ! procedures with PaKo, please use
                                             ! SET doSubmit no
                                             !
CATALOG SOU ~/090-08/Fraser_Sourcecat.sou    ! Source catalogue (molecular cores)
CATALOG LIN ~/090-08/Fraser_Linecat.lin      ! Catalogue for spectral lines.
```

```
! Fraser_Sourcecat.sou
!
! Source catalogue
!
B35A    EQ  2000 05:44:37.0   +09:10:13.0
L723    EQ  2000 19:17:51.2   +19:12:39.2
L1165   EQ  2000 22:06:40.4   +59:05:59.7
```

```
! Fraser_Linecat.lin
!
! Setting up a spectral line catalogue.
!
! Line          Frequency       Band

12CO(2-1)       230.537990      LSB
13CO(2-1)       220.398686      LSB
C18O(2-1)       219.560319      LSB
```

```
! receiver12CO_13CO.pako
!
RECEIVER      /CLEAR                     ! clear all receivers previously set
!
! For HERA:
!
RECEIVER HERA2 13CO(2-1) /dop dop /gain 0.1 /wid nar /eff 0.9 0.9 /derot 0 f
RECEIVER HERA1 12CO(2-1) /dop dop /gain 0.1 /wid nar /eff 0.9 0.9 /derot 0 f
```

```
! backend.pako
!
! Setting up the backends
!
BACKEND /CLEAR      ! clear all backend setups

  !
  !
  ! Set up VESPA autocorrelator (here: HERA modes).
  !
  !
  !       name   #   resolu bandw. fShift   RX
  !       ------ -   ------ -----  ------   ----

BACKEND  VESPA  1   0.080  80.0  0.0      /R HERA1
BACKEND  VESPA  2   0.080  80.0  0.0      /R HERA2
```

```
! receiverC18O.pako
!
RECEIVER      /CLEAR                     ! clear all receivers previously set
!
! For HERA:
!
RECEIVER HERA1 C18O(2-1) /dop dop /gain 0.1 /wid nar /eff 0.9 0.9 /derot 0 f
RECEIVER HERA2 C18O(2-1) /dop dop /gain 0.1 /wid nar /eff 0.9 0.9 /derot 0 f
```

```
otfMapOversampled_Lambda.pako
!
receiver hera1 /derot 9.5 s
backend /disconnect
backend vespa
!
!-------------------------------------------------------
! otfmaps in lambda direction, covering a region of 1
!-------------------------------------------------------
!
swtotal /tphase 0.5
calibrate
start
!
swfreq -6.9 +6.9 /tphase 0.2
OTFMAP -488 -433.7 492 -433.7  /step  0 11.9  /NOTF
       /totf 124
start
OTFMAP -488 -362.4 492 -362.4  /step  0 11.9  /NOTF
       /totf 124
start
!
swtotal /tphase 0.5
calibrate
start
!
swfreq -6.9 +6.9 /tphase 0.2
OTFMAP -488 -291.1 492 -291.1  /step  0 11.9  /NOTF
       /totf 124
start
```

```
otfMapOversampled_Beta.pako
!
receiver hera1 /derot 9.5 s
backend /disconnect
backend vespa
!
!-------------------------------------------------------------------------
! otfmaps in beta direction, covering a region of 15.3 x 15.3 arcmin^2
!-------------------------------------------------------------------------
!
swtotal /tphase 0.5
calibrate
start
!
swfreq -6.9 +6.9 /tphase 0.2
OTFMAP -421.9 -482 -421.9 485  /step  -11.9 0  /NOTF  2  /croloop o /ref no -
       /totf 124
start
OTFMAP -350.6 -482 -350.6 485  /step  -11.9 0  /NOTF  2  /croloop o /ref no -
       /totf 124
start
!
swtotal /tphase 0.5
calibrate
start
!
swfreq -6.9 +6.9 /tphase 0.2
OTFMAP -279.3 -482 -279.3 485  /step  -11.9 0  /NOTF  2  /croloop o /ref no -
       /totf 124
start
```

FIGURE 2.16. Examples of the macros used for a typical observing session at the IRAM 30 m Telescope.

The maps were frequency-switched with a 6.9 MHz throw using the VESPA backend. Frequency-switching eliminates the need to move the telescope off-source, increasing the on-source integration time. The local oscillator (LO) is switched from its original frequency ν^0_{LO} to a frequency shifted by a few MHz ($\nu^0_{LO} \pm \Delta\nu_{LO}$); the resulting spectra show both the original CO emission signal and a negative-amplitude signal,

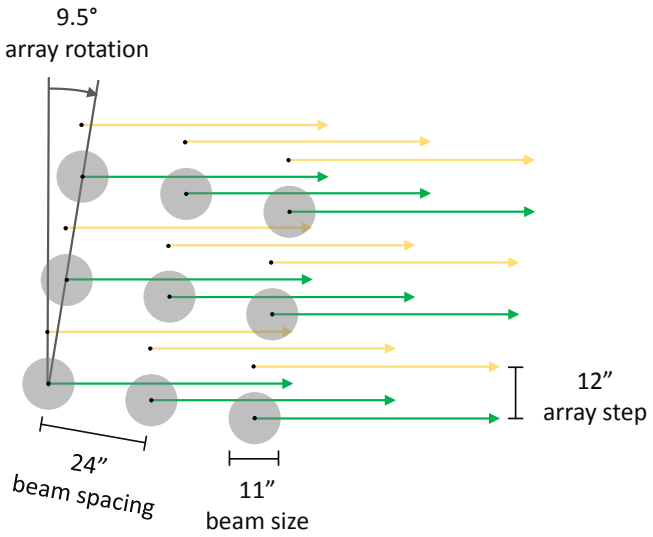

FIGURE 2.17. The HERA oversampled On-The-Fly mapping pattern used to observe the clouds. The array is rotated by 9.5° to the scan direction. This orientation leaves a gap which is subsequently filled by moving the array up by 12 arcsec and performing a second scan (yellow).

separated by $\Delta\nu_{LO}$. The negative-amplitude signal is then 'folded' into the original signal during the data reduction procedure, described in Section 3.1.2.

Visiting observers were encouraged by the support staff to become fully competent in the telescope operating procedures. As the telescope is operational 24 hours a day, the staff are often away from the control room to eat and sleep. The author learned to use the telescope control system, 'PaKo', and ran many of the observations independently.

Fig. 2.18 shows the PaKo commands used for a typical observing session. At the start of the session, the project macro files were loaded. A calibration observation was then performed by observing an 'on sky' position, an ambient temperature load (the 'hot' load) and a 'cold' load. The results were used for calibration of the HERA intensity scale. The accuracy of the telescope azimuth and elevation positioning ('pointing') was then checked and minor corrections were made as necessary. The telescope was then focused by making small adjustments to the subreflector position to maximise the intensity of the radiation on the receiver. A strong source was selected for calibration, pointing and focus; planets are best but those larger than the beamsize cannot be used to focus. Mars and Uranus are suitable and were used on most occasions. A second pointing source was then observed close to the target cloud (within 10° of elevation) and the pointing values were updated if required. The target cloud was selected and the OTF mapping macro was loaded to begin observations. The two mapping macros, named beta and lambda in reference to their orthogonal scan directions, were observed

```
Observing Procedure - Project 090-08

@~/090-08/setup
@~/090-08/receiver12CO_13CO             !(or receiverC18O)
@~/090-08/backend
q                                       !to exit loop leaving cont. backend in place
swtotal                                 !total power for cal
source uranus                           !pick a pointing & focus source e.g. Uranus
cal                                     !will have to be tuned
cal                                     !repeat cal after tuning
swbeam                                  !beam switching for pointing and focus
point
set point x y                           !set pointing
focus
set focus a                             !set focus
source 1749+096 /cata *                 !pick a pointing source near the target (within 10deg elev)
point
set point x y                           !set pointing
source L1165                            !input source
@~/090-08/backend
c                                       !to continue the loop and use Vespa backends
@~/090-08/otfMapOversampled_Beta.pako   !Begin observation. This will take ~1.1 hours
                                        !-after 1 scan, check derotator: Mira> view /derot 9.5 s
source 1749+096 /cata *                 !pick a pointing source near the target (within 10deg elev)
point
@~/090-08/otfMapOversampled_Lambda.pako !Begin observation. This will take ~1.1 hours
                                        !-after 1 scan, check derotator: Mira> view /derot 9.5 s
source 1749+096 /cata *                 !pick a pointing source near the target (within 10deg elev)
point
```

FIGURE 2.18. The PaKo commands used during a typical observing session at the IRAM 30 m Telescope.

several times for each cloud until the required signal-to-noise ratio was achieved. The telescope pointing was checked every hour between mapping macros, or more often if the target moved more than 10° in an hour. The focus was measured every three to four hours. Care was taken in scheduling observations around sunrise and sunset when the atmosphere can become unstable due to temperature changes. Multiple shorter duration OTF maps were made when the atmospheric stability was poor. The weather was monitored closely throughout the run and observations were made for a different project if the PWV and τ reached unacceptable values for the CO gas mapping project.

2.5 NOBEYAMA 45 M RADIO TELESCOPE

The Nobeyama 45 m Radio Telescope is situated at an elevation of 1350 m in the mountains of Japan's Nagano prefecture (Fig. 2.19). It is part of the Nobeyama Radio Observatory (NRO), run by the National Astronomical Observatory of Japan (NAOJ), which also includes the Nobeyama Radioheliograph, the Nobeyama Millimeter Array and the Nobeyama Radio Polarimeter (Fig. 2.20). The telescope is operational 24 hours a day and visiting observers are allocated a time slot based on the visibility of their sources. Observers and support scientists live in the dormitory building on site.

FIGURE 2.19. The Nobeyama 45 m Radio Telescope (image courtesy of NAOJ).

FIGURE 2.20. The Nobeyama Radio Observatory (image courtesy of NAOJ).

TABLE 2.8. CO $J = 1 \rightarrow 0$ lines observed with BEARS at the Nobeyama 45 m Radio Telescope

Isotopologue	Frequency (GHz)	Wavelength (mm)
^{12}CO	115.3	2.60
^{13}CO	110.2	2.72
C^{18}O	109.8	2.73

2.5.1 25-BEAM ARRAY RECEIVER SYSTEM

BEARS is a 25 (5 $\times$ 5) heterodyne receiver array operating at frequencies of 82 – 116 GHz (Sunada et al., 2000). It was installed on the telescope in April 1998 and is capable of mapping the $J = 1 \rightarrow 0$ transitions of the three CO isotopologues listed in Table 2.8. The beamsize is 15 arcsec at 115 GHz and the receivers are separated by 41.1 arcsec.

2.5.2 NOBEYAMA 45 M RADIO TELESCOPE OBSERVATIONS

As principle investigator and visiting observer for this project, the author worked alongside the observatory staff to learn the procedures for operating the telescope and receivers. This allowed the author to conduct observations with minimal assistance from the support astronomers.

Starless core L438 is the only object in the CO gas mapping project to have been observed with BEARS at the Nobeyama 45 m Radio Telescope. The autocorrelator spectrometer (Sorai et al., 2000) with 32 MHz bandwidth and 1024 channels was used as the backend. Observations began by tuning to the frequency of the relevant CO isotopologue, listed in Table 2.8. The S40 receiver then observed SiO maser IRC10414 (a source with strong emission) to determine whether the telescope pointing was accurate. Any change required in azimuth or elevation was entered into the system. The pointing was checked both before and between observations since the telescope can drift by several arcseconds. The wind speed was monitored closely throughout the observing run as it is one of the factors responsible for the drift.

The BEARS footprint was sufficient to cover the 400 $\times$ 400 arcsec target area in a 2 $\times$ 2 mosaic of maps. For each map, the sky was fully sampled using a 5 $\times$ 5 pattern with 8 arcsec spacing (see Fig. 2.21). Different noise levels in the receivers can cause mapping artefacts (high and low intensity patches), so the maps combined data from

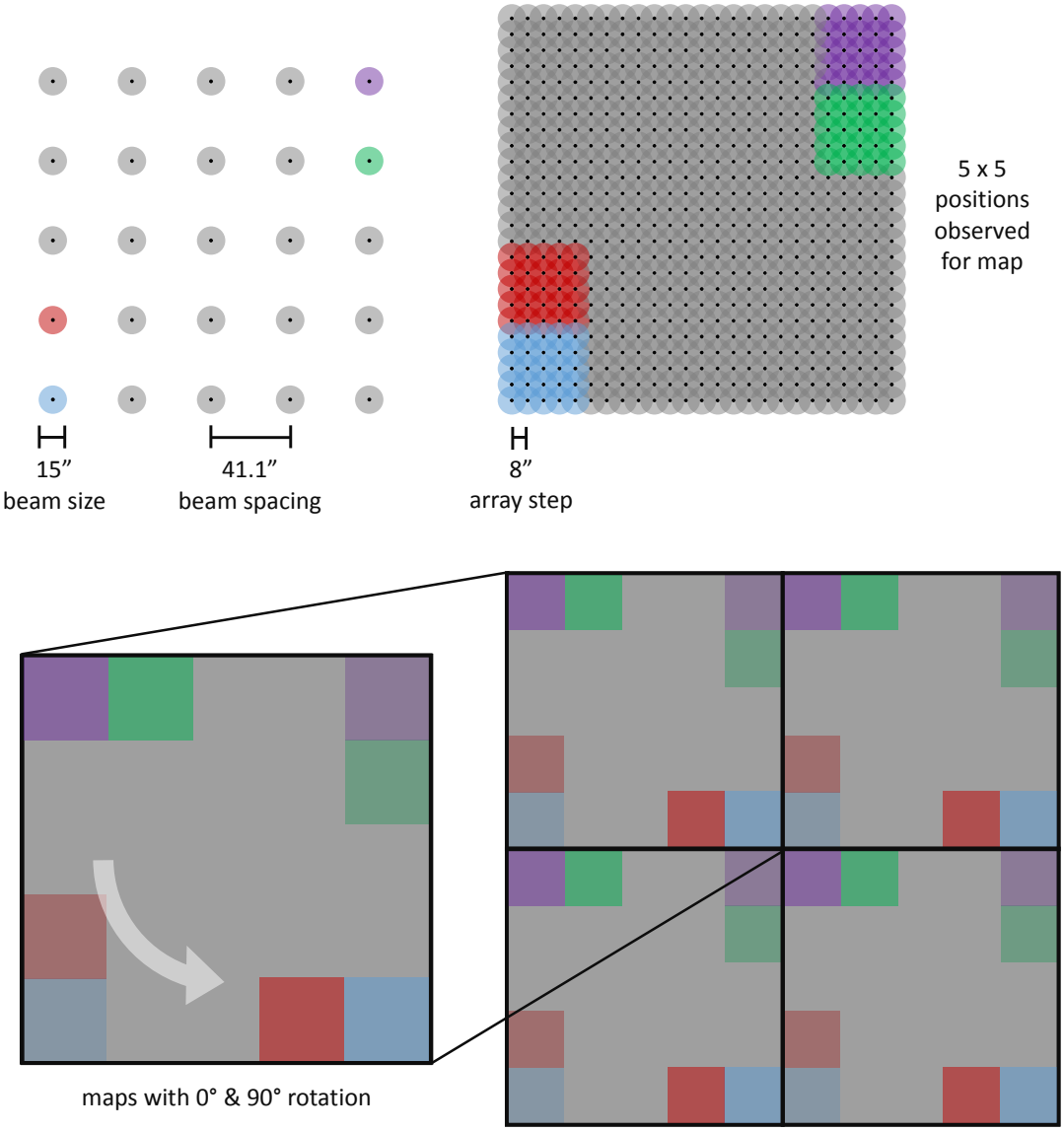

FIGURE 2.21. The BEARS mapping pattern used to observe L438. Four receivers are coloured to illustrate the pattern. Four individual sections were observed, each with 5×5 beam positions at both 0° and 90° array rotations to ensure full sampling.

both 0° and 90° array orientations to mitigate this effect. The ^{12}CO observations were made using the position-switching mode. However, ^{12}CO emission was later found in the reference position. To correct the ^{12}CO map, the reference position was observed in frequency-switching mode and the effect of the ^{12}CO emission was removed from the L438 map. The subsequent ^{13}CO and C^{18}O observations of L438 used the frequency-switching mode as it was not possible to find a region free of CO within switching distance.

TABLE 2.9. All observations made in the course of this PhD

Cloud	JCMT HARP $J = 3 \rightarrow 2$			IRAM HERA $J = 2 \rightarrow 1$			Nobeyama BEARS $J = 1 \rightarrow 0$		
B35A	^{12}CO	^{13}CO	C^{18}O	^{12}CO	^{13}CO	C^{18}O			
L158	^{12}CO	^{13}CO	C^{18}O	^{12}CO	^{13}CO	C^{18}O			
L204C-2	^{12}CO			^{12}CO					
L310									
L462-1									
L438	^{12}CO			^{12}CO			^{12}CO	^{13}CO	C^{18}O
L492	^{12}CO			^{12}CO					
L429C	^{12}CO			^{12}CO					
L723	^{12}CO	^{13}CO	C^{18}O	^{12}CO	^{13}CO	C^{18}O			
CB188									
L694-2	^{12}CO	^{13}CO	C^{18}O	^{12}CO	^{13}CO	C^{18}O			
L1165	^{12}CO	^{13}CO	C^{18}O	^{12}CO	^{13}CO	C^{18}O			

Instrument calibration data for the observed spectral lines was supplied by the observatory. Each season BEARS is calibrated by observing a source with strong line intensity and a good signal-to-noise ratio (such as W3 or W51). The source is first observed using the S100 receiver, which has a frequency range and beamsize similar to BEARS. Each of the BEARS receivers then observes the source and scaling factors are obtained. These scaling factors are applied to the BEARS observations in the data reduction procedure, which is described in Section 3.1.3.

2.6 SUMMARY

In the course of this PhD, the author was responsible for six successful telescope time proposals. These proposals included both a scientific justification for the wider gas-solid mapping project and a technical justification for the planned observing strategy. Target molecular clouds were selected based on their elevations during the observing season. The instruments and scanning patterns available at each telescope were investigated and optimum observing strategies were devised. For each map, the required integration time was calculated based on the scanning pattern, the CO isotopologues and transitions, and the likely weather conditions during the season.

A total of 206 hours of telescope time was awarded to the CO gas mapping project for observing three transitions of three isotopologues of CO across starless and star forming clouds. Adverse weather conditions meant that observations had to be abandoned

on several occasions and so some remain incomplete. Nine of the target clouds were observed in at least two transitions ($J = 3 \rightarrow 2$ and $J = 2 \rightarrow 1$) of ^{12}CO and six clouds were observed in two transitions of all three isotopologues. Table 2.9 summarises the completed observations.

Having conducted six observing runs, the author has become familiar with the control systems of the JCMT, the IRAM 30 m Telescope and Nobeyama 45 m Radio Telescope, and is now considered an 'experienced observer'.

REFERENCES

Buckle J. V., Hills R. E., Smith H., Dent W. R. F., Bell G., Curtis E. I., Dace R., Gibson H., Graves S. F., Leech J., Richer J. S., et al., 2009, MNRAS, pp 1026–1043 45

Chini R., 1981, A&A, 99, 346 36

Dame T. M., Thaddeus P., 1985, ApJ, 297, 751 36

Herbig G. H., Jones B. F., 1983, AJ, 88, 1040 36

Liebe H. J., 1989, International Journal of Infrared and Millimeter Waves, 10, 631 41

Noble J. A., 2011, PhD thesis, University of Strathclyde, Department of Physics 34

Noble J. A., Fraser H. J., Aikawa Y., Pontoppidan K. M., Sakon I., 2013, ApJ, 775, 85 34

Pardo J. R., Cernicharo J., Serabyn E., Wiedner M. C., 2009, in Lis D. C., Vaillancourt J. E., Goldsmith P. F., Bell T. A., Scoville N. Z., Zmuidzinas J., eds, Submillimeter Astrophysics and Technology: a Symposium Honoring Thomas G. Phillips Vol. 417 of Astronomical Society of the Pacific Conference Series, Contribution of the CSO to our Knowledge of the Atmospheric Opacity and Phase Delay at Submillimeter Wavelengths. Application to the ALMA Project. p. 125 41

Schuster K.-F., Boucher C., Brunswig W., Carter M., Chenu J.-Y., Foullieux B., Greve A., John D., et al., 2004, A&A, 423, 1171 49

Smith H., Buckle J., Hills R., Bell G., Richer J., Curtis E., Withington S., Leech J., et al., 2008, in SPIE Conference Series Vol. 7020, HARP: a submillimetre heterodyne array receiver operating on the James Clerk Maxwell Telescope 45

Sorai K., Sunada K., Okumura S. K., Tetsuro I., Tanaka A., Natori K., Onuki H., 2000, in Butcher H. R., ed., Society of Photo-Optical Instrumentation Engineers (SPIE) Conference Series Vol. 4015 of Society of Photo-Optical Instrumentation Engineers (SPIE) Conference Series, Digital spectrometers for the Nobeyama 45-m telescope. pp 86–95 56

Straižys V., Černis K., Bartašiūtė S., 2003, A&A, 405, 585 36

Sunada K., Yamaguchi C., Nakai N., Sorai K., Okumura S. K., Ukita N., 2000, in Society of Photo-Optical Instrumentation Engineers (SPIE) Conference Series Vol. 4015, BEARS: SIS 25-beam array receiver system for the NRO 45-m telescope. pp 237–246 56

Suutarinen A., 2015, PhD thesis, The Open University, Department of Physical Sciences, Astronomy Division 34

van der Tak F. F. S., Black J. H., Schöier F. L., Jansen D. J., van Dishoeck E. F., 2007, A&A, 468, 627 43

CHAPTER 3

ANALYSIS OF OBSERVATIONS OF CO GAS

SYNOPSIS

This chapter details the process for transforming the 'raw' telescope data into maps of CO distribution, velocity and temperature. It begins by describing the data reduction steps necessary to convert the telescope files into data cubes containing the spectra and their locations.

The equations used to analyse the spectral data are then presented. This chapter goes on to describe COROLINE, the suite of software written using these equations to determine the physical parameters of the clouds.

3.1 TELESCOPE DATA REDUCTION

Each telescope operating system produces observation files in a unique format. These files were 'reduced' using telescope-specific software to write standardised 'FITS' (Flexible Image Transport System) files suitable for input into the CO analysis software, which is described in Section 3.3. FITS files contain three dimensional data, with RA and Dec positions recorded in the first two axes and the emission spectra in the third (Hanisch et al., 2001); they are often referred to as FITS cubes. The FITS file header contains details of the observation (e.g. target name, telescope and receiver, observation frequency, resolution, etc.) which are used to construct the maps.

3.1.1 JCMT HARP DATA

The JCMT HARP data reduction was carried out using the Starlink software collection (Rankin et al., 2003). As weather conditions affect the quality of the observations, the author reduced the data while at the telescope on completion of each MSB and monitored the signal-to-noise ratios; subsequent MSBs were then amended as required.

Multiple observations of a cloud, made using the MSBs described in Section 2.3.2, were combined into a single data cube using the 'Smurf' (Jenness et al., 2013) and 'Kappa' (Currie & Berry, 2014) command line tools. The 'makecube' command imports and combines the observation files listed in a text file (e.g. 'B35A_12CO.txt').

makecube in = ^B35A_12CO.txt specbounds = \"-20.0, 40.0\" autogrid = false pixsize = 7.3 out = B35A_12CO badmask = and detectors = ' "h00,h01,h02,h04,h05, h06,h07,h08,h09,h10,h11,h13,h15" '

In this example the high and low velocity ends of each spectrum are removed, leaving only the data between -20.0 and 40.0 km s^{-1}. The raster mapping technique used for the observations requires the 'autogrid' parameter to be set as 'false' and the pixel size set as 7.3 arcsec. HARP receivers 'h03', 'h12' and 'h14' were either dead or extremely noisy and were not included in the final maps.

The resulting FITS cube was then imported into the Starlink 'GAIA' (Graphical Astronomy and Image Analysis) tool (Draper et al., 2014). Fig. 3.1 shows a preliminary CO map of molecular cloud L158 in the GAIA tool. The ragged edges are a consequence of the raster mapping technique, described in Section 2.3.1, and the removal of certain receivers. The map shows the CO emission across the cloud at the velocity

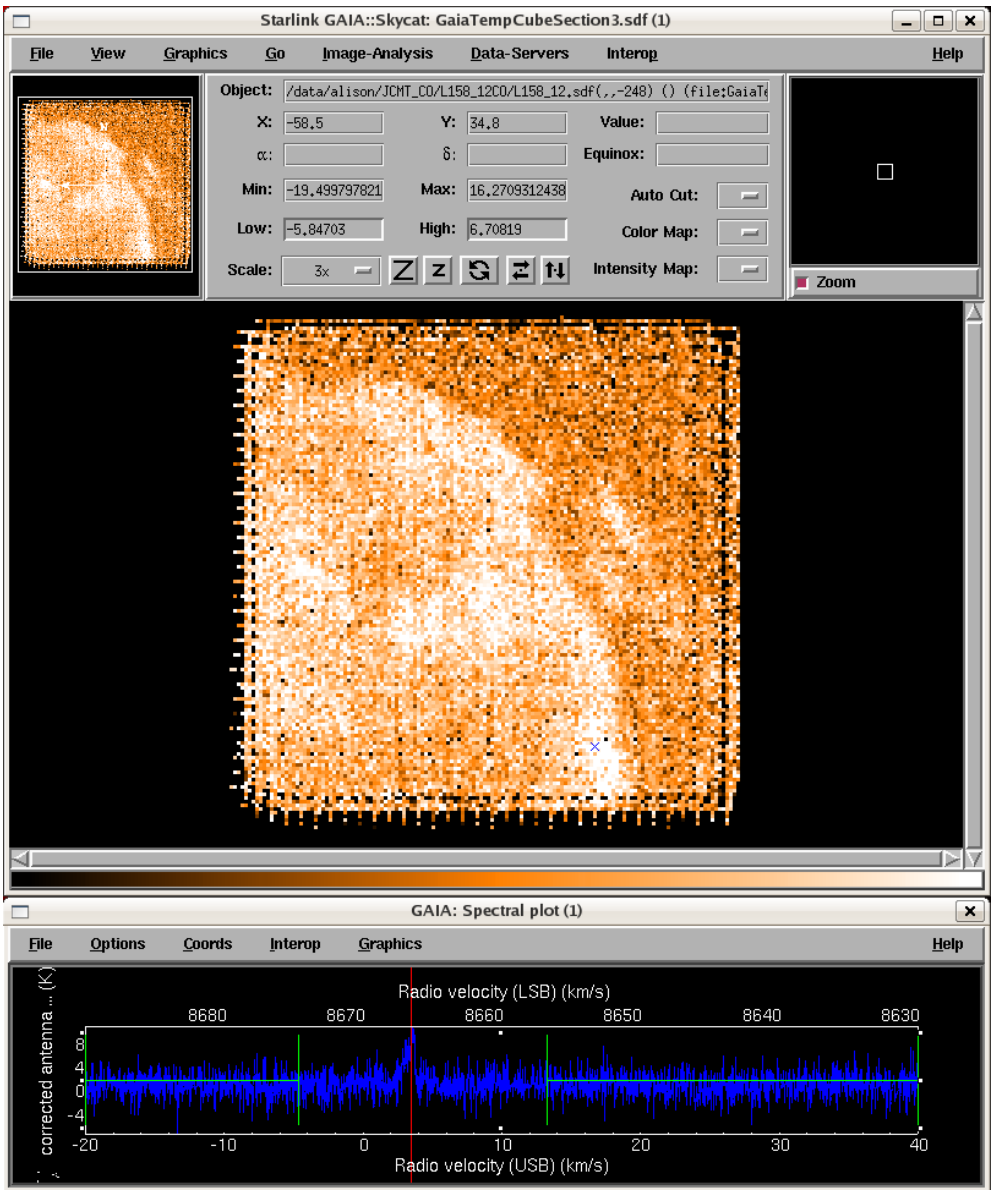

FIGURE 3.1. The Starlink GAIA tool showing first-order baseline removal from a ^{12}CO map of L158.

selected by the red line on the spectrum. The location of this spectrum is indicated by the blue cross on the map. Emission-free regions of the spectrum are marked in green; first order fits to these regions were used to remove linear baselines from the entire map. The spectral data were then re-binned to 0.1 km s^{-1} to improve the signal-to-noise ratio (Fig. 3.2). The resulting spectra were saved as a FITS cube for input into the CO analysis software, which is described in Section 3.3.

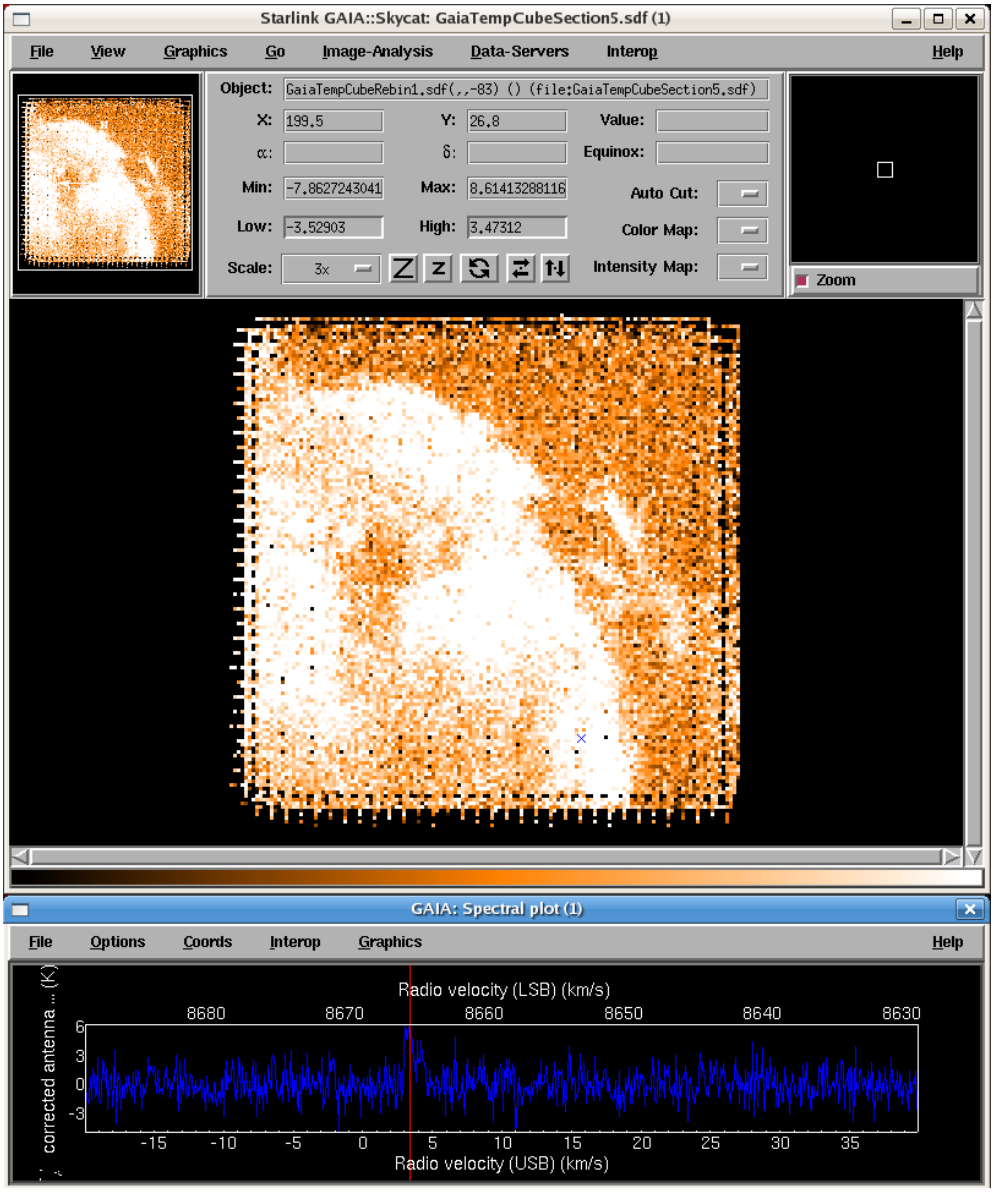

FIGURE 3.2. The Starlink GAIA tool showing baselined and re-binned ^{12}CO spectra in L158.

3.1.2 IRAM 30 M TELESCOPE HERA DATA

The HERA data reduction was carried out by the author at the IRAM 30 m Telescope using the 'CLASS' software (Continuum and Line Analysis Single-dish Software), which is part of the 'GILDAS' collection (Grenoble Image and Line Data Analysis Software, Gildas Team (2013)). The data were frequency folded, using the 'FOLD' command, to obtain the source spectra. Frequency switched observations usually result in data with non-linear baselines; a third order polynomial was found to be a good fit so

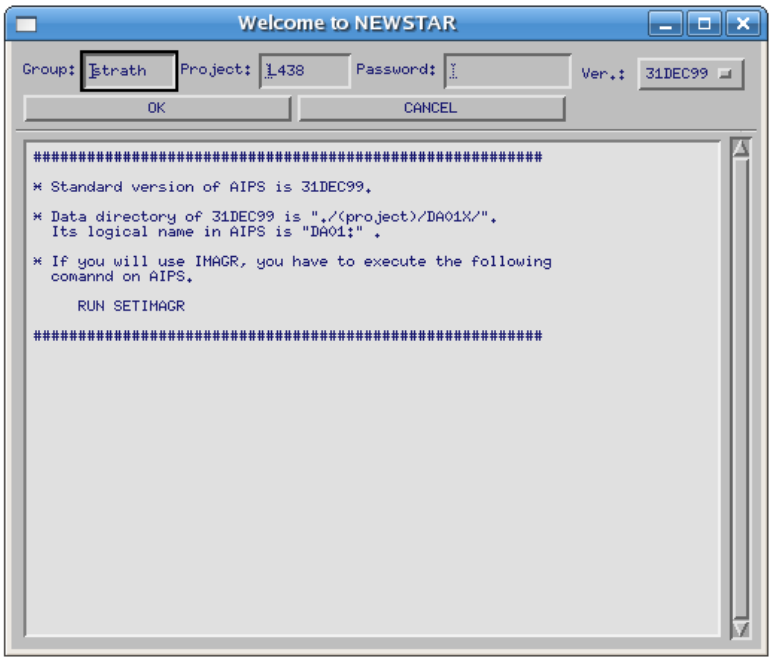

FIGURE 3.3. The NRO NewStar software GUI.

the 'BASE' command was used to remove a third order baseline from all spectra. The 'GRID' and 'GRID_CUBE' commands were used to build a FITS cube of the data. The FITS files were subsequently re-binned to a spectral resolution of 0.1 km s^{-1} and imported into the analysis software detailled in Section 3.3.

3.1.3 NOBEYAMA 45 M RADIO TELESCOPE BEARS DATA

The Nobeyama BEARS observations were reduced using the NRO 'NewStar' software (Ikeda et al., 2001). NewStar was developed at the National Radio Astronomy Observatory (NRAO) and is based on AIPS (Astronomical Image Processing System). The data reduction was carried out by the author during the observing run to ensure the necessary signal-to-noise ratios were achieved.

NewStar is operated via a Graphical User Interface (GUI), shown in Fig. 3.3. The data reduction is performed by a series of NewStar 'TASKs'; the full suite of TASKs is shown in Fig. 3.4. To reduce the BEARS observations, 'GCONV' was used to convert the raw data to spectra and apply the receiver scaling factors to adjust the intensities. For observations conducted in frequency-switching mode, the second step was to fold the spectra using 'Fold Sp', a technique which leads to a $\sqrt{2}$ improvement in signal-to-noise ratio. Baselines were then subtracted from all spectra using 'BASELINE'. It

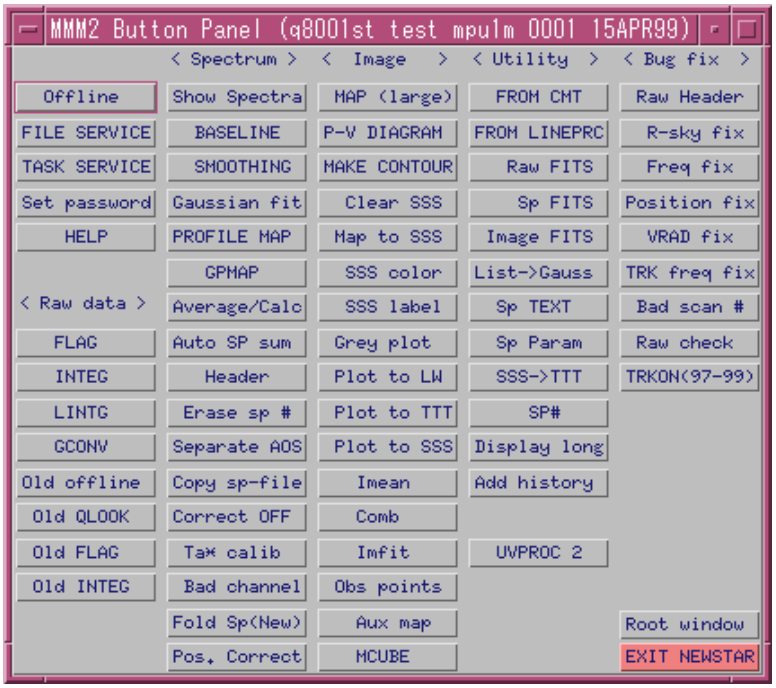

FIGURE 3.4. The TASKs used to reduce the Nobeyama 45 m Radio Telescope data.

was necessary to make minor position corrections to account for the telescope's beam transmission system; this was done using the 'Pos. Correct' TASK. Finally, the spectral data at neighbouring positions were averaged (weighted by their displacements) and a FITS cube of spectral and position data was constructed for the whole cloud using the 'AT for BEARS' TASK.

3.2 CO DATA ANALYSIS METHODS

3.2.1 SPECTRAL ANALYSIS

The CO emission lines in the reduced telescope data were converted to main beam temperature ($T_{\rm mb}$) by dividing the antenna temperatures ($T_{\rm a}^{*}$), stored in the FITS cubes, by the main beam efficiency of the telescope ($\eta_{\rm mb}$), which was 0.75 for the IRAM 30 m Telescope and 0.63 for the JCMT. The fluxes had been calibrated by observing standard objects and the errors were found to be at most 10 per cent. The final error in $T_{\rm mb}$ takes into account both the shot noise and the flux calibration error.

In observational astronomy, emission line frequencies are often found to be offset from their theoretical values (ν_0) due to Doppler shifting in the line of sight. The observed

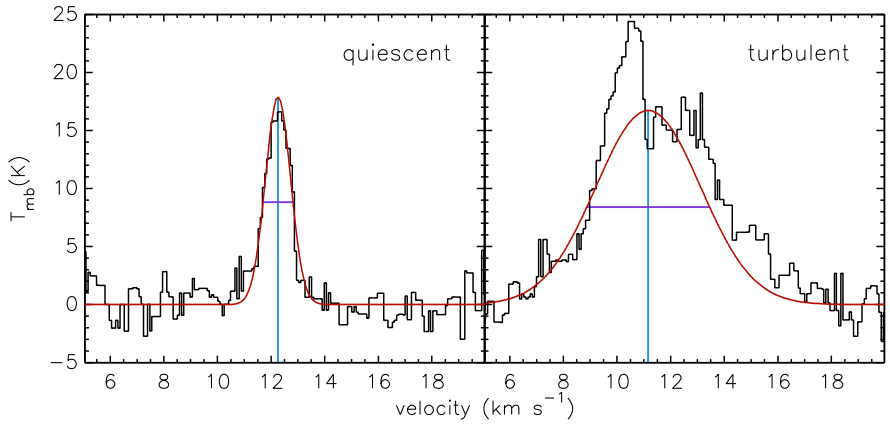

FIGURE 3.5. A Gaussian profile (red) is a good fit to quiescent emission but does not well represent the emission from turbulent gas.

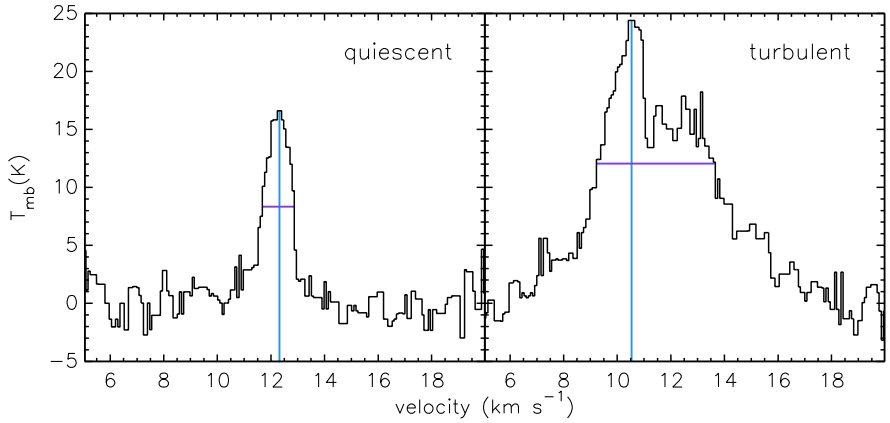

FIGURE 3.6. The peak velocity (blue) and linewidth, or Full-Width at Half-Maximum (FWHM, purple) are measured directly from the emission.

frequencies (ν) can therefore be converted to radial velocities ($v_{\rm r}$), which show the motion of the gas with respect to the local standard of rest ($v_{\rm LSR}$).

$$v_{\rm r} = \frac{{\rm c}(\nu_0 - \nu)}{\nu_0} \ {\rm km\ s^{-1}} \tag{3.1}$$

Quiescent CO gas is identified by a narrow, symmetrical emission line centred at the recession velocity of the cloud. A Gaussian fit to this line provides the parameters required for further analysis of the CO data: peak main beam temperature, peak velocity and linewidth (e.g. Fig. 3.5). However, turbulent gas was evident in many of the observations made for the CO gas mapping project. It appears as a broad emission line encompassing a wide range of velocities, often asymmetrical and with multiple peaks. The complexity of the emission meant that it could not be accurately represented by

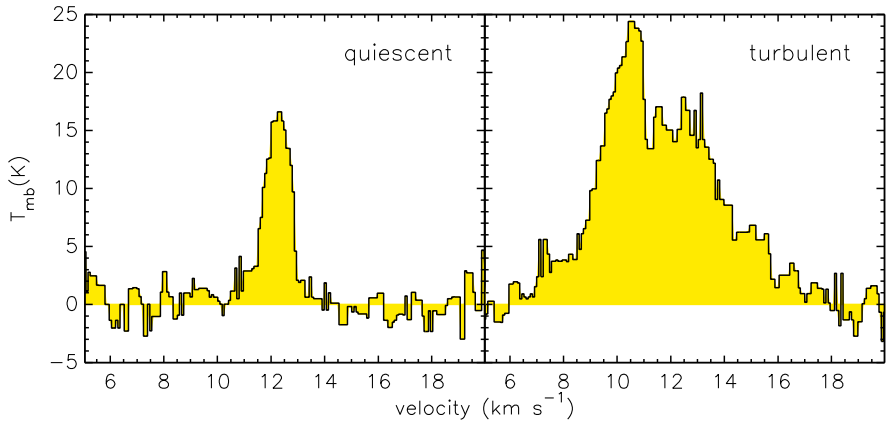

FIGURE 3.7. The integrated intensity of an emission line is the sum of all emission over the specified velocity range.

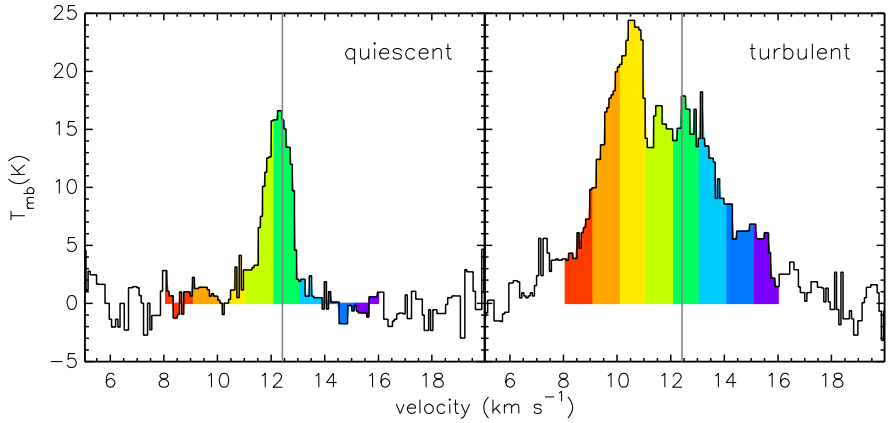

FIGURE 3.8. The integrated intensity of a channel is the sum of all emission over the velocity range of that channel.

a Gaussian, or multiple Gaussians. Instead, the absolute values of peak main beam temperature, peak velocity and linewidth, illustrated in Fig. 3.6, were used.

The integrated intensity of an emission line is the sum of all emission over the specified velocity range, as shown in Fig. 3.7. This value is used in Equation 3.5 to determine the total amount of gas at all velocities in the line of sight.

To investigate the velocity structure of the clouds, the main beam temperature was also integrated over a narrow velocity channel instead of the full width of the line (Fig. 3.8). Multiple maps were then constructed for successive velocity channels, showing how the structure of the cloud varies with velocity (Fig. 3.9). The velocity channel width was typically 0.25 km s^{-1} and covered 3.5 km s^{-1} centred on the mean cloud velocity. This range was sufficient for determining the structure of relatively quiescent gas.

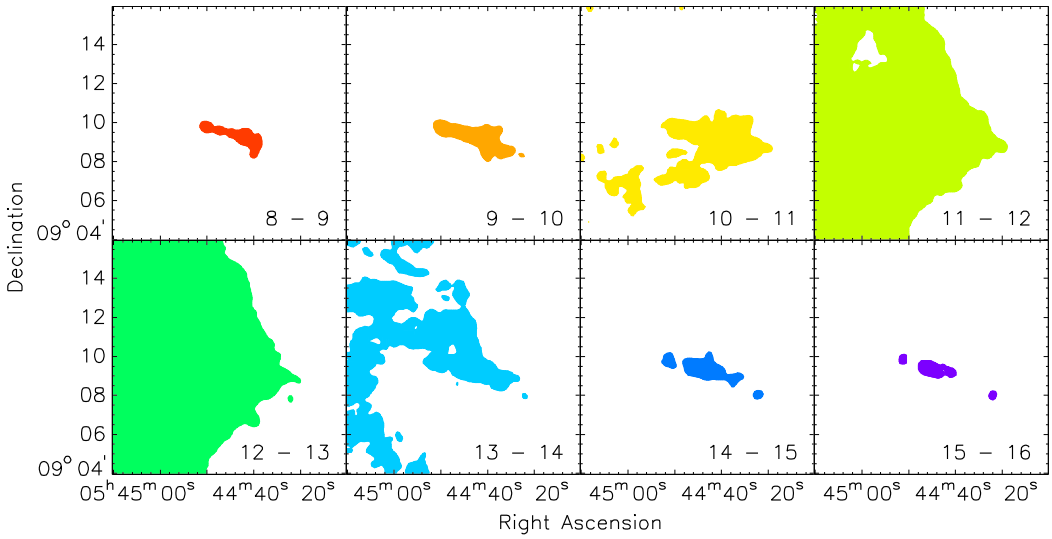

FIGURE 3.9. Maps of integrated intensity in each velocity channel. To illustrate the concept, all pixels with integrated emission greater than 1 K km s^{-1} in the channel are coloured (i.e. a single contour is drawn at 1 K km s^{-1}). The actual channel maps show multiple integrated intensity contours for each channel (e.g. Fig 5.5).

However, for B35A the channel width was additionally increased to 1 km s^{-1} and covered 7 km s^{-1} to explore the higher velocity gas in the molecular outflow.

3.2.2 CLOUD PHYSICAL PROPERTIES

An isotopologue is optically thin where the ratio of its peak intensity to that of a second isotopologue nears the accepted relative abundance ratio (i.e. the entire column of both isotopologues is detected). The ^{12}CO/^{13}CO abundance ratio is 77 (Wilson & Rood (1994)) but the peak intensity ratio is less than 15 for both transitions in every line of sight observed in B35A. The ^{12}CO emission is therefore optically thick across the entire cloud, which means the excitation temperatures could be determined using,

$$T_{\rm ex}(^{12}{\rm CO}) = \frac{T_0}{\ln[1 + T_0/(T_{\rm max} + const)]} \ {\rm K}, \tag{3.2}$$

where T_0 (= hν/k$_{\rm B}$) is 16.6 or 11.1 K (J = 3 $\rightarrow$ 2 and 2 $\rightarrow$ 1, respectively), $T_{\rm max}$ is the ^{12}CO peak main beam temperature and *const* (= T_0/(e$^{T_0/T_{\rm bg}}$-1)) is 0.038 or 0.840 K, where $T_{\rm bg}$ = 2.73 K.

The Boltzmann relationship between the energy level populations was assumed to de-

rive the ^{13}CO excitation temperature,

$$T_{\rm ex}(^{13}{\rm CO}) = \frac{E_2 - E_3}{\ln(R\, g_2/g_3)} \ {\rm K}, \tag{3.3}$$

where the energy levels, E_2 and E_3 are 15.9 and 31.7 K, g_2 and g_3 are the statistical weights, and R is the ratio of the ^{13}CO integrated intensities (J = 3 $\rightarrow$ 2 / J = 2 $\rightarrow$ 1).

The ^{13}CO optical depth was then found using,

$$\tau(^{13}{\rm CO}) = -\ln\left[1 - \frac{T_{\rm max}/T_0}{({\rm e}^{T_0/T_{\rm ex}(^{13}{\rm CO})} - 1)^{-1} - ({\rm e}^{T_0/T_{\rm bg}} - 1)^{-1}}\right], \tag{3.4}$$

where $T_{\rm max}$ is the ^{13}CO (J = 2 $\rightarrow$ 1) peak main beam temperature and T_0 = 10.9 K (^{13}CO J = 2 $\rightarrow$ 1).

Using equations 3.3 and 3.4, the ^{13}CO column density was derived using,

$$N(^{13}{\rm CO}) = \frac{3{\rm k_B}}{8\pi^3 {\rm B}_{13}\mu_{13}^2} \frac{{\rm e}^{{\rm hB}_{13}J(J+1)/{\rm k_B}T_{\rm ex}(^{13}{\rm CO})}}{J+1} \frac{\tau(^{13}{\rm CO})}{1-{\rm e}^{-\tau(^{13}{\rm CO})}} \frac{\int T_{\rm mb} dv}{1-{\rm e}^{-T_0/T_{\rm ex}(^{13}{\rm CO})}} \ {\rm cm}^{-2}. \tag{3.5}$$

The main beam temperature ($T_{\rm mb}$) was integrated over the full width of the line (8 to 15 km s^{-1} for B35A) and T_0 = 10.9 K (^{13}CO J = 2 $\rightarrow$ 1). The rotation constant (B_{13}) and dipole moment (μ_{13}) are 55.101 GHz (Klapper et al., 2000) and 0.11046 D (Goorvitch, 1994), respectively. Similar equations were used by Pineda et al. (2008) for the J = 1 $\rightarrow$ 0 transition.

Assuming a ^{12}CO/^{13}CO abundance ratio of 77 allowed a simple conversion to ^{12}CO optical depth and column density. The H_2/^{12}CO abundance ratio of 10^4 was then used to determine the H_2 column density. These are rough estimates, however, as these ratios are known to vary between clouds and also between regions within clouds (e.g. Pineda et al. (2008), Bolatto et al. (2013), Sofue & Kataoka (2016)).

3.2.3 MAP RESOLUTION

The maps were convolved to a spatial resolution of 15.3 arcsec (the beamsize of C^{18}O J = 3 $\rightarrow$ 2) and smoothed to 40 arcsec to produce clearer maps. The pixel size remains the same (7.3 arcsec), as the data were smoothed across the pixels. Noise levels (1σ) for the 15.3 arcsec resolution maps of B35A are 1.34, 0.99 and 1.02 K for ^{12}CO,

^{13}CO and C^{18}O ($J = 3 \rightarrow 2$), respectively; and similarly 1.62, 0.83 and 0.72 K for the $J = 2 \rightarrow 1$ transitions.

3.2.4 BARNARD 35A

Further extensive analysis was carried out on the observations of B35A to determine the effects of the bright-rim and embedded YSO on the morphology, kinematics and temperature CO gas. This is covered in depth in Chapters 4 and 5.

3.3 ANALYSIS SOFTWARE FOR CO OBSERVATIONS

The reduced observational data from all three telescopes are formatted as 3-dimensional FITS cubes (RA, Dec, spectrum) with details of the observation (target name, location, resolution, projection etc.) recorded in the FITS header. A suite of data analysis software was developed by the author to determine the physical properties of the clouds from the observed spectra contained within the FITS cubes. It is intended for use by the gas-solid mapping project team, and also the wider community, for analysis of CO mapping data.

3.3.1 SYSTEM REQUIREMENTS

At the start of this PhD, the author was familiar with the Fortran 90 programming language. However, it was found that Interactive Data Language (IDL) has a comprehensive astronomy code library and is more user friendly. The author therefore learned this language and used it to write the CO map analysis software. It was written originally using IDL 6.3 and subsequently modified to work with GNU Data Language (GDL) 0.9.6, a free and open-source IDL compiler, which allows the analysis to be performed without an IDL license. The software makes use of the 'IDL Astronomy User's Library', henceforth 'AUL', which is a service of the Astrophysics Science Division at NASA's Goddard Space Flight Center (Landsman, 1993). It is available for download from 'idlastro.gsfc.nasa.gov'. The image plotting routines make use of the 'Coyote Graphics Library' (Fanning, 2003), available on David Fanning's website 'idlcoyote.com'.

3.3.2 COROLINE SOFTWARE

The IDL analysis software written in the course of this PhD is called COROLINE, reflecting its use of **CO ro**tation **line** observations. The structure of the software is presented in Fig. 3.10.

Each FITS file is read into COROLINE via an 'input card' which also specifies the various unique parameters necessary for the analysis of that file, such as the telescope beam efficiency and the velocity of the emission line with respect to the local standard of rest. A routine called 'analyse_FITS' carries out the spectral analysis, calculating the integrated intensity, velocity and linewidth of the emission for each of the $\sim$15,000 pixels which comprise a map, as described in Section 3.2.1. 'analyse_FITS' is called by procedure 'analyse_all_FITS' to perform the spectral analysis on every available FITS file. Intermediate data files containing maps of the spectral parameters are produced for import into other COROLINE routines. These '.xdr' files are read in to the plotting routines, named for the plots they produce (e.g. 'plot_channel_maps', 'plot_linewidth'). Each plot uses the FITS header file to set the map coordinates, the noise file to exclude emission in pixels with excessive noise, and the file with the spectral parameter data. The maps are output as postscript files. The 5σ detection of the cloud edge is located and mapped using the 'cloud outline' routine.

Where observations are available for multiple isotopologues and transitions in the same cloud, the maps are aligned and the overlapping region is extracted using the 'HASTROM' and 'HEXTRACT' programs from the AUL. However, these programs only work for 2-dimensional data so this step is carried out following the spectral analysis. Where sufficient data are available, the physical properties of the cloud are determined using the equations presented in Section 3.2.2. These parameters are also saved as '.xdr' files for import into other routines. Maps are made of each physical parameter and saved as postscript files.

The COROLINE software is used as follows:

The relevant parts of the pipeline are compiled using the '.r' command,

.r cloud_isotopologue_transition.pro *(for all observations available for the cloud)*
.r analyse_FITS_cube.pro
.r analyse_all_FITS_cubes.pro

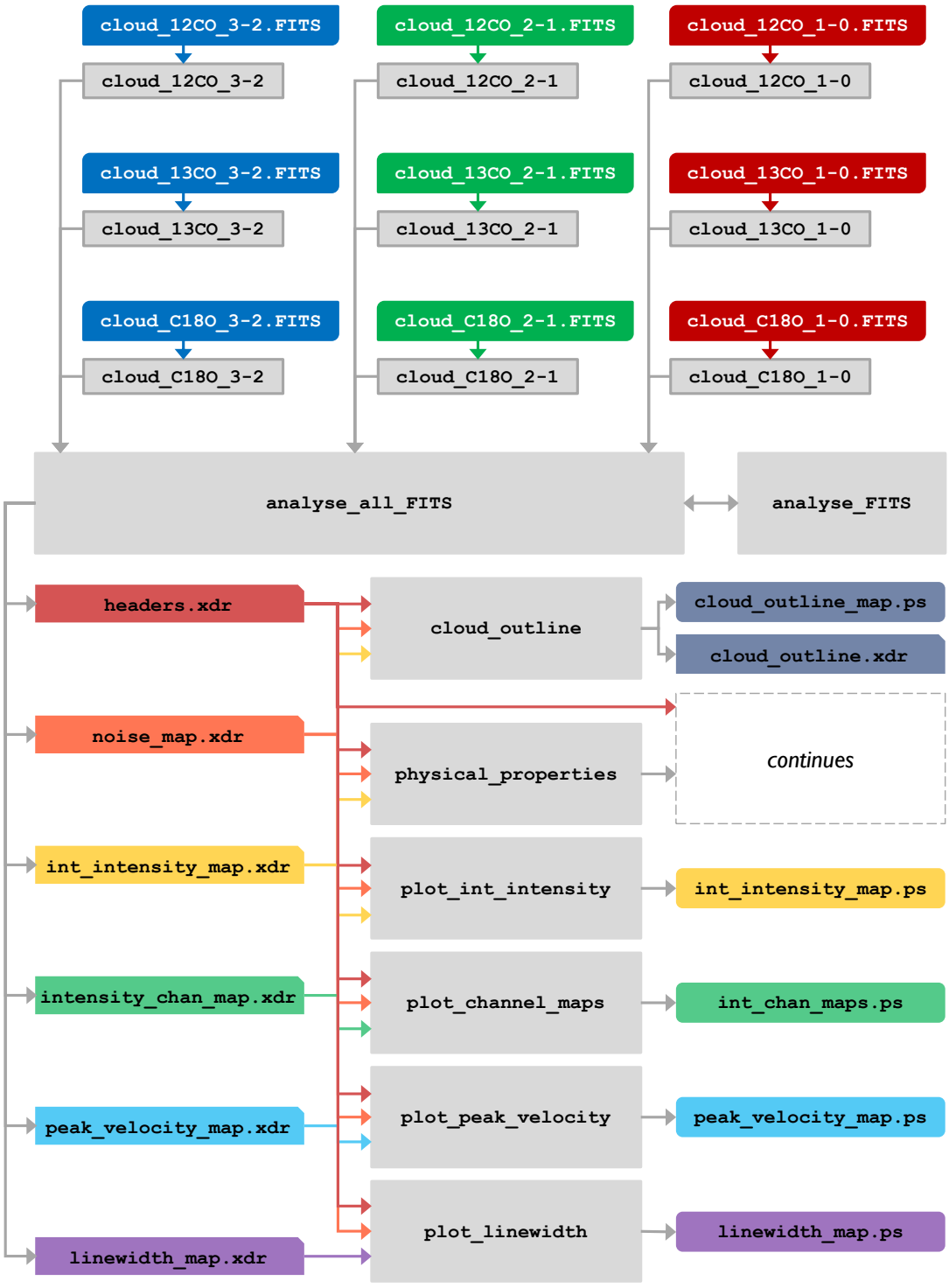

FIGURE 3.10. The structure of the COROLINE software, written for analysing the CO observation data.

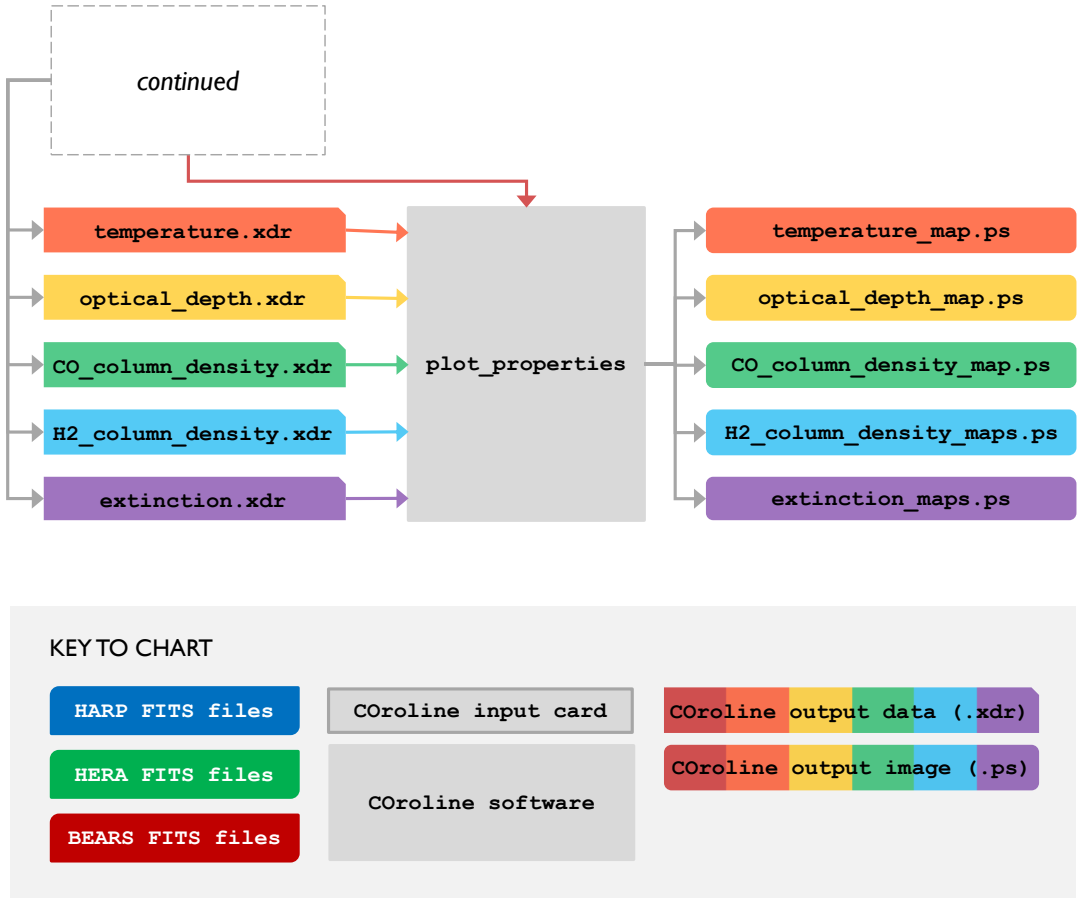

FIGURE 3.10 CONTINUED. The structure of the COROLINE software, written for analysing the CO observation data.

The analysis is then run,

analyse_all_FITS_cubes

The desired maps are output by compiling and running the relevant plotting routines, e.g.

.r plot_channel_maps.pro
plot_channel_maps

If observations exist of enough isotopologues and transitions, the physical properties of the cloud can be determined.

.r physical_properties.pro
physical_properties

Maps of the physical properties can also be plotted,

.r plot_properties.pro
plot_properties

The COROLINE software was used to analyse the CO observations of B35A. It is available to the gas-solid mapping team and will be used for similar analysis of the remaining gas-phase data.

3.4 SUMMARY

Telescope-specific software was used by the author during the observing runs to reduce the data, converting it into 3-dimensional FITS cubes. The quality of the data was monitored and the observing strategy was modified when necessary.

The 'COROLINE' software suite, written by the author in the course of this PhD, extracts the observation data from a FITS cube and performs the necessary analysis to produce maps of the cloud properties including CO column density, H_2 column density, gas velocity and excitation temperature. It is a useful resource for analysing the molecular clouds observed for the gas-solid mapping project and can also be used by others for analysis of similar CO observations.

REFERENCES

Bolatto A. D., Wolfire M., Leroy A. K., 2013, ARAA, 51, 207 70

Currie M. J., Berry D. S., , 2014, KAPPA: Kernel Applications Package, Astrophysics Source Code Library 62

Draper P. W., Gray N., Berry D. S., Taylor M., , 2014, GAIA: Graphical Astronomy and Image Analysis Tool, Astrophysics Source Code Library 62

Fanning D. J., 2003, IDL programming techniques – 2nd ed. 71

Gildas Team, 2013, GILDAS: Grenoble Image and Line Data Analysis Software, Astrophysics Source Code Library 64

Goorvitch D., 1994, ApJS, 95, 535 70

Hanisch R. J., Farris A., Greisen E. W., Pence W. D., Schlesinger B. M., Teuben P. J., Thompson R. W., Warnock III A., 2001, A&A, 376, 359 62

Ikeda M., Nishiyama K., Ohishi M., Tatematsu K., 2001, in Harnden Jr. F. R., Primini F. A., Payne H. E., eds, Astronomical Data Analysis Software and Systems X Vol. 238 of Astronomical Society of the Pacific Conference Series, Development of Radio Astronomical Data Reduction Software NEWSTAR. p. 522 65

Jenness T., Chapin E. L., Berry D. S., Gibb A. G., Tilanus R. P. J., Balfour J., Tilanus V., Currie M. J., , 2013, SMURF: SubMillimeter User Reduction Facility, Astrophysics Source Code Library 62

Klapper G., Lewen F., Gendriesch R., Belov S. P., Winnewisser G., 2000, Journal of Molecular Spectroscopy, 201, 124 70

Landsman W. B., 1993, in Astronomical Data Analysis Software and Systems II Vol. 52 of Astronomical Society of the Pacific Conference Series, The IDL Astronomy User's Library. p. 246 71

Pineda J. E., Caselli P., Goodman A. A., 2008, ApJ, 679, 481 70

Rankin S., Lawden M., Bly M., 2003, Starlink User Note, 1 62

Sofue Y., Kataoka J., 2016, Publ. Astron. Soc. Japan, 68, L8 70

Wilson T. L., Rood R., 1994, ARAA, 32, 191 69

CHAPTER 4

EVIDENCE FOR PHOTOELECTRIC HEATING IN BARNARD 35A

SYNOPSIS

This chapter presents observational evidence for a correlation between the intensity of PAH emission near 8 μm and gas excitation temperature across a 1.1 × 1.6 pc region of B35A. This relationship is consistent with photoelectric heating, where the absorption of UV photons by PAHs results in either infrared emission or the ejection of energetic photoelectrons that heat the gas.

By comparing B35A with similar clouds (the Orion Bar and Horsehead Nebula), the offset between the positions of maximum PAH emission (PAH_{max}) and maximum ^{12}CO emission ($^{12}CO_{max}$) within the PDR are shown to depend on the UV flux enhancement, G_0. In clouds where G_0 is moderate to high ($\gtrsim$60), ^{12}CO is photodissociated at the cloud edge and an offset is observed. For B35A, however, G_0 is very low ($\sim$20), which indicates that PAH_{max} and $^{12}CO_{max}$ coincide in this PDR. As the ^{12}CO is optically thick, the positions of $^{12}CO_{max}$ and T_{max} (excitation temperature maxima) are identical. It then follows that PAH_{max} and T_{max} also coincide, validating the correlation.

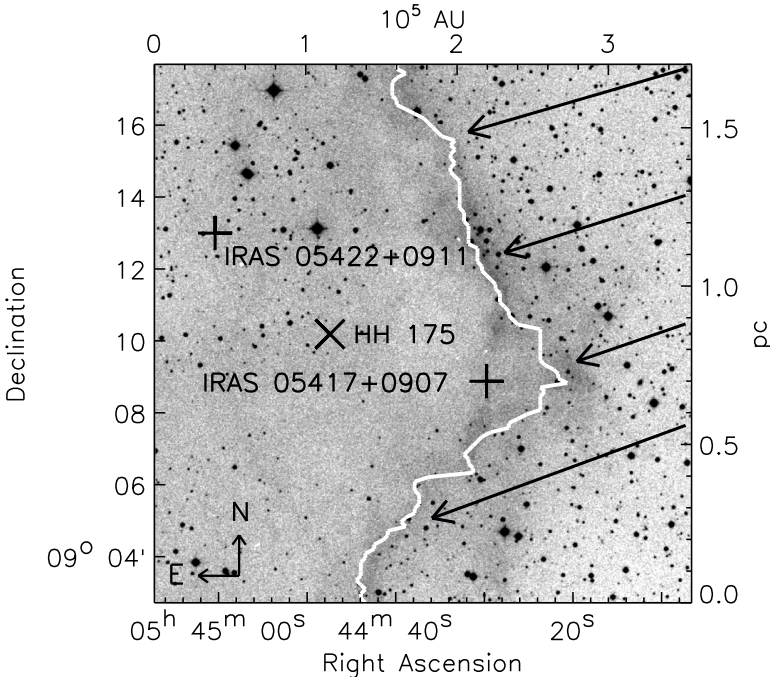

FIGURE 4.1. Objects of interest in the observed 14.6 × 14.6 arcmin region of B35A plotted on a Digitized Sky Survey image. A Herbig–Haro object and two IRAS sources are shown. IRAS 05417+0907 is a young stellar object with outflows in the northeast-southwest direction. Arrows indicate the direction of the wind from O8 III star λ Ori and the white line shows the western edge of the 5σ detection of ^{12}CO $J = 2 \rightarrow 1$ emission.

4.1 INTRODUCTION

4.1.1 BARNARD 35A

B35A is a type-A bright-rimmed molecular cloud found on the edge of the H II region formed by the λ Orionis (λ Ori) OB association. Objects of interest within the cloud are listed in Table 4.1 and plotted in Fig. 4.1 on a Digitized Sky Survey image, shown in negative. The dark region at the furthest western extent of the cloud is the bright rim, caused by scattered light from the nearby OB association. A dense ridge is indicated by the lack of stars immediately to the east of the bright rim, where the light from background stars cannot penetrate. The northern section of the dense ridge lies almost perpendicular to the direction of the wind from λ Ori, shown by arrows. UV photons from λ Ori are incident only on the western edge of the cloud, resulting in a PDR. This orientation makes it possible to investigate the relationship between PAH emission and gas excitation temperature across all environments in the cloud, from the PDR to the shielded interior, to test for photoelectric heating. Embedded Class I YSO

TABLE 4.1. Notable objects in the observed region of B35A

Object	RA (J2000)	Dec (J2000)	Description
λ Ori	05 35 08.3	+09 56 03	O8 III star
IRAS 05417+0907$^{\diamond}$	05 44 29.8	+09 08 54	YSO†
IRAS 05422+0911	05 45 00.5	+09 13 00	IR source
HH 175	05 44 47.5	+09 10 12	HH Object
Spitzer candidate YSOs‡:			
YSOc_red	05 44 29.3	+09 08 56.8	YSO*
YSOc	05 44 30.0	+09 08 57.3	YSO**
YSOc_star+dust(IR2)	05 44 30.9	+09 08 26.2	YSO*
YSOc_star+dust(IR2)	05 44 31.6	+09 08 57.9	YSO*

$^{\diamond}$ Connelley et al. (2008) detected a close binary companion (484 AU)
† see Table 4.2 ‡ defined by the c2d catalogue
* uncertain assignment ** IRAS 05417+0907

TABLE 4.2. Physical parameters of the observed region of B35A

Parameter	Value	Notes
Distances:		
B35A	400 ± 40 pc	Murdin & Penston (1977)
λ Ori	400 ± 40 pc	Murdin & Penston (1977)
λ Ori to B35A bright rim	17.2 ± 1.7 pc	d = 400 pc
Observed area:		
Angular	14.6×14.6 arcmin	
Actual	1.7×1.7 pc	d = 400 pc
YSO (IRAS 05417+0907):		
Class	I	Sugitani et al. (1991)
Luminosity	6 $L_{\odot}$	Morgan et al. (2008)
Spectral type	F0	de Jager & Nieuwenhuijzen (1987)
Mass	1.15 $M_{\odot}$	Morgan et al. (2008)

IRAS 05417+0907 (hereafter, the YSO) lies within the densest region of the cloud and is thought to be the result of triggered star formation, due to the age of the H II region (5.9 x 10^6 yr) and the implosion time-scale ($< 10^4$ yr) (Qin & Wu, 2003). The YSO is known to have an outflow (Myers et al. (1988), CO $J = 1 \rightarrow 0$), which extends in the northeast-southwest direction and is aligned with Herbig–Haro object HH 175. IRAS 05422+0911 and three further objects, found near the YSO by the *Spitzer* 'From Molecular Cores to Planet Forming Disks' (c2d) legacy survey (Evans et al., 2003), remain unclassified.

It is generally accepted that B35A and the OB association containing O8 III star

λ Ori lie at a distance of 400 ($\pm$40) pc (Murdin & Penston (1977)), separated by 17.2 $\pm$ 1.7 pc. However, determining the distance to a cloud is not straightforward. Since 1977 several distances have been quoted for B35A. Murdin & Penston (1977) plotted a Hertzsprung-Russell diagram of K-magnitude vs spectral type using a sample of stars within half a degree of λ Ori. They fit the zero-age main sequence and derived a distance modulus for the association corresponding to 400$\pm$40 pc, which is similar to the accepted distances for other regions of Orion. Armandroff & Herbst (1981) used star counts to determine the foreground star density for B35A and derived the distance using an empirical relation (d=320N$^{0.57}$ (Herbst & Sawyer, 1981)). This method yields a distance of 530$\pm$150 pc and the large uncertainty means that this value agrees with Murdin & Penston (1977). The star counting method, however, is only reliable for clouds with $A_V \gtrsim 7$ mag over the surveyed area. The observations presented in this chapter show that the extent of extinction $\gtrsim$7 mag is much less than the 32.6 arcmin^2 surveyed by Armandroff & Herbst (1981). This may mean that some background stars were counted leading to a greater distance estimate. It is therefore reasonable to assume that the best estimate is 400$\pm$40 pc.

B35A was observed for the gas-solid mapping project described in Section 1.5. This chapter presents the first large scale maps of B35A (14.6 $\times$ 14.6 arcmin, 1.7 $\times$1.7 pc) in three isotopologues and two transitions of CO. The maps are centred on $05^h44^m37.0^s$ $+09^\circ10'13.0''$(J2000) and include the bright rim and centre of the cloud. A range of environments within the cloud was investigated by observing multiple CO isotopologues. ^{12}CO emission traces the optically thick cloud surface. ^{13}CO is less abundant and emission from deeper in the cloud is observable. The least abundant of the three isotopologues, C^{18}O, probes even deeper into some of the densest regions of the cloud. Full details of the observations are presented in Chapter 2 and the initial analysis of the data is described in Chapter 3. The effects of the YSO's precessing outflow on the CO gas morphology and kinematics are discussed in detail in Chapter 5; this chapter explores the gas temperature and density structure of the cloud and presents the first observational evidence for photoelectric heating.

4.1.2 PHOTOELECTRIC HEATING

It is widely accepted that gas temperature and PAH emission are linked in PDRs as PAHs are the most efficient species for ejecting photoelectrons that heat the gas (D'Hendecourt & Leger (1987); Lepp & Dalgarno (1988); Verstraete et al. (1990);

TABLE 4.3. Observed CO emission lines

Isotopologue & J Transition	Telescope & Receiver	Frequency (GHz)	Beamsize (arcsec)
^{12}CO $3 \rightarrow 2$	JCMT HARP	345.8	14.6
^{13}CO		330.6	15.2
C^{18}O		329.3	15.3
^{12}CO $2 \rightarrow 1$	IRAM HERA	230.5	10.9
^{13}CO		220.4	11.4
C^{18}O		219.6	11.5

Bakes & Tielens (1994); Weingartner & Draine (2001)). In this chapter CO observations are combined with IRAC 8 μm maps to investigate a relationship between CO gas excitation temperature and polyaromatic hydrocarbon (PAH) emission. A correlation would provide the first observational evidence for PAH photoelectric heating, an assumption implemented in all PDR codes (Röllig et al., 2007). This chapter shows a statistically unbiased clear relationship between PAH emission and gas kinetic temperature across a 1.1 × 1.6 pc region of B35A.

Previous studies have found an offset between the positions of maximum of PAH and maximum ^{12}CO emission in PDRs (Tielens et al. (1993), (Habart et al., 2005)). This offset is investigated on a much larger scale and is found to depend on the enhanced UV flux, G_0. In PDRs where G_0 is moderate to high ($\gtrsim$60), the offset is large (Tielens et al. (1993); Habart et al. (2005)). However, as G_0 is only $\sim$20 in B35A (Wolfire et al., 1989) the offset is found to be negligible, validating the correlation.

The CO observations map a 14.6 × 14.6 arcmin (1.7 × 1.7 pc) region centred on $05^{h}44^{m}37.0^{s}$ $+09^{\circ}10'13.0''$(J2000) including the bright rim and centre of the cloud. The observed lines are summarised in Table 4.3.

4.2 GAS TEMPERATURE AND DENSITY STRUCTURE

Fig. 4.2 shows the integrated intensities of the three CO isotopologues between 8 and 15 km s^{-1} with a resolution of 40 arcsec. In general, the ^{12}CO emission has the greatest intensity and extends from a dense ridge on the western side towards a more diffuse region on the east. The intensity is enhanced along the outflow, between the YSO and the HH object, where the gas is entrained by the jet. The ^{13}CO emission closely matches the edge of the cloud and the dense ridge shown in ^{12}CO. The dense

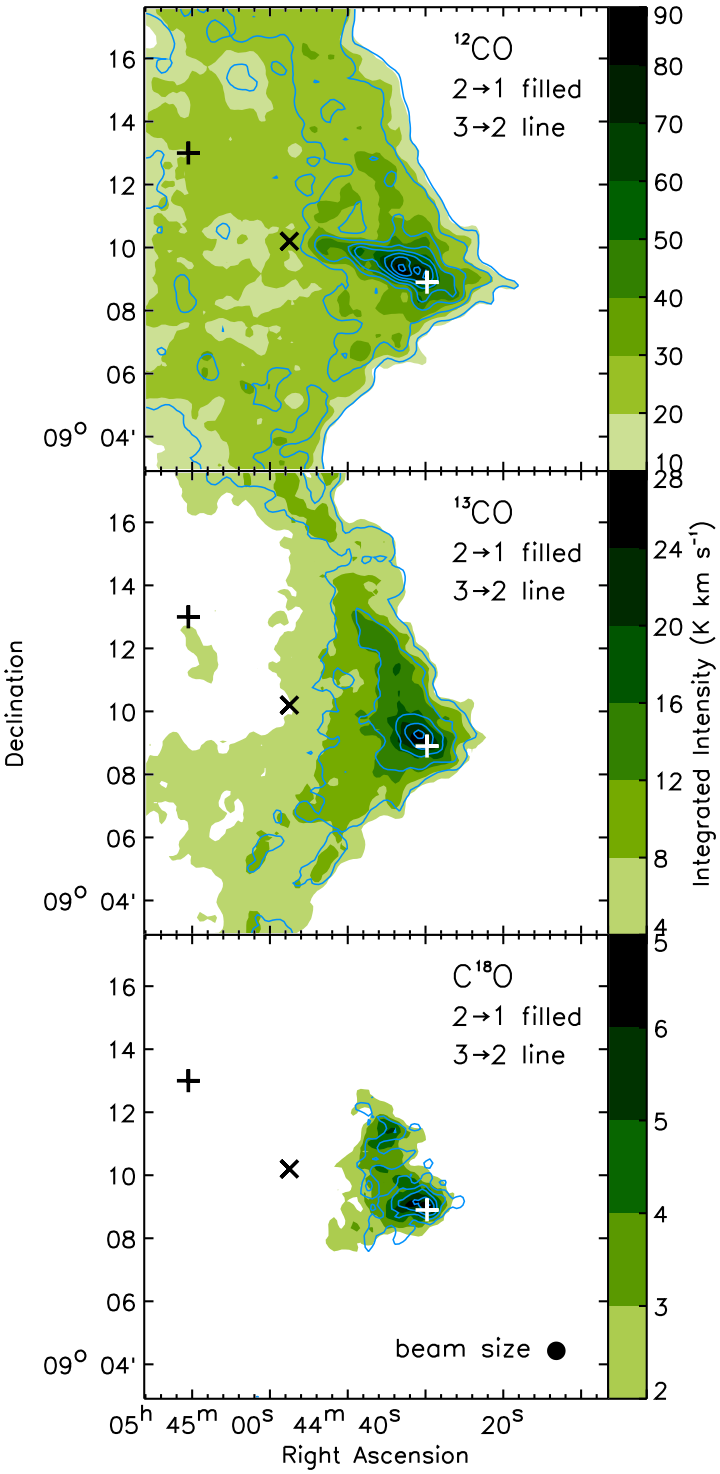

FIGURE 4.2. Integrated intensities of the ^{12}CO, ^{13}CO and C^{18}O emission. Filled contours show the $J = 2 \rightarrow 1$ transition overlaid with line contours showing the $J = 3 \rightarrow 2$ transition. For each isotopologue the $J = 3 \rightarrow 2$ contour levels are the same as those for the $J = 2 \rightarrow 1$ transition. The ^{12}CO emission has the greatest intensity and extends from a dense ridge on the western side towards a more diffuse region on the east. A dense ridge of ^{13}CO extends from the YSO to the north of the cloud perpendicular to the direction of the stellar wind from λ Ori. The C^{18}O emission is evident only in the very dense region of the cloud near the YSO.

ridge of ^{13}CO extends from the YSO to the north of the cloud; perhaps due to the stellar winds encountering this region perpendicular to the cloud edge, causing greater compression here than to the south (see Fig. 4.1). The C^{18}O emission traces the dense region of the ridge where the YSO is found. It also extends towards the north of the cloud, although not as far as the more abundant ^{13}CO. The integrated intensities of the $J = 3 \rightarrow 2$ transitions, shown in blue, are very similar, both in extent and magnitude, to the $J = 2 \rightarrow 1$ transitions. The optically thick ^{12}CO emission matches very closely, while ^{13}CO and C^{18}O are slightly more extended in the $J = 2 \rightarrow 1$ transition. This is not surprising as the $J = 2 \rightarrow 1$ transition is more easily excited. The clump, evident near the position of the unidentified IRAS source in the ^{13}CO $J = 2 \rightarrow 1$ map, is discussed in Chapter 5.

Peak emission maps are shown in Fig. 4.3 for all observed isotopologues and transitions (^{12}CO, ^{13}CO and C^{18}O; $J = 3 \rightarrow 2$ and $J = 2 \rightarrow 1$) with a 40 arcsec resolution. A steep drop in emission at the western edge of the cloud is clearly evident in horizontal cuts through the maps. This sharp edge is a characteristic of bright-rimmed clouds. The ^{12}CO western edge lies up to 2 arcmin (17 pixels) west of the ^{13}CO edge and its gradient is steeper. This is likely due to self-shielding; the UV photons with energy equal to the photodissociation energy of ^{12}CO are completely absorbed within a narrow layer at the cloud surface ($A_V \sim 0.7$), due to the high abundance of this isotopologue. The ^{13}CO, however, is less abundant and therefore preferentially photodissociated at the western surface of the cloud, resulting in a shallower gradient on the cut maps and smaller western extent. Both ^{12}CO transitions show peaks around the $05^h45^m00^s$ right ascension line. Some of the ^{13}CO cuts also show peaks in this region, where dense clumps are seen in the diffuse eastern side of the cloud. These clumps are discussed in Chapter 5.

The right-hand column of Fig. 4.3 shows the ^{12}CO and ^{13}CO excitation temperatures across the region, calculated using Equations 3.2 and 3.3. For both isotopologues the temperature peaks at 25 – 35 K along the northern section of the western edge, where the incident UV flux is highest. The ^{12}CO map shows a warm western region with temperatures of 20 – 30 K decreasing to 15 K in the east, with the exception of a few warm clumps which are discussed in Chapter 5. The ^{13}CO shows a similar morphology with temperatures of 20 – 35 K along the western edge, decreasing to 10 – 15 K towards the east. The warm clump near the IRAS source is also discussed in Chapter 5. The overall temperature structure of the cloud is consistent with heating from the northwest, the direction of O8 III star λ Orionis. The maps of peak emission,

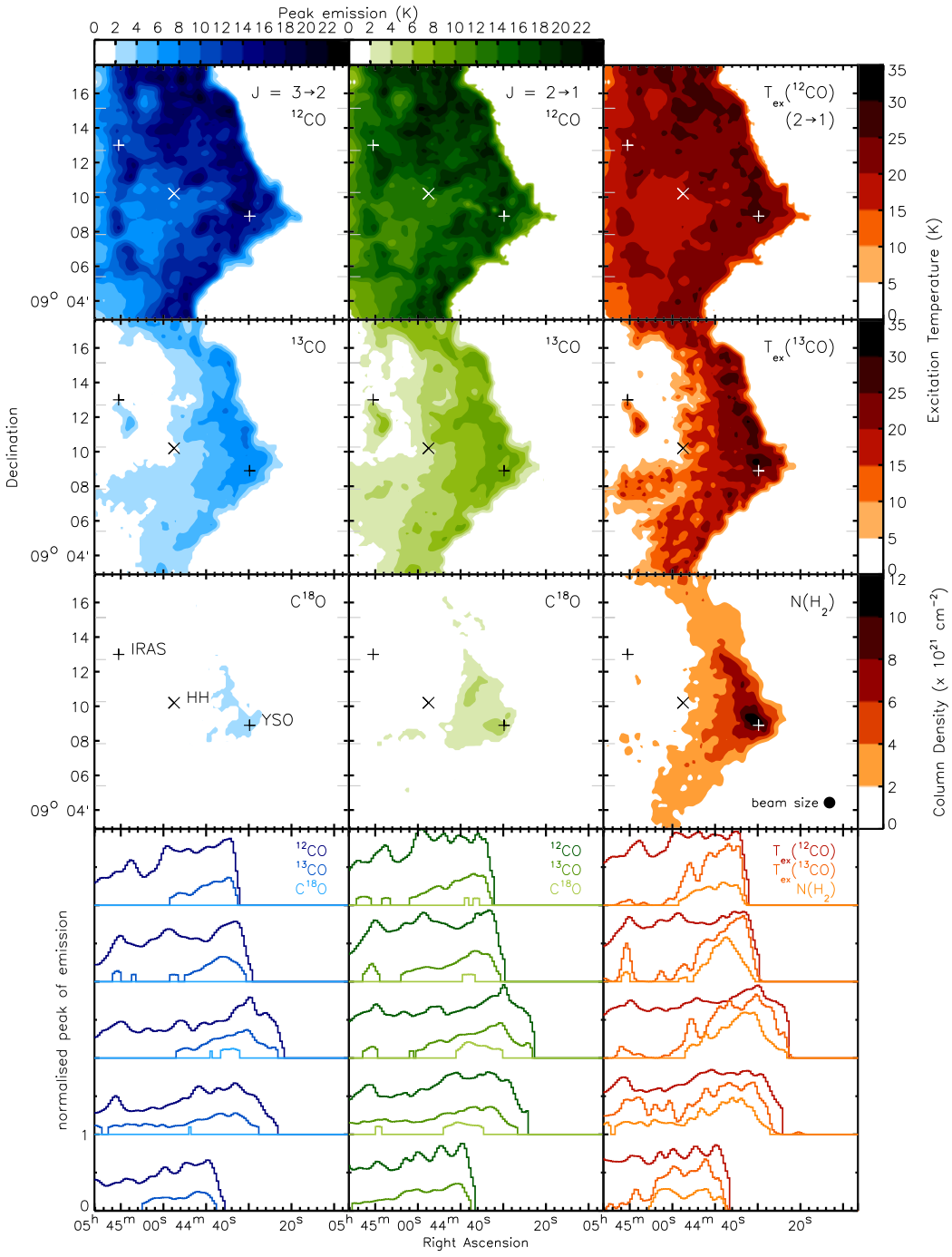

FIGURE 4.3. Peak emission maps for ^{12}CO ^{13}CO and C^{18}O ($J = 3 \rightarrow 2$) and horizontal cuts are shown in the left column. Similar maps and cuts for $J = 2 \rightarrow 1$ are shown in the middle column. The horizontal cuts (positions indicated in grey) have been normalised to the maximum value of the ^{12}CO $J = 2 \rightarrow 1$ peak map, which is 22.67 K. Emission below the detection limit has been removed (2σ for all maps except ^{12}CO $J = 2 \rightarrow 1$, where the 4σ detection was used). The ^{12}CO and ^{13}CO excitation temperature maps and H_2 column density map (divide by 10^4 for ^{12}CO column densities and 1.9×10^{21} for A_V), are shown in the right column. Horizontal cuts have been normalised to the maximum of the corresponding map: $T_{ex}(^{12}\mathrm{CO})_{max} = 28.69$ K, $T_{ex}(^{13}\mathrm{CO})_{max} = 31.93$ K, $N(\mathrm{H_2})_{max} = 1.2 \times 10^{22}$ cm^{-2}.

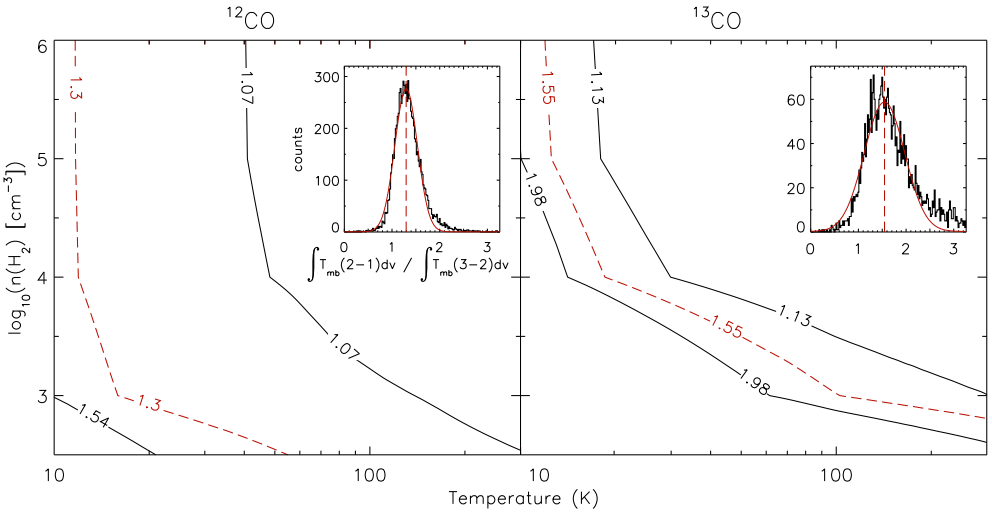

FIGURE 4.4. Radiative transfer analyses using the RADEX code with ^{12}CO and ^{13}CO column densities of 2.1×10^{17} and 2.7×10^{15} cm^{-2}, respectively, have been used to find the cloud density. Inset histograms show the integrated intensity ratio ($J = 2 \rightarrow 1$ / $J = 3 \rightarrow 2$) distribution for the ^{12}CO and ^{13}CO maps. Gaussian fits to the histograms have peak positions at 1.30 and 1.55, respectively. Applying these line ratios to the RADEX output shows that the H_2 density is 10^3 – 10^6 cm^{-3} for temperatures of 10 – 30 K.

and H_2 column density, describe a consistent morphology: a dense ridge with a well defined western edge extends in the north-south direction showing the highest density in the centre ($N(H_2)_{max} = 1.2 \times 10^{22}$ cm^{-2}), extending towards the northern end. The eastern side of the ridge gradually decreases in density towards the furthest extent of the map, with the exception of a few dense clumps. Dolan & Mathieu (2002) suggest that a supernova in the λ Ori OB association around 1 Myr ago may have eroded the inward facing sides of nearby clouds and caused the striking circular morphology of the H II region in which B35A lies (see Fig. 4 in Lee et al. (2005)). Although this could account for the observed dense ridge and sharp edge in B35A (and similar cloud B30), winds from the OB stars or the advancing ionization front would have a similar effect.

A RADEX radiative transfer analysis was carried out, using the ^{12}CO and ^{13}CO observations independently, to confirm the temperature and determine the range of densities in the cloud. RADEX is a one-dimensional radiative transfer code based on the escape probability method (van der Tak et al., 2007). Column densities for ^{12}CO (2.1×10^{17} cm^{-2}) and ^{13}CO (2.7×10^{15} cm^{-2}) were input and the observed integrated intensity ratios ($J = 2 \rightarrow 1$ / $J = 3 \rightarrow 2$) were used to determine the density range for the cloud.

The cloud density was determined by RADEX radiative transfer analyses using the me-

dian ^{12}CO and ^{13}CO column densities (2.1×10^{17} and 2.7×10^{15} cm^{-2}, respectively). Histograms showing the ratio of integrated intensities ($J = 2 \rightarrow 1$ / $J = 3 \rightarrow 2$) in all 14,641 pixels are inset in Fig. 4.4. Gaussian fits show that the distributions are centred on 1.30 and 1.55 with full-width half maxima of 0.47 and 0.85. Applying these line ratios to the RADEX analyses gave H_2 densities of 10^3 – 10^6 cm^{-3} for temperatures of 10 – 30 K, using the ^{12}CO and ^{13}CO data independently.

4.3 EVIDENCE FOR PHOTOELECTRIC HEATING

CO observations are combined with an IRAC 8 μm map and a relationship is found between the gas excitation temperature and PAH emission, adding weight to the hypothesis that PAHs electronically excited by FUV radiation eject photoelectrons which heat the gas.

The excitation temperature map in Fig. 4.5(a), derived from equation 3.2, shows that the cloud temperature is around 25 K along the edge facing the nearby O8 III star λ Ori, decreasing to ∼15 K in the cloud interior. To verify this method the same calculations were performed on an isolated starless cloud (L204C-2, Chapman & Mundy (2009)) yielding temperatures between 10 and 15 K across the whole cloud. This range is more consistent with the expected gas temperature where there are no OB stars in the vicinity (Lai et al., 2003). Park et al. (2004) also find a temperature of ∼15 K for L204C-2 using the $J = 1 \rightarrow 0$ transition of ^{12}CO. Since the heating effect extends along the whole western edge of B35A in the 14.6×14.6 arcmin (1.7×1.7 pc) field of view, it is reasonable to conclude that the PDR also extends over this region. Most of this PDR, and much of the shielded interior, have also been observed by *Spitzer*. Fig. 4.5(b) shows the *Spitzer* IRAC 8 μm flux overlaid with the ^{12}CO gas excitation temperature contours. If photoelectric heating is occurring, the warmest gas (heated by photoelectrons ejected from PAHs) should coincide with the highest 8 μm flux; PAH^+ emission is much stronger than PAH emission at this wavelength. Such a regime is evident in Fig. 4.5(b): regions of high 8 μm flux and high gas excitation temperature coincide at the edge of the cloud where the UV photons from λ Ori are incident; whereas low 8 μm flux and low excitation temperature are found in the shielded cloud interior.

The ^{13}CO excitation temperature map in Fig. 4.5(c), shows a similar structure, with warmer gas towards the western cloud edge. As ^{13}CO traces only the denser (inner) regions of the cloud, the spatial extent of the emission is smaller and the tempera-

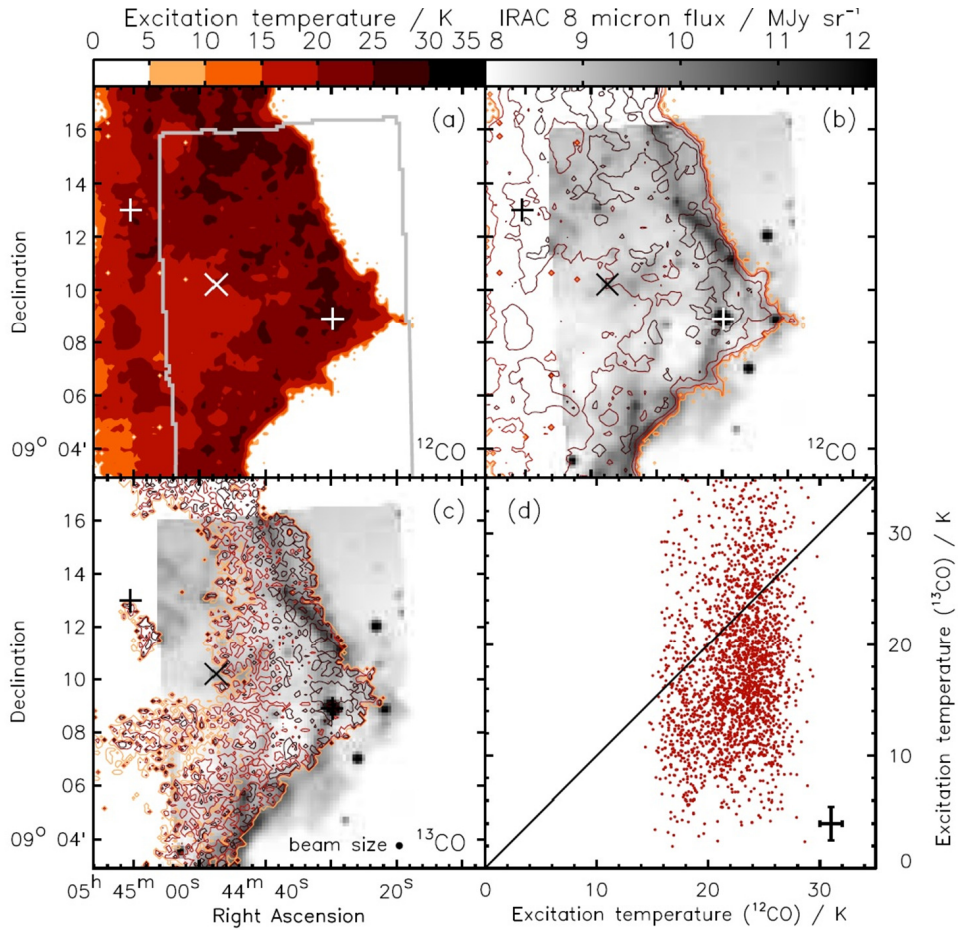

FIGURE 4.5. Maps with 15.3 arcsec resolution. (a) Gas excitation temperature map derived from the ^{12}CO $J = 2 \rightarrow 1$ transition. The region covered by the IRAC 8 μm data is outlined in grey. Objects within the cloud (+ and ×) are as described in Fig. 4.1. The cloud edge has a temperature of 20 – 30 K, which decreases to ∼15 K in the cloud interior. (b) *Spitzer* IRAC 8 μm flux, in greyscale, overlaid with the line-contour excitation temperature map derived from ^{12}CO ($J = 2 \rightarrow 1$). Two regimes are evident: high 8 μm flux and high excitation temperature coincide at the edge of the cloud where the UV photons from nearby O8 III star λ Ori are incident; whereas low 8 μm flux and low excitation temperature are found in the shielded cloud interior. (c) Greyscale as in (b) overlaid with the line-contour excitation temperature map derived from both transitions of ^{13}CO. This map also shows high temperatures (around 30 K) at the cloud edge, decreasing to 10 – 15 K towards the interior. ^{13}CO is not detected in the less dense eastern region of the cloud. (d) Scatter plot between the gas excitation temperatures derived from ^{12}CO ($J = 2 \rightarrow 1$) and ^{13}CO showing that the ^{13}CO is subthermally excited.

ture cannot be determined across the whole cloud. Furthermore, where the ^{12}CO and ^{13}CO temperature maps overlap, the ^{13}CO temperature is systematically lower (see Fig. 4.5(d)). This suggests that the ^{13}CO is subthermally excited, so although the ^{12}CO excitation temperature is equivalent to the kinetic temperature of the gas, this is not the

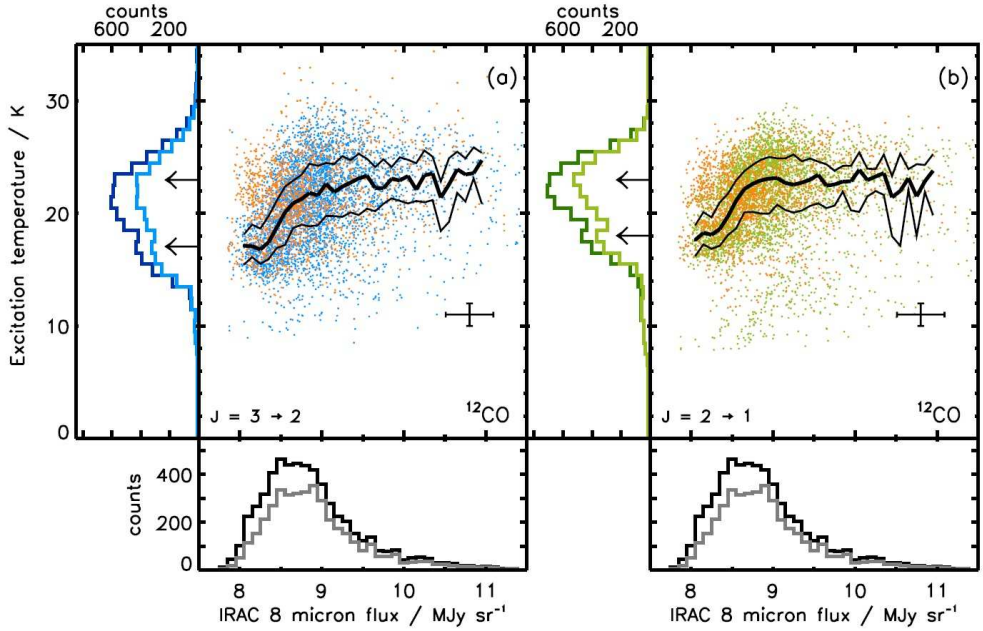

FIGURE 4.6. Scatter plot of the 8 μm flux and gas excitation temperature derived from the ^{12}CO (a) $J = 3 \rightarrow 2$ and (b) $J = 2 \rightarrow 1$ transitions to demonstrate that PAH emission and gas temperature are related over a 1.1 × 1.6 pc region, from the PDR to the shielded cloud interior. The blue and green points are from the quiescent region of the cloud and the orange points show the region affected by the YSO. The median of the quiescent distribution is overplotted as a thick black line and the two thin black lines are the upper and lower quartiles (25 per cent). Excitation temperature histograms are plotted to the left (the darker shade includes the YSO points, the lighter shade excludes them), and the IRAC flux histogram is plotted below (black includes the YSO points, grey excludes them). It is clear that the YSO has little effect on the correlation.

case for ^{13}CO.

The qualitative alignment between the temperature and 8 μm maps prompted further investigation of the relationship. The pixel to pixel scatter plot between ^{12}CO excitation temperature and IRAC 8 μm flux is shown in Fig. 4.6(a&b) with the median (thick black line) and upper and lower quartiles (the two thin black lines that enclose 50 per cent of the data points). The total number of pixels used in each correlation is 5736, of which 1678 (plotted in orange) are associated with turbulent gas caused by the YSO (IRAS 05417+0907). They are scattered across the plot, so although the YSO may have some effect on the heating of the cloud it is not likely to bias this analysis. However, to avoid any doubt, the YSO pixels are removed from all further analysis. The shape of the median curve suggests that either a non-linear correlation or two linear correlations with a turning point at ∼8.8 μm exist between the gas temperature and

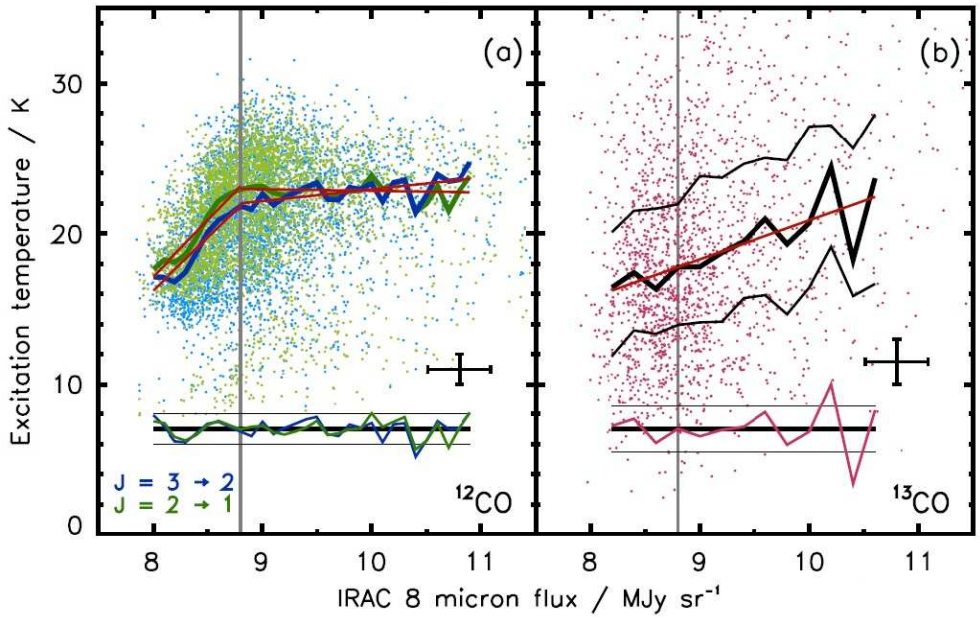

FIGURE 4.7. Scatter plot of the 8 μm flux and gas excitation temperature derived from the ^{12}CO $J = 3 \rightarrow 2$ (blue), $J = 2 \rightarrow 1$ (green) and ^{13}CO (pink) transitions to demonstrate that PAH emission and gas temperature are related over a 1.1 × 1.6 pc region, from the PDR to the shielded cloud interior. (a) Fits to the median lines are shown in red (see text and Table 4.4 for details) and the residuals are plotted below with the black lines indicating the ±1 K 3σ error in the temperature. The ^{12}CO data are divided into two IRAC 8 μm flux regimes for fitting: 'low' 7.9 to 8.8 and 'high' 8.8 to 10.9 MJy sr^{-1}. There are fewer points in the scatter plot derived from the quiescent ^{13}CO emission (b) as it has a smaller spatial extent. The median and upper and lower quartiles, overplotted as thick and thin black lines respectively, show a single linear correlation. The residuals are plotted below with the black lines indicating the ±1.5 K 3σ error in the temperature.

PAH flux. The two linear correlation hypothesis is preferable, since both the $J = 3 \rightarrow 2$ and $J = 2 \rightarrow 1$ data suggest that the cloud gas temperature distribution (binned to 1 K) is bimodal (see histograms to the left of each scatter plot in Fig. 4.6(a&b)). The two gas populations evident in both transitions of the ^{12}CO data, peaking at 23 K and 17 – 18 K, agree within the 3σ error of the data (i.e. 1 K). The temperature distributions of the data from the whole cloud (darker coloured histograms in Fig. 4.6(a&b)) show a very similar shape to the quiescent cloud temperature distributions (lighter coloured histograms). This is further evidence that the YSO does not affect the correlation. A histogram of the 8 μm flux from the quiescent cloud is repeated below the scatter plots in Fig. 4.6(a&b), binned to 0.1 MJy sr^{-1}, showing a single-peak log-normal distribution (in grey). This shape is also unaffected by the inclusion of the points associated with the YSO (shown in black). Given that the embedded Class I YSO has a luminosity

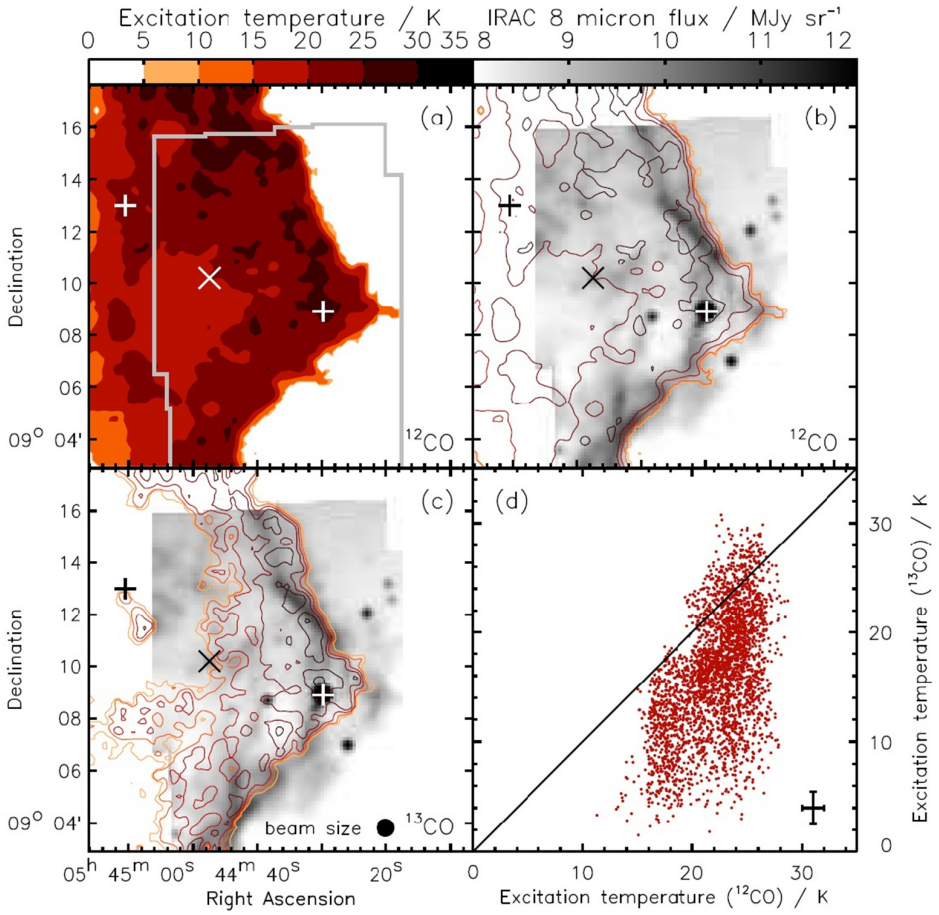

FIGURE 4.8. 40 arcsec resolution version of Fig 4.5. (a) Gas excitation temperature map derived from the ^{12}CO $J = 2 \rightarrow 1$ transition. The region covered by the IRAC 8 μm data is outlined in grey. Objects within the cloud (+ and ×) are as described in Fig. 4.1. The cloud edge has a temperature of 20 – 30 K, which decreases to ∼15 K in the cloud interior. (b) *Spitzer* IRAC 8 μm flux, in greyscale, overlaid with the line-contour excitation temperature map derived from ^{12}CO ($J = 2 \rightarrow 1$). Two regimes are evident: high 8 μm flux and high excitation temperature coincide at the edge of the cloud where the UV photons from nearby O8 III star λ Ori are incident; whereas low 8 μm flux and low excitation temperature are found in the shielded cloud interior. (c) Greyscale as in (b) overlaid with the line-contour excitation temperature map derived from both transitions of ^{13}CO. This map also shows high temperatures (around 30 K) at the cloud edge, decreasing to 10 – 15 K towards the interior. ^{13}CO is not detected in the less dense eastern region of the cloud. (d) Scatter plot between the gas excitation temperatures derived from ^{12}CO ($J = 2 \rightarrow 1$) and ^{13}CO showing that the ^{13}CO is subthermally excited.

of only 6 $L_{\odot}$ (Morgan et al., 2008), the number of UV photons from the YSO heating the cloud beyond its envelope is negligible.

The correlations are replotted in Fig. 4.7(a), with all YSO pixels omitted. Linear fits

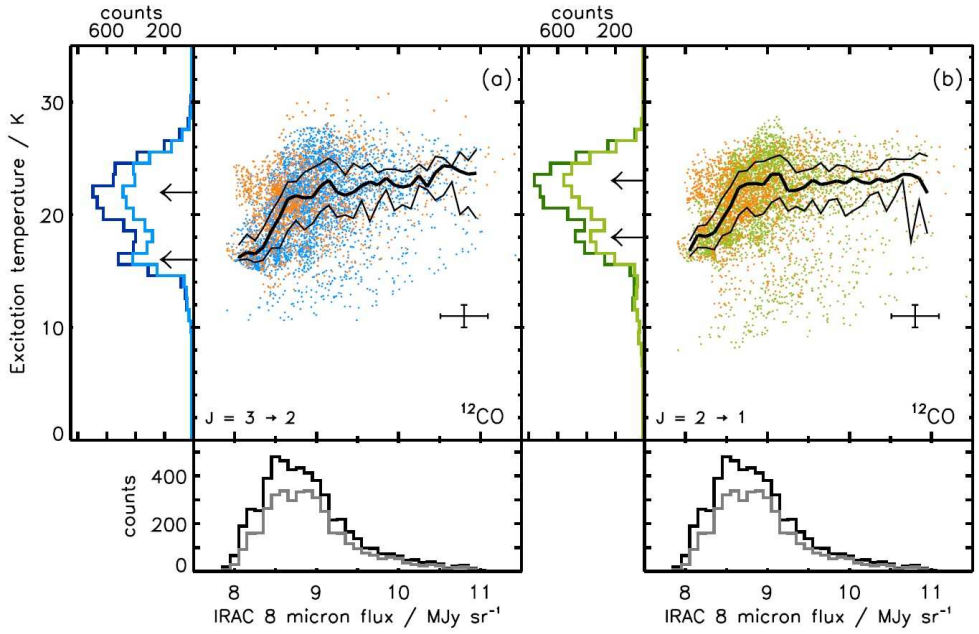

FIGURE 4.9. 40 arcsec resolution version of Fig 4.6. Scatter plot of the 8 μm flux and gas excitation temperature derived from the ^{12}CO (a) $J = 3 \rightarrow 2$ and (b) $J = 2 \rightarrow 1$ transitions to demonstrate that PAH emission and gas temperature are related over a 1.1 × 1.6 pc region, from the PDR to the shielded cloud interior. The blue and green points are from the quiescent region of the cloud and the orange points show the region affected by the YSO. The median of the quiescent distribution is overplotted as a thick black line and the two thin black lines are the upper and lower quartiles (25 per cent). Excitation temperature histograms are plotted to the left (the darker shade includes the YSO points, the lighter shade excludes them), and the IRAC flux histogram is plotted below (black includes the YSO points, grey excludes them). It is clear that the YSO has little effect on the correlation.

to the 'cold' and 'warm' gas regimes are shown in red, defined arbitrarily as ranging from F(8μm) < 8.8 MJy sr^{-1} and F(8μm) > 8.8 MJy sr^{-1}, respectively. The residuals of the fits generally lie within the 3σ error of the ^{12}CO gas excitation temperature. The 'warm, high flux' and 'cold, low flux' regimes are also consistent with a visual analysis of the IRAC 8 μm flux and gas temperature map shown in Fig. 4.5(b). The fit gradients have no real physical meaning, but are consistent as shown in Table 4.4. In the 'cold, low flux' regime the gradients are significantly steeper (e.g. 7.0 ± 1.3 K (MJy sr^{-1})$^{-1}$) than in the 'warm, high flux' regime (e.g. 0.8 ± 0.3 K (MJy sr^{-1})$^{-1}$).

These gradients can be considered as a measure of the heating efficiencies of the two regimes. They indicate the ability of the PAHs to emit photoelectrons, which can further heat the gas (as opposed to the heating that has already occurred). It is assumed that in the 'warm, high flux' regime the PAHs have already been ionized, releasing

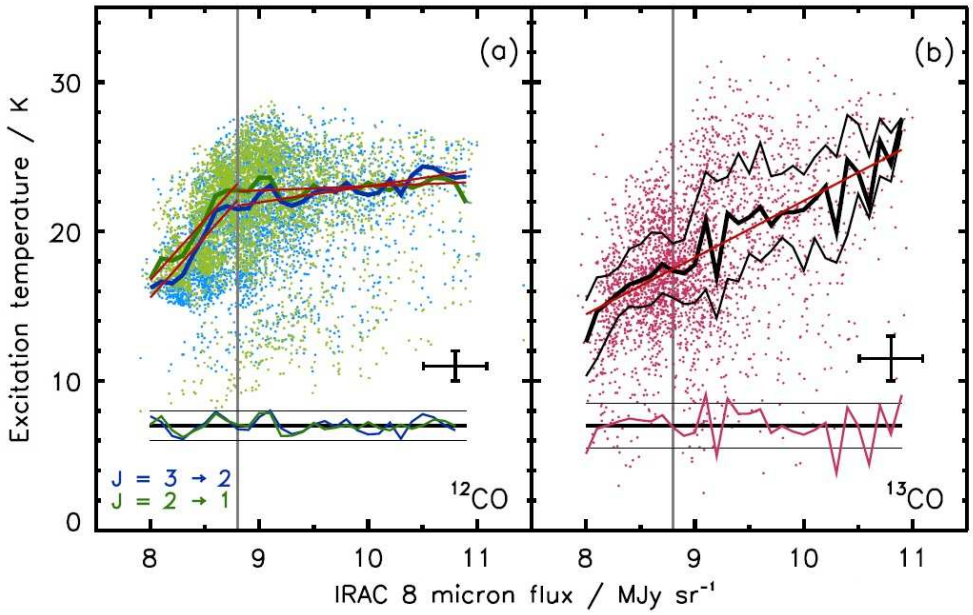

FIGURE 4.10. 40 arcsec resolution version of Fig 4.7. Scatter plot of the 8 μm flux and gas excitation temperature derived from the ^{12}CO $J = 3 \rightarrow 2$ (blue), $J = 2 \rightarrow 1$ (green) and ^{13}CO (pink) transitions to demonstrate that PAH emission and gas temperature are related over a 1.1×1.6 pc region, from the PDR to the shielded cloud interior. (a) Fits to the median lines are shown in red (see text and Table 4.4 for details) and the residuals are plotted below with the black lines indicating the ± 1 K 3σ error in the temperature. The ^{12}CO data are divided into two IRAC 8 μm flux regimes for fitting: 'low' 7.9 to 8.8 and 'high' 8.8 to 10.9 MJy sr^{-1}. There are fewer points in the scatter plot derived from the quiescent ^{13}CO emission (b) as it has a smaller spatial extent. The median and upper and lower quartiles, overplotted as thick and thin black lines respectively, show a single linear correlation. The residuals are plotted below with the black lines indicating the ± 1.5 K 3σ error in the temperature.

a photoelectron which has heated the gas. Successive ionizations of PAH^+ require higher energy UV photons. The probability of continued photoelectric heating therefore decreases and the heating efficiency is low (cf. shallow gradient). Conversely, in the 'cold, low flux' regime the PAHs are presumably abundant and predominantly neutral. The conversion of UV flux into photoelectrons that heat the gas can therefore be efficient (cf. steep gradient).

This analysis has also been carried out on data smoothed to 40 arcsec, which produces clearer maps. Figs. 4.8, 4.9 and 4.10 confirm the correlation on this larger scale. The fit gradients of the smoothed data, shown in Table 4.4, are the same as the smoothed data within the 1σ error.

Fig. 4.7(b) shows the correlation for temperatures derived from the $J = 3 \rightarrow 2$ and

$J = 2 \rightarrow 1$ transitions of ^{13}CO using equation 3.3. As the ^{13}CO emission has a smaller spatial extent there are fewer pixels in this scatter plot, only 2520 (excluding those associated with the YSO). The ^{13}CO is not self shielding, so the correlation is unsurprisingly linear throughout the cloud. The gradient of the fit (2.6 ± 0.6) lies between the gradients for the two components of the ^{12}CO data.

Given that similar temperature distributions are found for both ^{12}CO transitions, the flattening of the slope suggests that the PAH photoelectric heating efficiency has reached a maximum (Hollenbach & Tielens, 1999). PAH heating efficiency,

$$\epsilon = \frac{4.87 \times 10^{-2}}{1 + 4 \times 10^{-3}\gamma^{0.73}} + \frac{3.65 \times 10^{-2}(T/10^4)^{0.7}}{1 + 2 \times 10^{-4}\gamma}, \tag{4.1}$$

decreases with the photo-ionization parameter $\gamma \equiv G_0 T^{1/2}/n_e$ (which is proportional to the degree of ionization), where G_0 is the UV flux enhancement compared to the standard ISM Draine field, T is the temperature and n_e the electron density (Tielens, 2005). Wolfire et al. (1989) have determined that G_0 is 19.95 at the C II edge of B35A using the observed ratios of C II to IR flux and ^{12}CO ($J = 1 \rightarrow 0$) to IR flux. This is used, along with the ^{12}CO gas excitation temperatures, to estimate the heating efficiencies for the cold, shielded cloud interior and warm edge (presented in Table 4.5) assuming G_0 decreases with exp(-A_V), where $A_V = 5$ in the cloud interior and $A_V = 3$ at the ^{12}CO cloud edge. Equation 4.1 gives the heating efficiency compared to fully neutral PAHs, therefore ϵ measures the effect of ionized PAHs on the heating rate. The heating efficiency is found to be lower at the warm edge of the cloud, where many of the PAHs are already ionized, than in the shielded interior where the fraction of neutral PAHs is larger. This agrees with the analysis of Fig. 4.7.

Although the heating efficiency is shown to be responsible, to some extent, for the flattening of the correlation, it is also likely that more efficient cooling has an effect. The rotational transitions of CO are one of the most effective ways of cooling the gas; so regions of higher CO density will cool more efficiently. A full analysis of the cooling due to CO requires the sum of the flux from all its rotational transitions. Fig. 4.11 gives some indication of where the cooling is taking place within the cloud, showing the sum of the integrated intensities of the $J = 3 \rightarrow 2$ and $J = 2 \rightarrow 1$ transitions for ^{12}CO and ^{13}CO. It is evident that CO is cooling the cloud more in the densest regions near the YSO. A scatter plot of the summed ^{12}CO flux, and ^{13}CO flux, against the IRAC 8 μm flux (not including the YSO pixels) is shown in Fig. 4.12. Linear relations with very shallow gradients for both ^{12}CO and ^{13}CO (1.92 ± 0.54 and 0.27 ± 0.03,

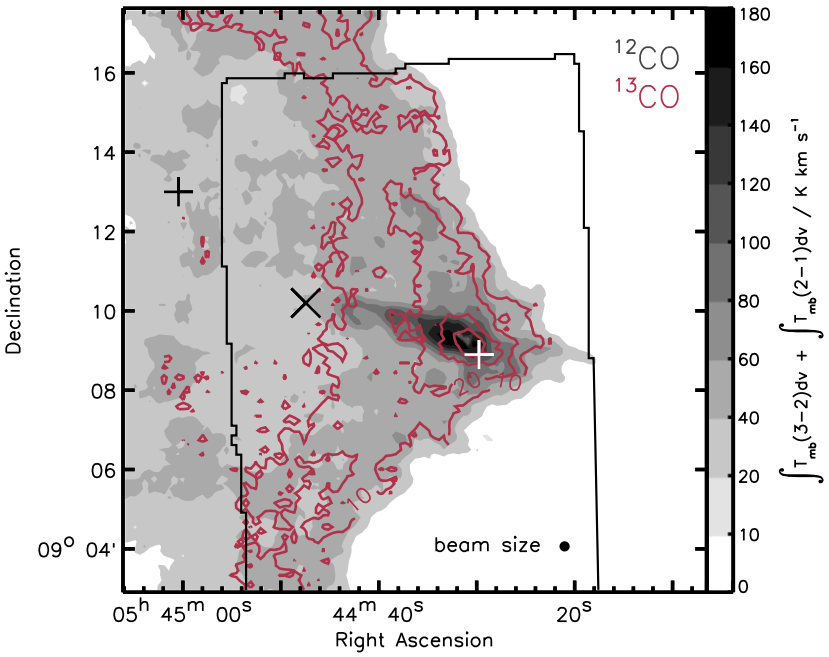

FIGURE 4.11. Maps of the cooling due to CO constructed from the summed integrated intensities of the $J = 3 \rightarrow 2$ and $J = 2 \rightarrow 1$ transitions between 8 and 15 km s^{-1} for both CO isotopologues. The shading shows the ^{12}CO data and the contours the ^{13}CO data, in steps of 10 K km s^{-1}. Objects within the cloud (+ and $\times$) are as described in Fig. 4.1.

respectively) mean that the CO cooling efficiency is essentially uniform across the cloud. Gas-dust interactions are also likely to be involved in the cooling. Morgan et al. (2008) have determined that the dust temperature is 18 K. This is consistent with the gas temperature of the shielded, cold cloud interior, therefore gas-dust collisions in the warm cloud edge will result in gas cooling.

A more traditional method for comparing several maps of a region is to plot the emission intensity along cuts through the maps. Fig. 4.13 shows an IRAC 8 µm map with a contour of the furthest west 23 K gas and three cut positions. Fig. 4.14 shows a horizontal cut through various maps of B35A at 9°13′11.3″(position C on Fig. 4.13). Although the 8 µm emission extends outside the CO cloud boundary, it peaks near the position of high CO excitation temperature (the small peak near $05^h44^m20^s$ is due to a background star). The 450 µm and 850 µm SCUBA data show that the dust morphology is unaffected by the incident UV field. While this is a useful technique for examining *individual* sections, the large number of pixels in these maps (∼9164) mean that a statistical analysis of *all* the data (see Fig. 4.6) is a much more powerful way of exploring a correlation.

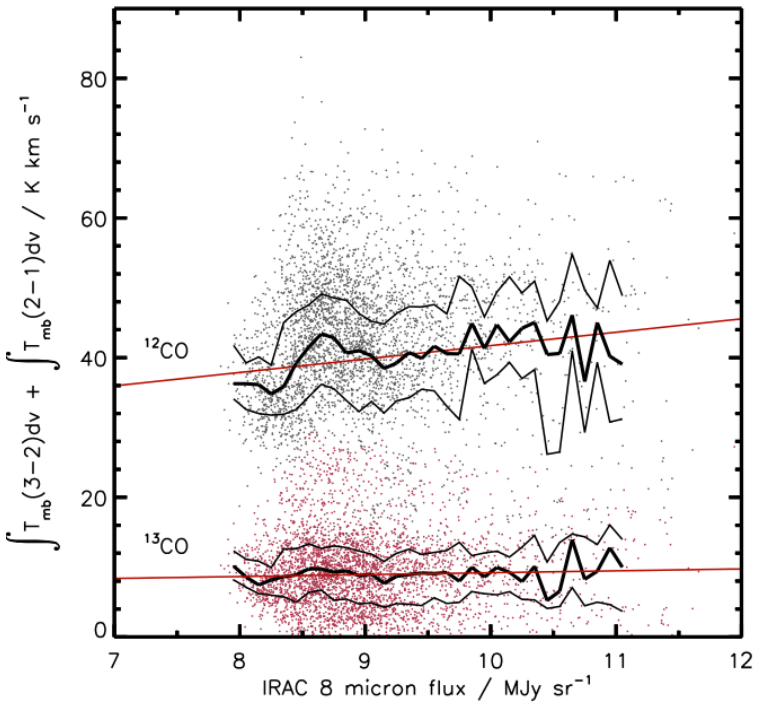

FIGURE 4.12. Scatter plot of IRAC 8 μm flux and the summed integrated intensities of the $J = 3 \rightarrow 2$ and $J = 2 \rightarrow 1$ transitions between 8 and 15 km s^{-1} for ^{12}CO and ^{13}CO (not including YSO pixels), which indicates the cooling due to CO. Medians and upper and lower quartiles (25 per cent) of the distributions are plotted with thick and thin lines, respectively. Fits to the data are shown in red with gradients 1.92 ± 0.54 and 0.27 ± 0.03 for ^{12}CO and ^{13}CO, respectively.

The IRAC 8 μm flux – T_{ex} correlation was also investigated statistically using the Spearman rank correlation test. The Spearman rank correlation coefficient is calculated using,

$$r_{\rm s} = 1 - \frac{6\Sigma_{\rm i} d_{\rm i}^2}{n(n^2+1)}, \tag{4.2}$$

where $d = \bar{x}_i$ - $\bar{y}_i$, the difference between the zero mean ranks in the x and y directions, and n is the number of points. Zero mean ranks are found by ranking the variables by magnitude and subtracting the mean rank. The critical value for the coefficient is calculated using $r_{\rm crit} = z\sqrt{n+1}$, where z = 2.58 for a significance of 99 per cent. The calculated values shown in Table 4.6 exceed the critical values for the two regimes independently and also for the whole flux range. The correlation is therefore statistically proven.

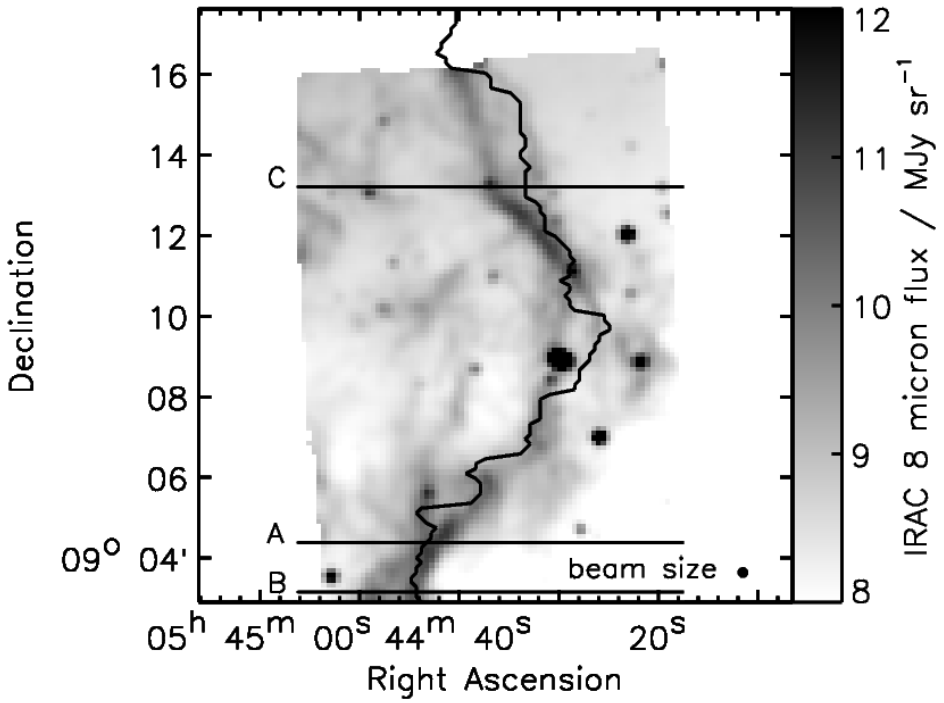

FIGURE 4.13. IRAC 8 μm emission is shown in greyscale, overplotted with the furthest west 23 K contour of the gas temperature (determined using the $J = 2 \rightarrow 1$ transition of ^{12}CO). Cuts lie at: A: +09°04′25.7″; B: +09°03′12.7″; C: +09°13′11.3″.

TABLE 4.4. Change in temperature with 8 μm flux for the two regimes within the cloud (with 1σ errors).

Flux Range (MJy sr^{-1})	J Transition	δT/δ(8μm Flux) 15.3 arcsec	40 arcsec
7.9 - 8.8	$3 \rightarrow 2$	7.0 ± 1.3	8.1 ± 1.3
	$2 \rightarrow 1$	7.5 ± 1.3	8.1 ± 1.3
8.8 - 10.9	$3 \rightarrow 2$	0.8 ± 0.3	1.1 ± 0.4
	$2 \rightarrow 1$	-0.1 ± 0.3	0.3 ± 0.4

TABLE 4.5. Estimates of the heating efficiency (ϵ) in the cold, shielded cloud interior and warm, irradiated edge using the temperatures from the histogram peaks in Fig 4.6. The mean temperature of the two transitions is used in each calculation.

	$T_{3\rightarrow2}$ (K)	$T_{2\rightarrow1}$ (K)	G_0^*	n_e (cm^{-3})	γ	ϵ
Cloud Interior	17±1	18±1	0.13	5×10^{-5}	1.1×10^{4}	1.1×10^{-2}
CO Edge	23±1	23±1	0.99	5×10^{-5}	9.5×10^{4}	0.3×10^{-2}

* G_0 multiplied by exp(-A_V), $A_{V(\text{interior})} = 5$ and $A_{V(\text{CO edge})} = 3$

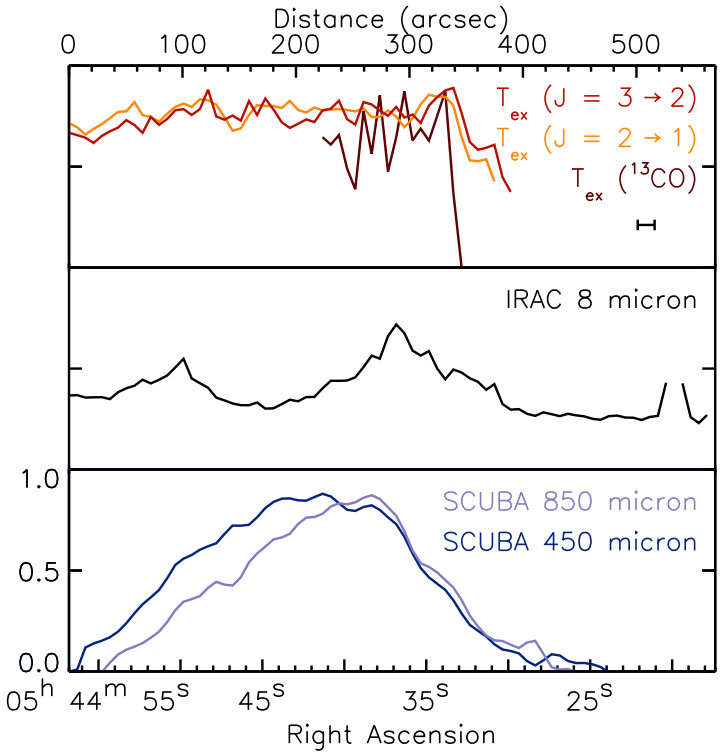

FIGURE 4.14. Normalised emission along a horizontal cut (marked C in Fig. 4.13) through the excitation temperature maps derived from ^{12}CO $J = 3 \rightarrow 2$, $J = 2 \rightarrow 1$, and ^{13}CO, the IRAC 8 μm map and SCUBA maps at 450 and 850 μm. The resolution for all cuts has been convolved to 15.3 arcsec, shown by the error bar.

TABLE 4.6. Spearman rank correlation test for the two regimes within the cloud, and for the whole cloud. Calculated values greater than the critical values prove that a correlation exists, for both map resolutions (15.3 and 40 arcsec).

IRAC 8 μm Flux Range (MJy sr^{-1})	J Transition	r_s 15.3 arcsec	r_s 40 arcsec	r_{crit}
7.9 - 8.8	$3 \rightarrow 2$	0.28	0.35	0.05
	$2 \rightarrow 1$	0.30	0.36	0.05
8.8 - 10.9	$3 \rightarrow 2$	0.14	0.17	0.05
	$2 \rightarrow 1$	0.06	0.08	0.05
7.9 - 10.9	$3 \rightarrow 2$	0.36	0.38	0.03
	$2 \rightarrow 1$	0.32	0.32	0.03

4.4 G_0 RELATION

B35A may seem similar to the well-studied Orion Bar and Horsehead Nebula, where the position of maximum PAH emission (PAH_{max}) is offset from the position of maxi-

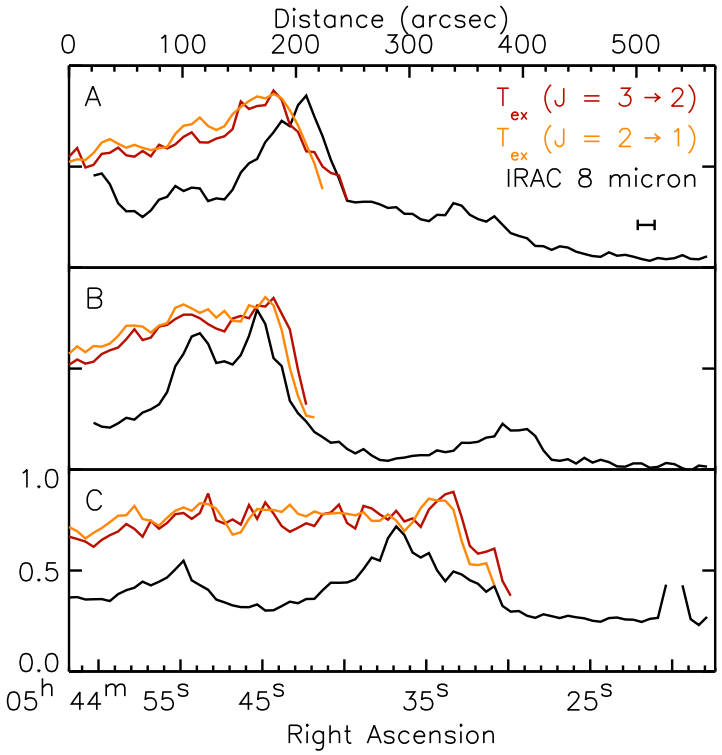

FIGURE 4.15. Normalised horizontal cuts through the maps at three positions demonstrate that the offsets between the maxima of the PAH emission (PAH_{max}) and the excitation temperature (T_{max}, derived from the $J = 3 \rightarrow 2$ and $2 \rightarrow 1$ transitions of ^{12}CO) differ along the cloud edge. The cut locations are shown in Fig. 4.13. Cut A shows PAH_{max} ahead of T_{max}. This morphology has been observed previously in the Orion Bar and Horsehead Nebula, (Tielens et al. (1993) and Habart et al. (2005), respectively), and has been assumed to hold for all PDRs. However, the maxima can be seen to coincide in cut B, and cut C shows T_{max} ahead of PAH_{max}.

mum ^{12}CO emission ($^{12}CO_{max}$) at the edge of the PDR. However, the environment of B35A is sufficiently different to allow an assumption of no offset. The UV flux enhancement, G_0, at the edge of the Orion Bar is 1.4×10^4 (Ysard & Verstraete, 2010) and $\sim$60 for the Horsehead Nebula (Gerin et al., 2005). The bright-rim of B35A, however, is exposed to a G_0 of only 19.95 (Wolfire et al., 1989). PDR structures depend on the G_0/n_H ratio. Fortunately the hydrogen densities are similar in all three PDRs: B35A and Orion Bar $\sim 10^4$ cm^{-3} (Wolfire et al. (1989); Ysard & Verstraete (2010)) and Horsehead Nebula 10^4 – 10^5 cm^{-3} (Goicoechea et al., 2009); so the effect of G_0 alone can be studied.

A high UV flux enhancement results in the photodissociation of CO well into the PDR, hence $^{12}CO_{max}$ is offset from PAH_{max} by about 20 arcsec in the Orion Bar (Tielens et al., 1993). The offset in the Horsehead nebula is much smaller, $\sim$4 arcsec (and negligible

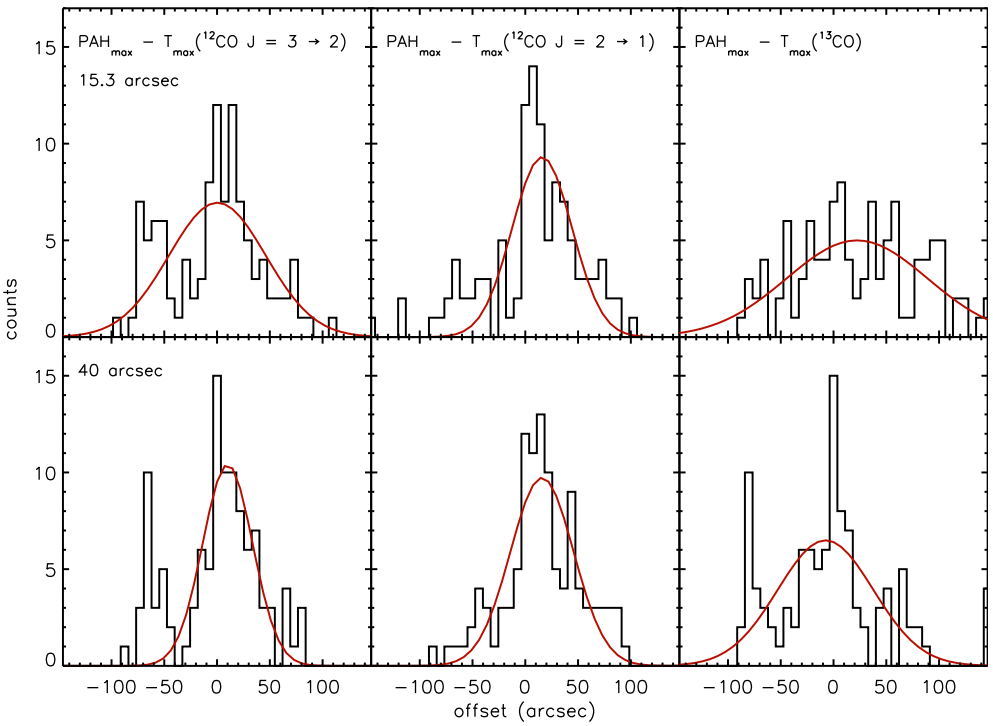

FIGURE 4.16. Each horizontal cut through the map was used to determine the position of maximum PAH emission (PAH_{max}) and the position of maximum excitation temperature (T_{max}) (derived from the ^{12}CO ($J = 3 \rightarrow 2$), ^{12}CO ($J = 2 \rightarrow 1$) and ^{13}CO emission), near the cloud edge. Histograms were constructed using the results of 105 cuts across each map. These histograms show the horizontal offset in position between PAH_{max} and T_{max} for two spatial resolutions; the highest resolution data (15.3 arcsec) are shown in the top row, and the smoothed (40 arcsec) data are plotted below. The zero-point indicates where PAH_{max} and T_{max} occupy the same pixel. All positive values show that PAH_{max} lies ahead of T_{max} and negative values show that T_{max} lies ahead of PAH_{max}. Gaussian fits to the histograms show the average offset between the maxima along the PDR. The fit parameters are given in Table 4.7.

within the 6 arcsec beamsize (Habart et al., 2005)), due to the lower UV flux. These offsets were determined using only a single cut through each cloud. Fig. 4.15 demonstrates that the measured offset in B35A depends on the cut location. The position of maximum IRAC 8 μm emission is used to define PAH_{max} and, as the ^{12}CO emission is optically thick, $^{12}CO_{max}$ is the position of maximum excitation temperature (T_{max}). Cut A shows PAH_{max} ahead of T_{max}. However, the maxima can be seen to coincide in cut B, and cut C shows T_{max} ahead of PAH_{max}. The cut locations are shown in Fig. 4.13.

To determine the offset for the cloud as a whole, 105 of the maps' 116 rows of pixels were examined (4 rows in the vicinity of the YSO were not included due to excess emission and 7 were omitted at the top as the IRAC map is not square). The range of

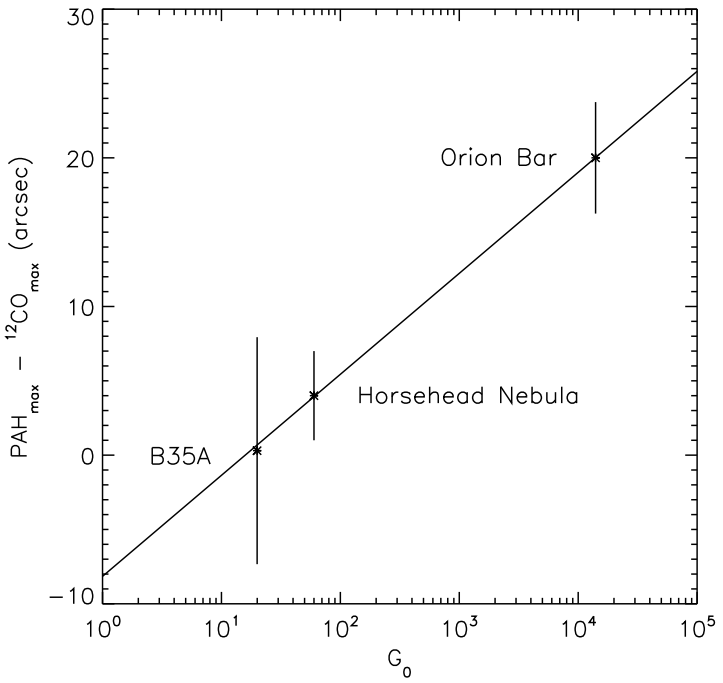

FIGURE 4.17. The offset between positions of PAH_{max} and $^{12}CO_{max}$ (i.e. T_{max}) depends on the incident UV radiation field, G_0. Data was taken from Wolfire et al. (1989), Gerin et al. (2005) and Ysard & Verstraete (2010) for G_0 at B35A, the Horsehead Nebula and the Orion Bar, respectively. The peak position of the high resolution (15.3 arcsec) ^{12}CO $J = 3 \rightarrow 2$ histogram in Fig. 4.16 was used to define the offset for B35A. This method used 105 cuts to determine the offset. The Horsehead Nebula and Orion Bar ^{12}CO data were taken from Habart et al. (2005) and Tielens et al. (1993), respectively, where the offsets were determined by a single cut. Error bars were plotted using the beamsize of the observations.

offsets found between PAH_{max} and T_{max} are displayed as histograms in Fig. 4.16. This analysis was carried out using T_{max} determined from ^{12}CO $J = 3 \rightarrow 2$ and $J = 2 \rightarrow 1$ and from ^{13}CO, for both 15.3 and 40 arcsec map resolutions. Table 4.7 shows the results of Gaussian fits to the histograms, which found that the offsets are small and most lie near zero (using the beamsize as an error bar). Secondary histogram peaks are evident at -50 to -100 and +50 to +100, which are due to a number of cuts in the northern region of the cloud where $^{12}CO_{max}$ lies ahead of PAH_{max}, and a number in the southern region where PAH_{max} lies ahead of $^{12}CO_{max}$. The range of offsets could be explained by the unknown structure of the cloud's third dimension.

A rough comparison of the offsets and G_0 values for B35A, the Horsehead Nebula and Orion Bar suggests a trend. Fig. 4.17 confirms that the magnitude of G_0 is related to the size of the offset between PAH_{max} and $^{12}CO_{max}$. The offset for B35A, +0.3 arcsec, was taken from the fit to the high resolution (15.3 arcsec) data in Fig. 4.16 for

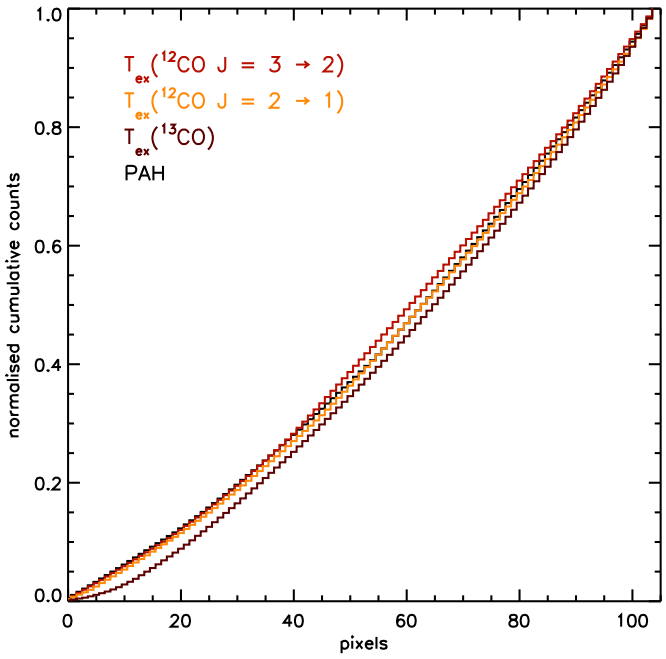

FIGURE 4.18. The cumulative distribution functions (CDFs) of the positions of $T_{\rm max}$ (derived from ^{12}CO J = 3 $\rightarrow$ 2 and J = 2 $\rightarrow$ 1; and ^{13}CO) and PAH$_{\rm max}$ match very closely. The Kolmogorov–Smirnov (K–S) test finds the maximum difference between two CDFs, showing how similar they are. The K-S statistics for these CDFs are given in Table 4.8.

^{12}CO J = 3 $\rightarrow$ 2. The equation of the fit in Fig. 4.17 is PAH$_{\rm max}$ – ^{12}CO$_{\rm max}$(arcsec) = 6.8($\pm$1.9)log$_{10}G_0$ - 8.2($\pm$5.4), which supports the assumption that the offset is around zero for B35A. Prohibitively time-consuming interferometric observations would be necessary to resolve any separation in this cloud.

A Kolmogorov–Smirnov (K–S) statistical analysis provides additional proof that PAH$_{\rm max}$ and $T_{\rm max}$ (hence ^{12}CO$_{\rm max}$) coincide in B35A. This K–S test shows the similarity of two samples by determining the maximum difference between their cumulative distribution functions (CDFs). The CDFs of the positions of PAH$_{\rm max}$ and $T_{\rm max}$ (derived from ^{12}CO J = 3 $\rightarrow$ 2 and J = 2 $\rightarrow$ 1; and ^{13}CO) are plotted in Fig. 4.18. The distributions evidently match very closely, proved by the K–S statistics (maximum difference (D) between two CDFs) shown in Table 4.8. The critical value for 99.9 per cent significance is calculated using D = 1.95 $\sqrt{2n/n^2}$, which for the 105 cuts across the cloud equals 0.27. The K–S statistics are around 10 times lower than this, so the positions of PAH$_{\rm max}$ and $T_{\rm max}$ are statistically the same.

The relationship between G_0 and the PAH$_{\rm max}$ – ^{12}CO$_{\rm max}$ offset is a trend which should be further investigated using multiple cuts across other similarly oriented PDRs with

TABLE 4.7. Parameters (in arcsec) of Gaussian fits to the histograms in Fig. 4.16, showing the average offset between the positions of maximum PAH emission and maximum excitation temperature (derived from CO) along the PDR.

Beamsize	^{12}CO (J=3→2)		^{12}CO (J=2→1)		^{13}CO	
	Offset	FWHM	Offset	FWHM	Offset	FWHM
15.3	+0.3	45.9	+15.9	28.3	+22.3	66.8
40	+10.0	23.7	+15.8	29.9	-7.6	45.3

TABLE 4.8. Kolmogorov–Smirnov statistics for the positions of $T_{\rm max}$ (derived from ^{12}CO $J = 3 \rightarrow 2$ and $J = 2 \rightarrow 1$; and ^{13}CO) and PAH$_{\rm max}$.

Position 1	Position 2	K-S Statistic
$T_{\rm max}$ (^{12}CO $J = 3 \rightarrow 2$)	PAH$_{\rm max}$	0.024
$T_{\rm max}$ (^{12}CO $J = 2 \rightarrow 1$)	PAH$_{\rm max}$	0.011
$T_{\rm max}$ (^{13}CO)	PAH$_{\rm max}$	0.036
$T_{\rm max}$ (^{12}CO $J = 3 \rightarrow 2$)	$T_{\rm max}$ (^{12}CO $J = 2 \rightarrow 1$)	0.024

hydrogen densities around 10^4 cm^{-3}.

4.5 SUMMARY AND CONCLUSIONS

The observations presented in this chapter constitute the first large scale (14.6 × 14.6 arcmin) multi-transition ($J = 3 \rightarrow 2$ and $J = 2 \rightarrow 1$) survey of three CO isotopologues (^{12}CO, ^{13}CO and C^{18}O) in bright-rimmed cloud B35A. They show that the western side of the cloud has a dense ridge and sharp edge, which extend in the north-south direction. The density gradually decreases towards the eastern side of the map, with the exception of a few clumps. H_2 column densities of $\sim$1.2 × 10^{22} cm^{-2} are found in the densest region at the centre of the ridge. This morphology, typical of a type A bright-rimmed cloud, is likely due to the stellar wind or ionization front from the nearby λ Ori OB association compressing the western side of the cloud. UV photons from the OB stars are responsible for the bright-rim and PDR. The gas temperature along the bright-rim is found to be around 23 $\pm$1 K, significantly higher than the interior temperature of 17.5 $\pm$1 K.

It is generally assumed that PAH photoelectric heating takes place in PDRs i.e. photoelectrons ejected from UV irradiated PAHs heat the gas through collisions. This work presents the first observational evidence for a correlation between the intensity of the PAH emission near 8 μm and gas excitation temperature across a 1.1 × 1.6 pc region of

B35A. The large size of the CO and 8 μm flux maps and the favourable orientation of the PDR have enabled a statistically unbiased analysis across the UV irradiated cloud edge and shielded interior. Two distinct regimes are found within the cloud: a warm (20 – 30 K) region along the cloud edge where the 8 μm flux is high (due to the incident UV photons); and a cold region (10 – 20 K) in the shielded cloud interior where the 8 μm flux is low. This results in a clear, two component, linear correlation between the 8 μm flux and gas temperature which rises steeply to around 23 K at 8.8 MJy sr^{-1} and then flattens off. This flattening is, in part, due to a lower heating efficiency at the cloud edge where the PAHs are already ionized and subsequent ionizations require higher energy photons. Cooling mechanisms are also responsible for the flattening. As the dust temperature is 18 K, gas-dust interactions at the warm edge of the cloud are also a mechanism for gas cooling. Using PDR codes and maps of similar coverage of B35A in the main cooling lines C II at 157 μm and O I at 63 and 145 μm would help to understand the shape of the correlation and its relationship with the PAH heating efficiency. In particular, fine structure line ratios will better constrain the UV enhancement G_0 and gas density. A survey of similarly oriented PDRs (i.e. IC 63, Thi et al. (2009)) would determine whether other PDRs also show two distinct regimes with comparable $\delta T/\delta$(8 μm flux).

A previously observed offset between the maxima of PAH and ^{12}CO emission in PDRs is found to depend on the enhanced UV flux, G_0. In PDRs where G_0 is high, the offset is large. However, as G_0 is only $\sim$20 in B35A, the offset is negligible. As the ^{12}CO emission is optically thick, the excitation temperature and ^{12}CO maxima lie at the same positions. The PAH and temperature maxima are therefore co-located and the correlation is valid. Further interferometric observations of CO and PAHs in PDRs with similar hydrogen densities (10^4 cm^{-3}) would better define the relationship between the offset and G_0.

REFERENCES

Armandroff T. E., Herbst W., 1981, AJ, 86, 1923 80

Bakes E. L. O., Tielens A. G. G. M., 1994, ApJ, 427, 822 81

Chapman N. L., Mundy L. G., 2009, ApJ, 699, 1866 86

Connelley M. S., Reipurth B., Tokunaga A. T., 2008, AJ, 135, 2496 79

de Jager C., Nieuwenhuijzen H., 1987, A&A, 177, 217 79

De Vries C. H., Narayanan G., Snell R. L., 2002, ApJ, 577, 798

D'Hendecourt L. B., Leger A., 1987, A&A, 180, L9 80

Dolan C. J., Mathieu R. D., 2002, AJ, 123, 387 85

Draine B. T., Li A., 2007, ApJ, 657, 810

Evans II N. J., Allen L. E., Blake G. A., Boogert A. C. A., Bourke T., Harvey P. M., Kessler J. E., Koerner D. W., et al., 2003, PASP, 115, 965 79

Gerin M., Roueff E., Le Bourlot J., Pety J., Goicoechea J. R., Teyssier D., Joblin C., Abergel A., Fossé D., 2005, in D. C. Lis, G. A. Blake, & E. Herbst ed., Astrochemistry: Recent Successes and Current Challenges Vol. 231 of IAU Symposium, Carbon Chemistry in Photodissociation Regions. pp 153–162 98, 100

Goicoechea J. R., Pety J., Gerin M., Hily-Blant P., Le Bourlot J., 2009, A&A, 498, 771 98

Goorvitch D., 1994, ApJS, 95, 535

Habart E., Abergel A., Walmsley C. M., Teyssier D., Pety J., 2005, A&A, 437, 177 81, 98, 99, 100

Herbst W., Sawyer D. L., 1981, ApJ, 243, 935 80

Hollenbach D. J., Tielens A. G. G. M., 1999, Reviews of Modern Physics, 71, 173 93

Klapper G., Lewen F., Gendriesch R., Belov S. P., Winnewisser G., 2000, Journal of Molecular Spectroscopy, 201, 124

Lai S.-P., Velusamy T., Langer W. D., Kuiper T. B. H., 2003, AJ, 126, 311 86

Lee H.-T., Chen W. P., Zhang Z.-W., Hu J.-Y., 2005, ApJ, 624, 808 85

Lepp S., Dalgarno A., 1988, ApJ, 335, 769 80

Morgan L. K., Thompson M. A., Urquhart J. S., White G. J., 2008, A&A, 477, 557 79, 90, 94

Murdin P., Penston M. V., 1977, MNRAS, 181, 657 79, 80

Myers P. C., Heyer M., Snell R. L., Goldsmith P. F., 1988, ApJ, 324, 907 79

Ogura K., Sugitani K., 1998, Publications of the Astronomical Society of Australia, 15, 91

Park Y., Lee C. W., Myers P. C., 2004, ApJS, 152, 81 86

Pineda J. E., Caselli P., Goodman A. A., 2008, ApJ, 679, 481

Qin S.-L., Wu Y.-F., 2003, Chinese Journal of Astronomy and Astrophysics, 3, 69 79

Röllig M., Abel N. P., Bell T., Bensch F., Black J., Ferland G. J., Jonkheid B., Kamp I., et al., 2007, A&A, 467, 187 81

Schuster K.-F., Boucher C., Brunswig W., Carter M., Chenu J.-Y., Foullieux B., Greve A., John

D., et al., 2004, A&A, 423, 1171

Smith H., Buckle J., Hills R., Bell G., Richer J., Curtis E., Withington S., Leech J., et al., 2008, in SPIE Conference Series Vol. 7020, HARP: a submillimetre heterodyne array receiver operating on the James Clerk Maxwell Telescope

Sugitani K., Fukui Y., Ogura K., 1991, ApJS, 77, 59 79

Thi W., van Dishoeck E. F., Bell T., Viti S., Black J., 2009, MNRAS, 400, 622 103

Tielens A. G. G. M., 2005, The Physics and Chemistry of the Interstellar Medium. Cambridge University Press 93

Tielens A. G. G. M., 2008, ARAA, 46, 289

Tielens A. G. G. M., Meixner M. M., van der Werf P. P., Bregman J., Tauber J. A., Stutzki J., Rank D., 1993, Science, 262, 86 81, 98, 100

van der Tak F. F. S., Black J. H., Schöier F. L., Jansen D. J., van Dishoeck E. F., 2007, A&A, 468, 627 85

Verstraete L., Leger A., D'Hendecourt L., Defourneau D., Dutuit O., 1990, A&A, 237, 436 80

Weingartner J. C., Draine B. T., 2001, ApJS, 134, 263 81

Wilson T. L., Rood R., 1994, ARAA, 32, 191

Wolfire M. G., Hollenbach D., Tielens A. G. G. M., 1989, ApJ, 344, 770 81, 93, 98, 100

Ysard N., Verstraete L., 2010, A&A, 509, A12+ 98, 100

CHAPTER 5

PHOTODESORPTION AHEAD OF A PRECESSING OUTFLOW IN BARNARD 35A

SYNOPSIS

This chapter explores the theory that photodesorption ahead of a precessing outflow has resulted in an arc of clumps of enhanced CO emission in bright-rimmed cloud B35A. The cloud morphology and kinematics across a 1.7 $\times$ 1.7 pc region are investigated using observations of three isotopologues and two transitions of CO.

An outflowing Class I YSO, with a binary companion, is embedded within the bright rim. A velocity analysis shows that its outflows are oriented perpendicular to the line-of-sight ($\sim$80 – 89°) and the western outflow causes a protrusion in the cloud edge. A velocity variation is also found along the eastern outflow, which indicates episodic ejections. The eastern outflow is aligned with an HH object and a clump of enhanced CO emission beyond. Photodesorption of CO ice from the surface of dust grains is proposed as the source of this enhanced emission. A chain of similar clumps, following a $\sim$45° arc equidistant from the YSO, suggest that the outflow is precessing. The binary companion may be in an inclined orbit with tidal interactions between the disks inducing the precession.

5.1 INTRODUCTION

5.1.1 BARNARD 35A

B35A is a bright-rimmed cloud, described in detail in Section 4.1.1. It was observed in three isotopologues and two transitions of CO (^{12}CO, ^{13}CO and C^{18}O; $J = 3\rightarrow2$ and $J = 2\rightarrow1$) for the gas-solid mapping project, introduced in Section 1.5. Objects of note within B35A are plotted in the diagram in Fig. 5.1. Class I YSO IRAS 05417+0907 is the primary of a close binary system (Connelley et al., 2008) embedded within the dense ridge at the western edge of the cloud; its eastern outflow is aligned with Herbig–Haro object 175 (HH 175) (Myers et al., 1988). Another IRAS source (IRAS 05422+0911), which lies at the eastern side of the cloud, remains unidentified.

Full details of the observations are presented in Chapter 2 and the initial analysis of the data is described in Chapter 3. In Chapter 4 the CO observations revealed a warm dense ridge with a sharp western edge, heated and compressed by O8 III star λ Ori. The thermal balance of the cloud was discussed and it was shown that photoelectric heating occurs in the PDR along this western edge. In this chapter a detailed analysis is presented of the gas morphology and kinematics across a 1.7 $\times$ 1.7 pc region of B35A. The physical characteristics of the outflows are explored and the origin of an arc of clumps equidistant from YSO IRAS 05417+0907 is investigated.

5.1.2 BIPOLAR JETS AND MOLECULAR OUTFLOWS

Bipolar jets are ejected as a star forms by gravitational collapse. As described in Section 1.2.1, the surrounding molecular gas is entrained and accelerated by the jets forming molecular outflows, which are observed at higher (and lower) line-of-sight velocities than the quiescent cloud. These jets can have a significant effect on the morphology and kinematics of the cloud. CO outflows are easily observed (e.g. Hatchell et al. (1999); Knee & Sandell (2000); Davis et al. (2000); Hatchell et al. (2007); Lee et al. (2007); Bussmann et al. (2007); Yeh et al. (2008); van Kempen et al. (2009); Klaassen et al. (2016)). Episodic ejections have been observed in many young molecular outflows, such as L1157 (Gueth et al., 1998) and IRAS 04239+2436 (Arce & Goodman, 2001a). Several shocks are evident along these outflows and position–velocity diagrams show a jagged profile (Arce & Goodman, 2001b). The episodic nature of ejec-

tions may be explained by sudden changes in the stellar accretion rate.

Shocks can significantly affect the chemical composition where a supersonic jet passes through a region. Heating and compression can induce processes such as molecular dissociation and ice desorption from dust grains (Jørgensen et al., 2004). This influences the observed column density of gaseous molecules.

Herbig–Haro (HH) objects are regions where jets collide with the molecular cloud, interacting hydro-dynamically and causing strong atomic line emission. There is evidence that UV radiation produced in the shock affects the chemical composition of material ahead of the HH object e.g. Viti et al. (2006). Enhanced clumps of HCO^+, CO and NH_3 emission have been detected ahead of HH objects. It is likely that this emission is caused by molecules photodesorbed from dust grains in dense clumps near the head of the jet (Girart et al., 1994). As this emission is cool and quiescent, the high molecular abundances can not be attributed to shock chemistry.

Precession of the jets occurs where the ejection axis is not aligned with the star's rotation axis. These jets trace out a conical surface. Precessing outflows have previously been observed in sources such as Cep E (Eisloffel et al., 1996), and L1157 (Gueth et al., 1996, 1998). Where the precession angle is large, a significant region of gas may be swept out by the jets.

5.2 CLOUD KINEMATICS

5.2.1 SPECTRA

Emission spectra are excellent tracers of the gas kinematics in a cloud. Fig. 5.1 shows the median emission across 5×5 pixels (15000×15000 AU, approximately 40 arcsec: the map resolution) in five regions of B35A: quiescent gas, the IRAS source, the YSO, a point midway along the outflow, and the HH object. The peak intensity, velocity and FWHM of each emission spectrum are shown in Table 5.1. The ^{12}CO and ^{13}CO spectra in Fig. 5.1(a) are symmetric, showing a Gaussian distribution around a single velocity, as expected for a quiescent region. The cloud velocity is found to be 12.42 km s^{-1}, the average of the two transitions of ^{12}CO in the quiescent region. C^{18}O is not detected in this quiescent region because it is situated far from the dense core. In fact, quiescent C^{18}O is not found anywhere in this cloud as the outflowing YSO is located in the only region dense enough.

The ^{12}CO emission in the region of the unidentified IRAS source, Fig. 5.1(b), is asymmetric and red-shifted from the cloud velocity, peaking at $\sim$12.8 km s^{-1}. This is due to its proximity to a high velocity clump ($\sim$13 km s^{-1}), which is discussed in Section 5.4. The other isotopologues are not detected due to the low density of the region.

The YSO spectra, in contrast, show broad blue-shifted components (Fig. 5.1(c)). This has previously been attributed to infalling gas in the envelope (De Vries et al. (2002), hereafter deV02). The 25 pixels, shown in the upper panel of Fig. 5.2, from which the median ^{12}CO ($J = 2 \rightarrow 1$) spectrum in Fig. 5.1(c) was constructed, all display this profile. If this shape is indeed due to the infalling motions of the envelope (radius $\sim 10^4$ AU (Lommen et al., 2008)), the same profile will be found in the 49 pixels centred on the YSO (each pixel 2920 $\times$ 2920 AU). The spectra at the outer edge of the envelope are shown in the lower panel of Fig. 5.2 (the inner ring of 8 spectra). As the ^{12}CO $J = 2 \rightarrow 1$ beamsize is 15.3 arcsec (6.12×10^3 AU), the outer 16 spectra in the lower panel of Fig. 5.2 (4.67×10^4 AU from the YSO) should not include any infalling gas. However, blue-shifted emission is clearly evident in the northeast (top left bold L) which is unlikely to be infalling gas but rather outflowing gas entrained by the jet. It is therefore possible that the blue-shifted emission within the envelope is not entirely due to infalling gas, but caused to some extent by the outflow.

The outflow spectra, Fig. 5.1(d), show a broad profile, which includes both blue and red shifted emission. The range of possible bipolar outflow orientations means it is more common to observe red-shifted emission in one outflow and blue-shifted emission in its counterpart. Finding both in one outflow suggests that it is oriented perpendicular to the line-of-sight and the red- and blue-shifted emission are due to the opening angle. This is discussed further in sections 5.2.2 and 5.3.1.

The emission is non-Gaussian and less intense at the HH object position (10.8 and 12.8 K, for $J = 3 \rightarrow 2$ and $J = 2 \rightarrow 1$, respectively), Fig. 5.1(e), than in the quiescent region (17.5 and 22.4 K) or the YSO region (17.0 and 20.5 K). It is possible that some CO molecules are dissociated either by the shock or UV photons (van Kempen et al., 2009). Observations of enhanced C I would add weight to this theory.

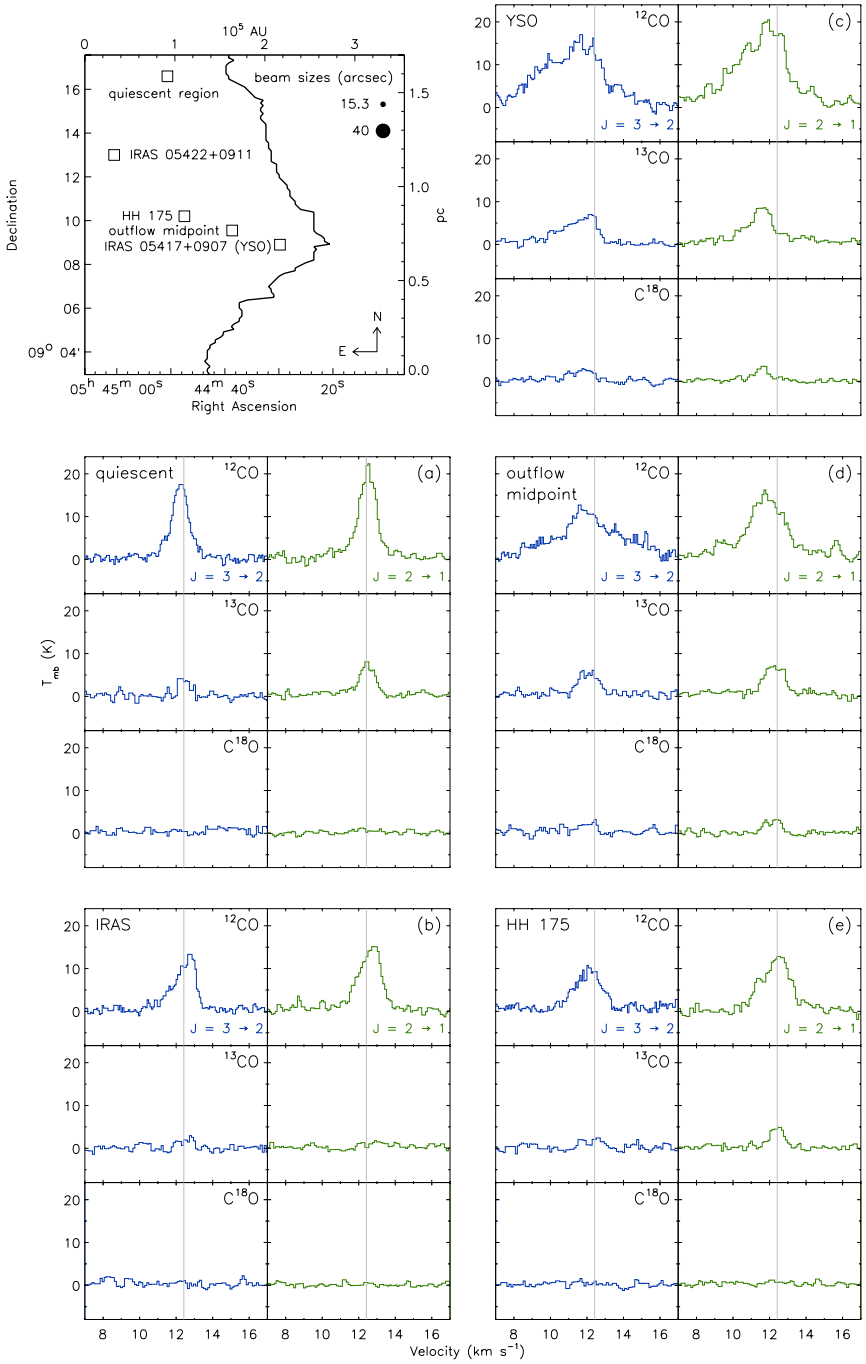

FIGURE 5.1. Objects of interest and the edge of the 5σ detection of ^{12}CO ($J = 2 \rightarrow 1$) in B35A. IRAS 05417+0907 is a Class I YSO whose jet is aligned with HH 175 (Myers et al., 1988). IRAS 05422+0911 is unidentified. A point midway along the outflow is also shown and a quiescent region in the north of the cloud (used to identify the cloud velocity). Black squares indicate the six (5 × 5 pixel) regions from which median spectra are determined for the following panels in this figure. The cloud velocity is shown at 12.42 km s^{-1} in all spectra. (a) quiescent region: ^{12}CO and ^{13}CO are symmetric but C^{18}O is not detected as the region is diffuse. (b) IRAS region: ^{12}CO has a red-shifted component. ^{13}CO and C^{18}O are not detected, indicating that this region is not dense. (c) YSO region: broad blue-shifted components may be the result of outflows. (d) A region midway along the outflow: blue and red shifted emission contribute to these broad profiles. (e) HH 175 region: peaks are lower than in the quiescent region and non-Gaussian. This may indicate photo-dissociation due to the shock.

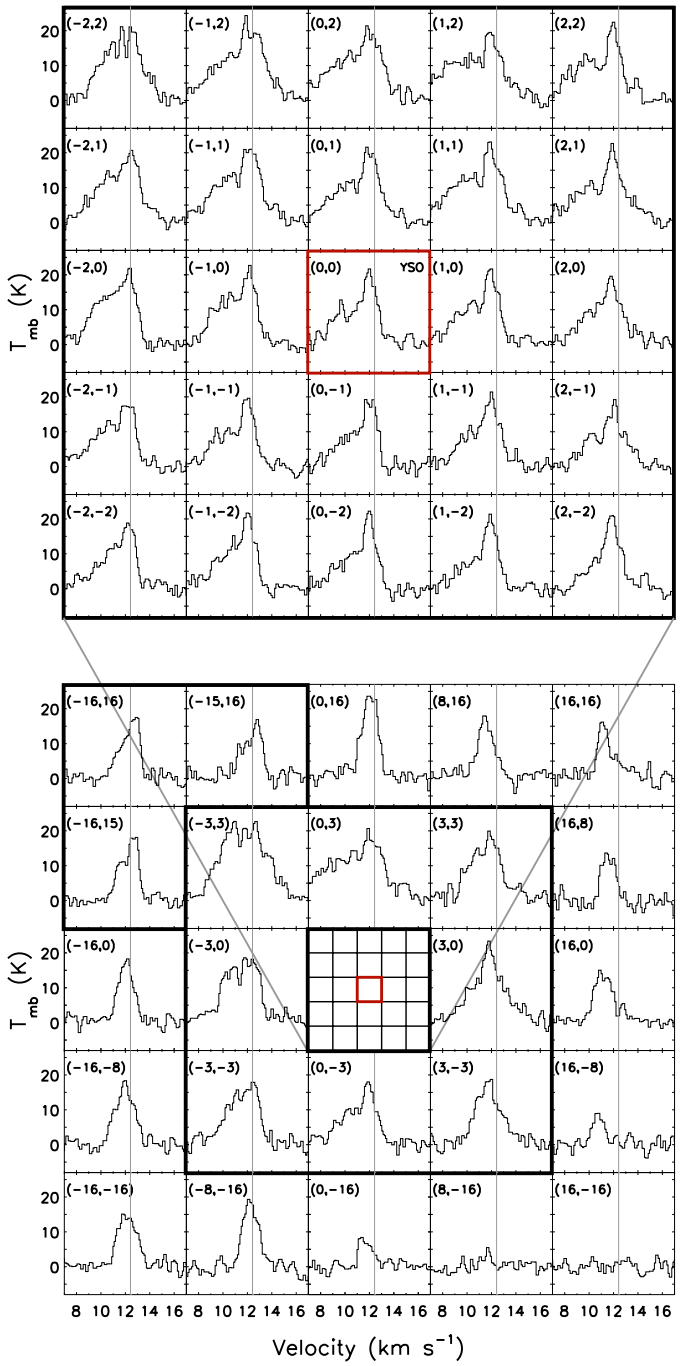

FIGURE 5.2. ^{12}CO $J = 2 \rightarrow 1$ spectra around the YSO pixel showing that the blue-shifted emission is not confined to the circumstellar envelope. The cloud velocity is indicated at 12.42 km s^{-1}. The upper panel shows the spectra of the YSO and surrounding 24 pixels, all of which lie within the envelope. One pixel is 2.92 $\times$ 10^3 AU, therefore the upper panel shows the emission out to a radius of 5.84 $\times$ 10^3 AU. The lower panel shows spectra further from the YSO. The inner ring of 8 spectra in the lower panel (8.76 $\times$ 10^3 AU) also lie within the envelope (radius $\sim$10^4 AU), as indicated by the large bold square. However, the outer 16 do not (4.67 $\times$ 10^4 AU). Although the three northeastern spectra (top left bold L) are outwith the envelope, they show the same blue-shifted emission. This is due to the outflow. The blue-shifted emission within the envelope may therefore be due, in part, to the outflow and not entirely caused by infalling gas.

TABLE 5.1. Parameters of the emission lines shown in Fig. 5.1. The peak intensity and velocity are shown where the maximum emission is greater than the 3σ detection limit. FWHM are shown where the half-maximum emission is greater than the 3σ detection limit.

Region	RA (J2000)	Dec (J2000)	Isotopologue & J Transition	$T_{\rm mb}$ Peak (K $\pm$ 10 %)	Velocity (km s^{-1} $\pm$ 0.15)	FWHM (km s^{-1} $\pm$ 0.3)
Quiescent	05 44 50.7	+09 16 36	^{12}CO 3 $\rightarrow$ 2	17.49	12.28	1.03
			2 $\rightarrow$ 1	23.36	12.56	1.02
			^{13}CO 3 $\rightarrow$ 2	4.13	12.23	-
			2 $\rightarrow$ 1	8.07	12.44	0.96
			^{13}CO 3 $\rightarrow$ 2	4.03	12.23	-
			2 $\rightarrow$ 1	5.67	11.97	1.17
IRAS	05 45 00.5	+09 13 00	^{12}CO 3 $\rightarrow$ 2	13.31	12.75	1.11
			2 $\rightarrow$ 1	15.11	12.86	1.52
YSO	05 44 29.8	+09 08 54	^{12}CO 3 $\rightarrow$ 2	17.01	11.68	3.81
			2 $\rightarrow$ 1	20.50	11.95	2.54
			^{13}CO 3 $\rightarrow$ 2	6.97	12.18	1.99
			2 $\rightarrow$ 1	8.59	11.75	1.38
			C^{18}O 2 $\rightarrow$ 1	3.54	11.64	-
Outflow Midpoint	05 44 38.8	+09 09 18	^{12}CO 3 $\rightarrow$ 2	12.72	11.60	2.22
			2 $\rightarrow$ 1	16.23	11.74	2.13
			^{13}CO 3 $\rightarrow$ 2	6.11	12.34	1.22
			2 $\rightarrow$ 1	7.18	12.28	1.38
			C^{18}O 3 $\rightarrow$ 2	3.22	12.45	-
			2 $\rightarrow$ 1	3.18	12.38	-
HH 175	05 44 47.5	+09 10 12	^{12}CO 3 $\rightarrow$ 2	10.75	12.04	1.43
			2 $\rightarrow$ 1	12.82	12.51	2.13
			^{13}CO 2 $\rightarrow$ 1	4.88	12.91	-

5.2.2 CHANNEL MAPS

A detailed inspection of the channel map morphology provides insights into the kinematics of the gas, prompting further analysis. Fig. 5.3 shows the emission in channels of 0.25 km s^{-1} from 10.25 to 13.75 km s^{-1} (i.e close to the cloud velocity) for both transitions of ^{12}CO and ^{13}CO. The ^{12}CO maps clearly show less emission at the north end of the cloud for lower velocities (e.g. 11.00 – 11.25 km s^{-1}) and less emission at the south end for higher velocities (e.g. 13.00 – 13.25 km s^{-1}). A simple analysis would indicate that the cloud is rotating about an east – west axis, similar to the Serpens cloud's rotation about a north – south axis (Olmi & Testi, 2002). Using observations of a 5 $\times$ 7 arcmin region of B35A Goodman et al. (1993) found a linear velocity gradient in the northeast – southwest direction, suggesting solid-body rotation. However, a more detailed investigation reveals a more complex story. The higher velocity ^{12}CO gas (13.00 – 13.50 km s^{-1}) shows a triangular hole extending eastwards from the YSO towards the HH object and terminating with an arc of clumps at the eastern edge of the cloud, around 0.5 pc from the YSO. This hole is more noticeable in the $J = 3 \rightarrow 2$ maps than the $J = 2 \rightarrow 1$ maps as the height of the upper J level above ground for the two transitions (33.2 and 16.6 K, for $J = 3 \rightarrow 2$ and $J = 2 \rightarrow 1$, respectively) means that the $J = 2 \rightarrow 1$ transition is more easily excited. The alignment of the outflow with the northern edge of the hole and arc of clumps bordering the hole's eastern edge lead to the theory that the YSO's eastern jet is precessing and has swept out this segment. This theory is discussed in detail in Section 5.4.

The arc of clumps at the eastern edge of the triangular hole are evident only at median to high velocities, 12.25 – 13.50 km s^{-1}. Although gas is also present at lower velocities, the clumps do not appear in those channel maps. The nature, origin and fate of the clumps are discussed in Section 5.4.

The high (13.25 – 13.75 km s^{-1}) and low (10.25 – 10.75 km s^{-1}) velocity ^{12}CO channel maps (i.e the red- *and* blue-shifted gas) clearly show a linear outflow from the YSO towards the HH object. As described in Section 5.2.1, bipolar outflows are typically seen with red- and blue-shifted components extending in opposite directions from the YSO. In this case the outflows are oriented perpendicular to the line-of-sight, with the opening angle responsible for the co-location of red and blue outflows. This is discussed further in Section 5.3.1.

The ^{13}CO channel maps show a dense region around the YSO and a ridge along the

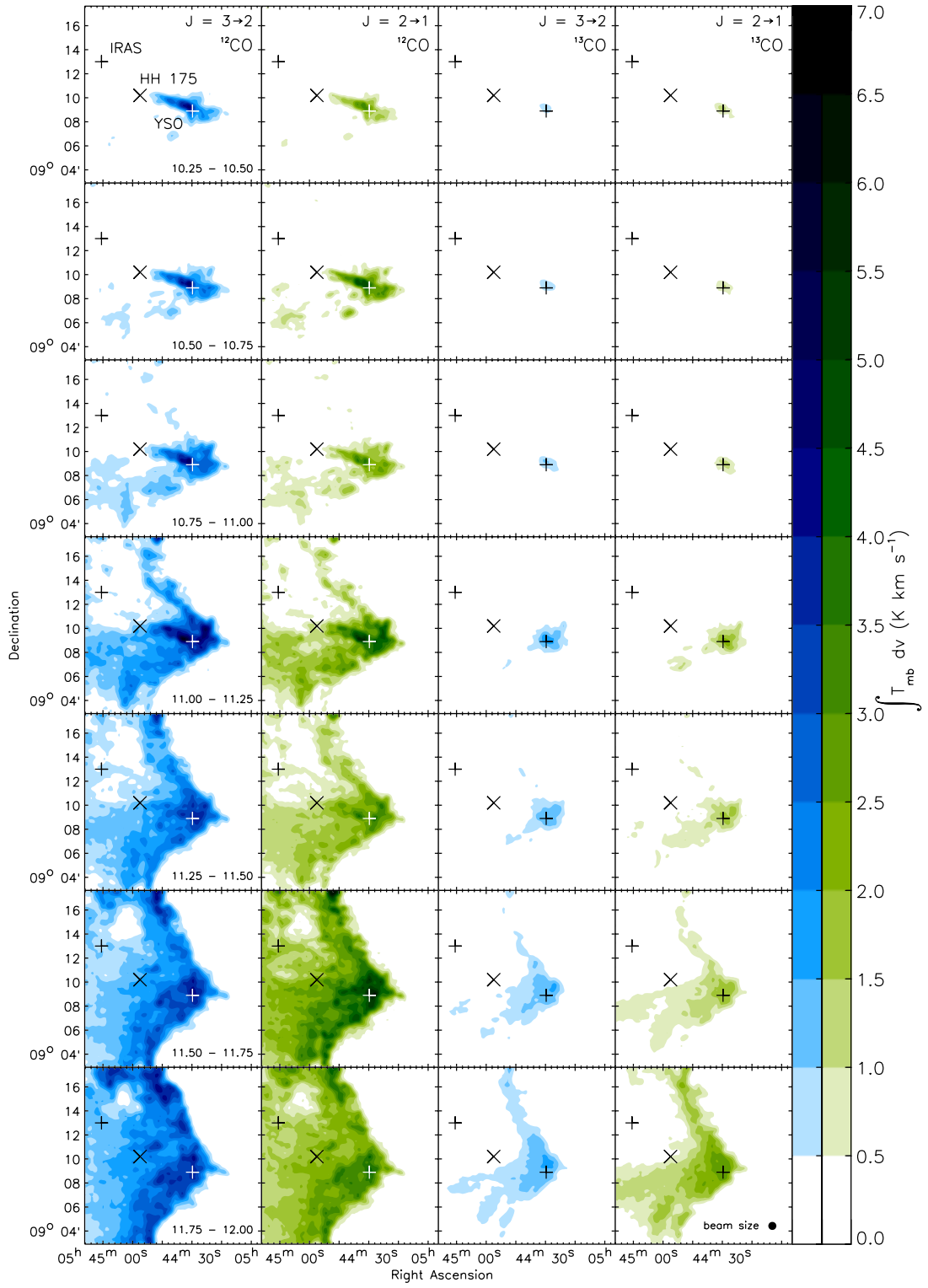

FIGURE 5.3. From left: channel maps for ^{12}CO 3→2, ^{12}CO 2→1, ^{13}CO 3→2 and ^{13}CO 2→1. Integrated emission from 10.25 to 12.0 km s^{-1} in channels of 0.25 km s^{-1}. These maps show less emission at the northern end of the cloud than the southern.

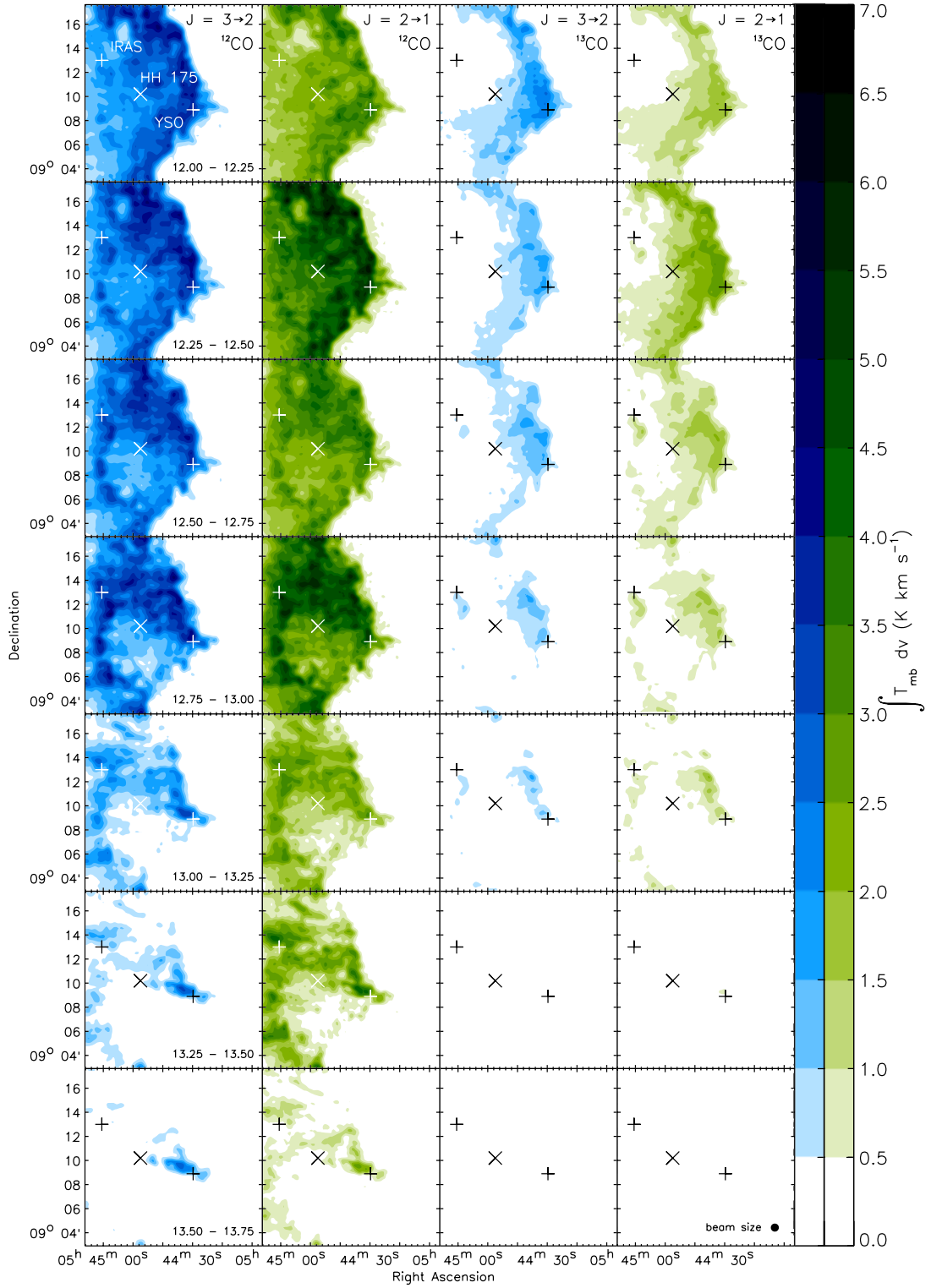

FIGURE 5.3 CONTINUED. From left: channel maps for ^{12}CO 3→2, ^{12}CO 2→1, ^{13}CO 3→2 and ^{13}CO 2→1. Integrated emission from 12.0 to 13.75 km s^{-1} in channels of 0.25 km s^{-1}. The higher velocity ^{12}CO gas (13.00 – 13.50 km s^{-1}) shows a triangular hole extending eastwards from the YSO and terminating with an arc of clumps at the eastern edge of the cloud, around 0.5 pc from the YSO. This triangular hole may have been swept out by a precessing outflow (see Section 5.4).

western edge of the cloud where the gas has been compressed by winds from O8 III star λ Orionis. The triangular hole and arc of clumps are also evident in ^{13}CO (e.g. 12.75 – 13.00 km s^{-1}).

5.2.3 VELOCITY

The cloud velocity of 12.42 km s^{-1} (see Section 5.2.1) describes the line-of-sight recession of the cloud as a whole. The cloud velocity has been previously determined by Maddalena et al. (1986) (11.5 km s^{-1}), Claussen et al. (1996) (11.8 km s^{-1}) and Li et al. (2007) (12.28 km s^{-1}). Although seeming to steadily increase, this range of velocities can be explained by the cloud's internal motions. The observed region over which a median velocity is determined will have an effect on the value and this cloud is far from quiescent.

The cloud kinematics are most easily described with a position–velocity map. Fig. 5.4 shows the velocity at which the emission peaks in each pixel. The $J = 3 \rightarrow 2$ (left hand side) and $J = 2 \rightarrow 1$ (right hand side) transitions have very similar velocity structures. The ^{12}CO emission shows three distinct regions: a low velocity component extending from the west of the YSO to the edge of the cloud and also in clumps along the eastern outflow; an intermediate velocity component south of the YSO incorporating the edge of the cloud and the triangular region; and a high velocity component in the north-eastern region of the cloud and to the east of the triangular region. The protrusion to the west of the YSO, in both transitions of ^{12}CO, has a velocity similar to that of the outflow to the east. This suggests that the protrusion has been formed by the western jet as it ploughs through the dense ridge. The ^{13}CO maps show a similar morphology although the outflows are not evident in this less abundant isotopologue. Although the C^{18}O emission only traces the dense region near the YSO, it also shows lower velocities to the south and west of the YSO and higher velocities to the north.

5.3 YSO OUTFLOWS

Bipolar jets from the YSO are likely to be responsible for most of the kinematic disruption in B35A. They entrain CO along their length resulting in a wider range of velocities than observed in quiescent regions. The YSO's position at the western edge of the cloud means that the eastern jet has a greater effect than its western counterpart.

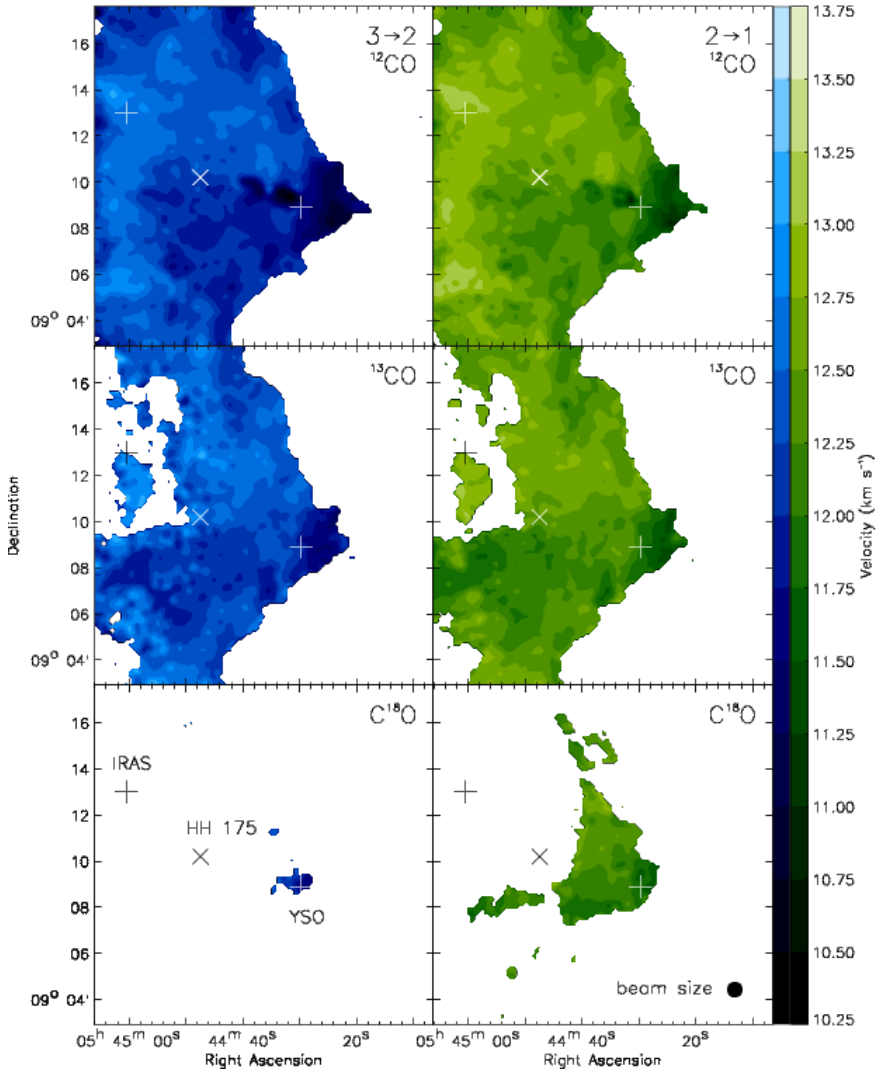

FIGURE 5.4. Position–velocity maps show the velocity at which the emission peaks for all 3 isotopologues in the $J = 3 \rightarrow 2$ and $J = 2 \rightarrow 1$ transitions. The ^{12}CO emission shows three distinct regions: a low velocity component extending from the west of the YSO to the edge of the cloud and also along the outflow to the east of the cloud; an intermediate velocity component south of the YSO incorporating the edge of the cloud and the triangular region; and a high velocity component in the north-eastern region of the cloud and to the east of the triangular region. This velocity structure is also evident in the ^{13}CO and C^{18}O emission.

5.3.1 ORIENTATION

Fig. 5.5 shows ^{12}CO channel maps for both transitions from 8 to 15 km s^{-1} in channels of 1 km s^{-1} (a wider velocity range than shown in Fig. 5.3). The outflow emission is linear, red- and blue-shifted, and extends from the YSO to HH 175. These outflows

are unusual as the red- and blue-shifted CO are co-located. Bipolar outflows are more commonly observed with red- and blue-shifted emission extending in opposite directions from a YSO (e.g. Fig. 5.6). Therefore, it is likely that these outflows are oriented perpendicular to the line-of-sight as described in Fig. 5.7. The co-located red- and blue-shifted emission are then due to the opening angle of the eastern outflow, which extends into the less dense central region of the cloud.

The western outflow is truncated where it encounters the dense ridge of the the cloud. The jet may blow out through the dense western ridge but the outflow can only be observed where there is CO gas to be entrained.

The line-of-sight outflow velocity is low, only $\sim$1-4 km s^{-1} relative to the cloud velocity. Typical outflow velocities for low mass stars are 10-100 km s^{-1} (Arce et al., 2007). This supports the theory that a large component of the velocity is perpendicular to the line-of-sight and hence undetectable in a Doppler shift analysis. Assuming an inclination to the line-of-sight of 80 – 89°results in outflow velocities of $\sim$14 – 182 km s^{-1}.

5.3.2 PROPERTIES

To analyse the outflowing material without any contribution from the quiescent gas, a 'cloud Gaussian profile' is removed from the entire dataset. Fig. 5.8 illustrates this method. The profile is determined by fitting a Gaussian to the median spectrum of 15 $\times$ 15 pixels in the quiescent region. This profile is then scaled to the emission in each pixel in the map (using a fixed peak position and FWHM), and subtracted from it. This method is used for both ^{12}CO and ^{13}CO maps. Fig. 5.8 shows the residual red and blue integrated intensity maps for the two isotopologues. A quiescent region in the north of the cloud, with a velocity of 12.42 km s^{-1}, was selected for this analysis. As there is very little *residual* ^{13}CO emission it can be assumed that the *residual* ^{12}CO emission is optically thin and a lower limit is found for the mass of both the red- and blue-shifted emission.

As this region of B35A is dense, local thermodynamic equilibrium (LTE) is assumed and the excitation temperature is calculated using,

$$T_{\rm ex}(^{12}{\rm CO}) = \frac{T_0}{\ln[1 + T_0/(T_{\rm max} + const)]} \ {\rm K}, \tag{5.1}$$

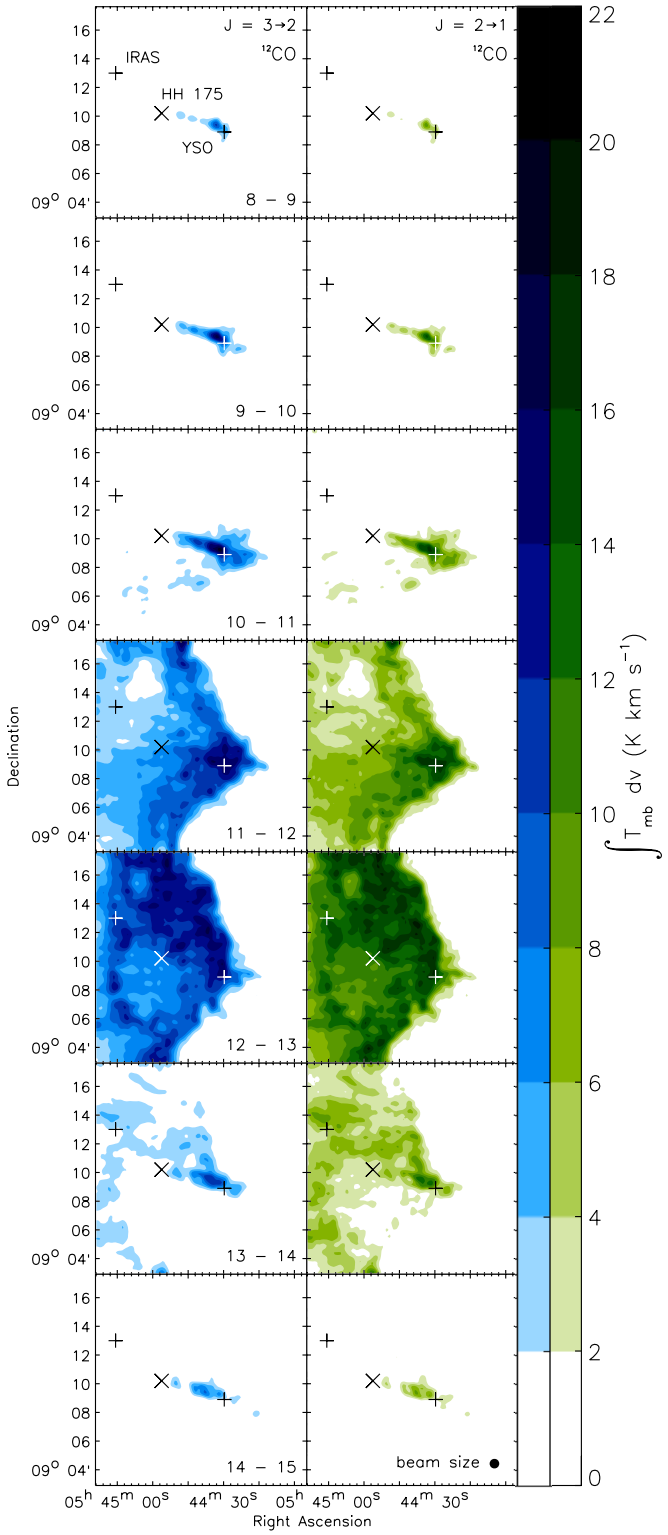

FIGURE 5.5. Channel maps for ^{12}CO ($J = 3 \rightarrow 2$ and $2 \rightarrow 1$) with velocity range 8 to 15 km s^{-1} in channels of 1 km s^{-1}. Outflowing gas is evident at high and low velocities. Co-located red- and blue-shifted outflow emission suggests that the outflow is aligned perpendicular to the line-of-sight. The high and low velocity components are due to the outflow opening angle. This theory is supported by the low line-of-sight outflow velocity (∼1–4 km s^{-1}).

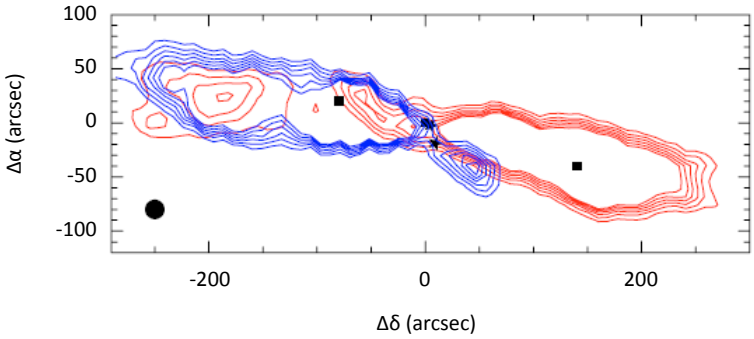

FIGURE 5.6. Bipolar outflows in Bok globule BHR71 demonstrating the typically observed orientation, reproduced from Parise et al. (2006), Fig. 1(b). Integrated CO (J = 3→2) emission, with velocities -14 to -6 km s^{-1} in blue and -3 to 5 km s^{-1} in red, shows two pairs of bipolar outflows with distinct blue- and red-shifted lobes. Contours are from 7.5 to 30 in 4 K km s^{-1} increments. Higher flux contours are omitted from the large outflows to better show the fainter pair of outflows with red and blue lobes in opposite directions. The locations of the two protostellar sources are shown by the black stars and the beamsize is indicated by the circle.

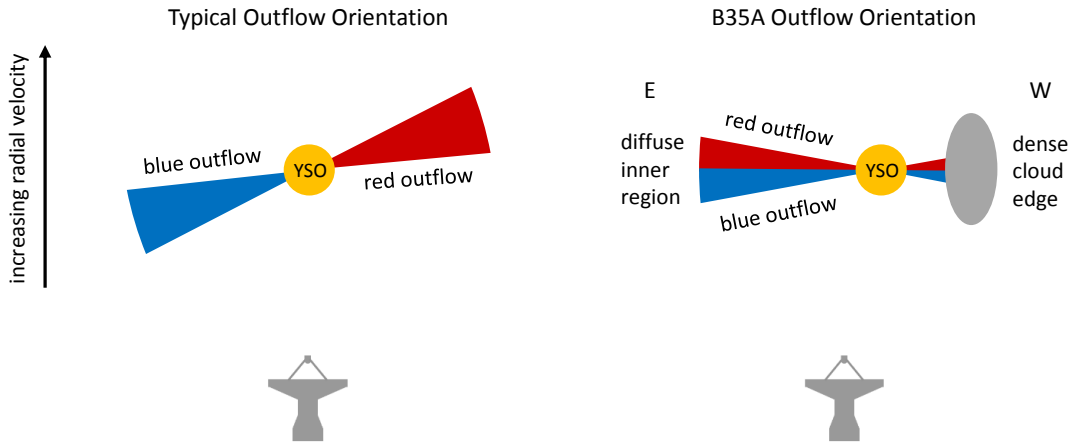

FIGURE 5.7. A diagram illustrating the orientations of bipolar outflows. Left: A commonly observed orientation, where the outflows lie at an angle to the plane of the sky. The resulting velocity maps show the red and blue lobes well separated spatially (e.g. Fig. 5.6). Right: The likely orientation in B35A, where red and blue shifted CO is seen in the same line-of-sight for both eastern and western outflows. The western outflow is truncated as it encounters the dense ridge of the the cloud. The eastern outflow extends further into the less dense central region of the cloud.

where T_0 (=hν/k$_B$) is 16.6 K (J = 3 → 2: ν = 345.8 GHz); T_{max} is the peak of the emission; and *const* (= T_0/(e$^{T_0/T_{bg}}$-1)) is 0.038 K, where T_{bg} = 2.73 K. The ^{12}CO column

density, $N(^{12}\mathrm{CO})$, of the optically thin outflowing gas is then determined using,

$$N(^{12}\mathrm{CO}) = \frac{3\mathrm{k_B}}{8\pi^3 \mathrm{B}_{12}\mu_{12}^2} \frac{\mathrm{e}^{\mathrm{hB}_{12}J(J+1)/\mathrm{k_B}T_{\mathrm{ex}}(^{12}\mathrm{CO})}}{J+1} \times \frac{\int T_{\mathrm{mb}} dv}{1-\mathrm{e}^{-T_0/T_{\mathrm{ex}}(^{12}\mathrm{CO})}} \ \mathrm{cm}^{-2}, \quad (5.2)$$

where $\int T_{\mathrm{mb}}\mathrm{dv}$ is the integrated intensity of the residual blue or red emission from 6.4 to 12.4 and 12.4 to 18.4 km s^{-1}, respectively. The rotation constant (B_{12}) and dipole moment (μ_{12}) are 57.636 GHz (Winnewisser et al., 1997) and 0.11011 D (Goorvitch, 1994), respectively. Similar equations are used by Pineda et al. (2008) for the $J = 1 \rightarrow 0$ transition. The mass in each pixel *(x,y)* is,

$$M(x,y) = N(^{12}\mathrm{CO})[\mathrm{H_2}/^{12}\mathrm{CO}]A(x,y)m \ \ \mathrm{M}_\odot, \quad (5.3)$$

where $[\mathrm{H_2}/^{12}\mathrm{CO}] = 1.0 \pm 0.5 \times 10^4$, *A(x,y)* is the pixel size and *m* = 2.2 $\mathrm{m_H}$ / $\mathrm{m}_\odot$ ($\mathrm{m_H}$ is the mass of a hydrogen atom and $\mathrm{m}_\odot$ is the solar mass). The total mass within the outflow can then be determined by summing the contribution (red and blue shifted) in all pixels i.e.

$$M_{\mathrm{total}} = \sum_{x=1}^{x_{\mathrm{tot}}} \sum_{y=1}^{y_{\mathrm{tot}}} (M_{\mathrm{red}} + M_{\mathrm{blue}}) \ \ \mathrm{M}_\odot. \quad (5.4)$$

The momentum *P*, kinetic energy E_{k} and mechanical luminosity L_{m} are determined by the moments,

$$P = \iiint M(v,x,y)\, v\, dv\, dx\, dy \ \ \mathrm{M}_\odot \ \mathrm{km\ s}^{-1}, \quad (5.5)$$

$$E_{\mathrm{k}} = \frac{1}{2} \iiint M(v,x,y)\, v^2\, dv\, dx\, dy \ \ \mathrm{M}_\odot \ \mathrm{km}^2\ \mathrm{s}^{-2}, \quad (5.6)$$

and

$$L_{\mathrm{m}} = \frac{1}{2R} \iiint M(v,x,y)\, v^3\, dv\, dx\, dy \ \ \mathrm{L}_\odot, \quad (5.7)$$

where *R* is the length of the outflow. The dynamical age of the outflow is simply,

$$\tau_{\mathrm{dyn}} = l/v \ \ \mathrm{yr}, \quad (5.8)$$

where *l* is the length of the outflow and v is the velocity of the gas. This can then be used to calculate the mass loss rate,

$$\dot{M} = \frac{M}{\tau_{\mathrm{dyn}}} \ \ \mathrm{M}_\odot \ \mathrm{yr}^{-1} \quad (5.9)$$

TABLE 5.2. Masses of red and blue-shifted material in four regions of the cloud (defined in Fig. 5.8). Masses are calculated after subtraction of a 'cloud Gaussian profile'. The mass uncertainties are dominated by the systematic error in the ^{12}CO:H_2 ratio ($\sim$50 per cent).

	$M_{\rm red}$ ($M_\odot$)	$M_{\rm blue}$ ($M_\odot$)	$M_{\rm red}$ (%)	$M_{\rm blue}$ (%)
Whole Cloud	0.14	0.60	19	81
YSO Region	0.06	0.37	14	86
Eastern Outflow	0.05	0.28	15	85
Western Outflow	0.01	0.09	10	90

and momentum loss rate,

$$\dot{P} = \frac{P}{\tau_{\rm dyn}} \ {\rm M}_\odot \ {\rm km\ s^{-1}\ yr^{-1}}. \tag{5.10}$$

Following the removal of a 'cloud Gaussian profile', the residual mass of the entire cloud is 0.74 $M_\odot$. Table 5.2 shows that for the whole cloud, the residual blue-shifted mass is greater than the red. However, a significant proportion of this residual mass (42 per cent) is found beyond the reach of the outflows and should not be considered in this analysis. A region encompassing only the YSO and outflow is defined in Fig. 5.8. As the outflow is oriented in the plane of the sky it is helpful to discuss the east and west components (described in Fig. 5.8 by a line perpendicular to the direction of the outflow). The eastern outflow (0.33 $M_\odot$) is more massive than the western outflow (0.10 $M_\odot$). The low mass of the western outflow can be explained by the YSO's proximity to the western edge of the cloud. The eastern jet entrains CO along its entire length, however, the western jet presumably extends through the edge of the cloud and therefore entrains CO along only half its length. Proportionally, the eastern outflow mass is 15 per cent red and 85 per cent blue. The western outflow is 10 per cent red and 90 per cent blue. The red percentage is slightly higher in the east than the west. This indicates that the outflow axis may be oriented very slightly backward to the east and forward to the west; however, for red- and blue-shifted emission to be detected in both outflows the inclination must be smaller than the estimated opening angle. Taking the diameter of the outflow at its widest part (Fig. 5.3: 10.75 – 11.00 km s^{-1}, $J = 3 \rightarrow 2$) and assuming the outflow is conical gives an opening angle of $\sim 20^\circ$.

Further physical characteristics of the outflows and a comparison with values determined by deV02 are shown in Table 5.3. It is found that the results depend strongly on how certain parameters are determined. A variety of methods are shown to illus-

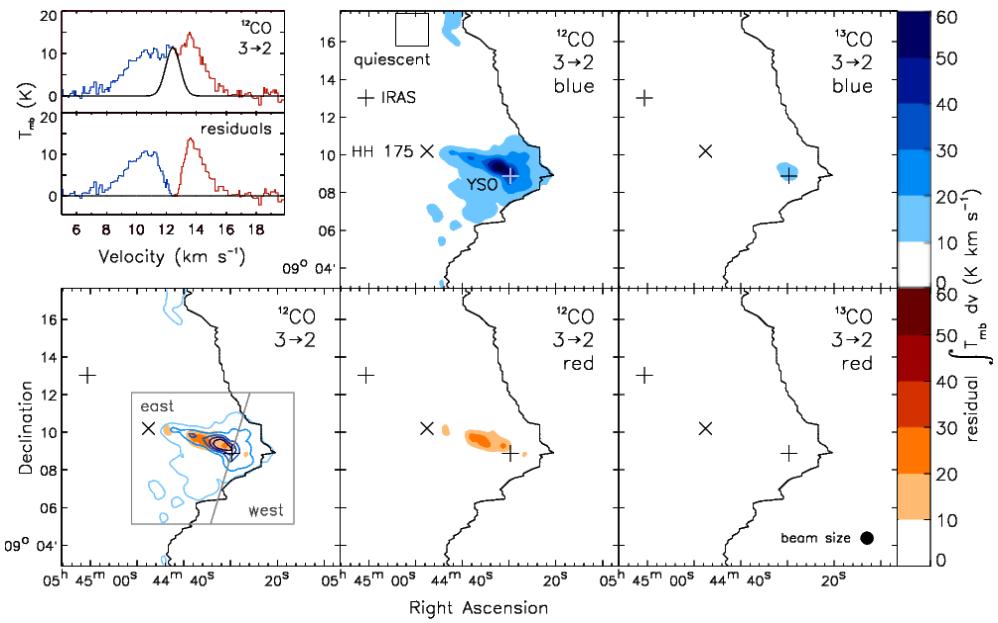

FIGURE 5.8. Top left: The upper spectrum shows the 'cloud Gaussian profile' scaled to the emission, where the velocity and FWHM of the profile are fixed. The profile is determined by fitting a Gaussian to the median emission in the region marked in the top centre panel. The lower spectrum shows the residual emission after the removal of this profile. Centre and right: ^{12}CO and ^{13}CO integrated intensity red- and blue-ward of the median cloud velocity after subtraction of a 'cloud Gaussian profile'. Bottom left: The YSO region is defined by the rectangle and divided into eastern and western sectors by a line perpendicular to the direction of the outflow. The outflow masses are shown in Table 5.2 and a detailed analysis of the outflow properties is presented in Table 5.3.

trate this. The mass, for example, can be determined using the integrated intensity of: the line-wing emission (deV02); or the residuals after a 'cloud Gaussian profile' has been subtracted (the preferred method for this work). The excitation temperature can be fixed at 30 K for the whole cloud (deV02); or calculated for each pixel (Eq. 3.2). The dynamical age of the outflow depends only on its length and velocity. However, the length inevitably depends on the s/n of the data as the intensity decreases towards the outflow's furthest extent. In addition, two methods can be used to determine the velocity. The maximum velocity difference between the peak emission and the linewings gives the velocity of the fastest material in the outflow (deV02). Alternatively, the velocity of the peak residual emission after a 'cloud Gaussian profile' has been subtracted gives the velocity of the majority of the outflowing mass.

Table 5.3 begins with parameters determined by analysing the spectra across the whole cloud. The first row shows the values calculated by deV02 using the $J = 1 \rightarrow 0$ tran-

sition of ^{12}CO. In the second row the same method is used to derive results from the JCMT data. The JCMT masses (0.9 and 1.5 $M_{\odot}$) are found to be slightly higher than calculated in deV02 (0.4 and 0.5 $M_{\odot}$). This may be due to the different transitions used. The JCMT red- and blue-shifted velocities in the eastern outflow are +6.0 and -7.5 km s^{-1} with respect to the cloud velocity. While these values are similar to the deV02 results, they fall short of the typical range. This is not surprising as the line-of-sight velocity component for jets oriented in the plane of the sky is bound to be small. The JCMT outflow lengths (0.3 and 0.4 pc) are shorter than found by deV02 (0.7 and 0.6 pc). This may be due to differing noise levels in the data.

While the JCMT outflow properties have been calculated using the same method as deV02 for comparison, more accurate values can be obtained without their assumptions since the cloud temperature is not uniformly 30 K. A good estimate of the outflow inclination to the line-of-sight along with the residual emission (after subtraction of a 'cloud Gaussian profile') is used to find the mass and velocity.

The subsequent four rows in Table 5.3 explore how the assumed excitation temperature affects the parameters using our method to determine the mass and velocity. Calculating the temperature of each pixel obviously produces the most accurate results, however the assumption of 30 K for the entire cloud does not make a large difference to the calculated parameters. Assuming a 10 or 5 K excitation temperature results in significantly higher mass estimates. The cloud temperature could therefore be approximated to 30 K, but the calculated temperature is used to improve the accuracy of the results.

As the line-of-sight outflow velocities are close to the cloud velocity, a region around the YSO has been selected (Fig. 5.8) to ensure that non-outflow blue and red shifted emission is not included in the mass determinations. The resulting parameters are shown in the next section of Table 5.3: 'YSO Region'. The 'red- and blue-shifted' values are compared to those found when the YSO region is divided into 'east and west' sectors. The red- and blue-shifted masses are much lower than those found using the spectra from whole cloud. This demonstrates that it is necessary to carefully define the affected region when investigating outflows aligned in the plane of the sky. This orientation means that an east-west analysis is more useful than the usual red-blue analysis to define the properties of the individual outflows. The table shows that the eastern outflow is twice as long as the western outflow; 0.4 and 0.2 pc respectively. The eastern outflow also has three times the mass of the western outflow; 0.3 and 0.1 $M_{\odot}$.

This is due to the location of the YSO at the western edge of the cloud.

Although the outflow masses and lengths are simple to calculate due to the orientation of the outflow, the velocities are vastly underestimated. To account for this, a trigonometric correction is used in the next section of the table: 'Sin(i) Correction', where i is the inclination to the line-of-sight. As the opening angle of the outflows is estimated to be $\sim 20°$and red- and blue-shifted emission is found in both, the inclination to the line-of-sight is likely to be between 80 and 89°. This correction has a negligible effect on the outflow length but significantly increases the velocities. These final two rows in the table provide the most reliable range of outflow parameters as the implications of the unusual orientation are fully taken into account when calculating the mass velocity and length.

Molecular outflows from low mass stars are typically 0.1 – 1 pc in length, with velocities of 10 – 100 km s^{-1} (Arce et al., 2007). The eastern and western outflows in B35A are found to be 0.4 and 0.2 pc long, respectively. The sin(i) correction results in eastern velocities of 14 to 143 km s^{-1} and western velocities of 18 to 182 km s^{-1}. Typically observed outflow momentum rates are 10^{-5} $M_\odot$ km s^{-1} yr^{-1} (Arce et al., 2007) and outflow mass fluxes of around 10^{-6} to 10^{-5} $M_\odot$ yr^{-1} (Bontemps et al., 1996) are common for low mass stars. Momentum rates of 2 to 28 $\times$ 10^{-5} $M_\odot$ km s^{-1} yr^{-1} and mass fluxes of 1 to 11 $\times$ 10^{-5} $M_\odot$ yr^{-1} are found in B35A, depending on the actual orientation of the outflows.

The total mass of the observed region is 28.6$\pm$14.3 $M_\odot$, however B35A extends much further to the east. At least one other YSO is present in the densest region of the cloud near the outflowing YSO (Table 4.1). It is possible that further star formation will take place elsewhere in the cloud, although much of the gas is heavily disrupted by the outflowing YSO.

TABLE 5.3. Physical characteristics of the outflows using a distance of 400pc to the cloud and the ^{12}CO $J = 3 \rightarrow 2$ transition. The total mass of the observed region, including the quiescent cloud and outflows, is 28.6 $\pm$14.3 $M_\odot$. The mass uncertainties are dominated by the systematic error in the ^{12}CO:H_2 ratio ($\sim$50 per cent). The velocity and length uncertainties are 0.15 km s^{-1} and 0.01 pc.

	M_{red}	M_{blue}	P_{red}	P_{blue}	$E_{k(red)}$	$E_{k(blue)}$	v_{red}	v_{blue}	l_{red}	l_{blue}
	($M_\odot$)		($M_\odot$ km s^{-1})		($M_\odot$ km^2 s^{-2})		(km s^{-1})		(pc)	
Whole Cloud										
de Vries et al., 2002	0.4	0.5	2.4	2.4	7.4	6.0	6.1	4.9	0.7	0.6
de Vries Method[a]	0.9	1.5	5.5	11.1	16.5	41.3	6.0	7.5	0.3	0.4
T_{ex} = Calculated	0.1	0.6	0.2	1.5	0.2	2.1	2.3	2.6	0.3	0.4
T_{ex} = 30 K	0.1	0.6	0.2	1.6	0.3	2.4	2.3	2.6	0.3	0.4
T_{ex} = 10 K	0.2	1.0	0.3	2.6	0.4	3.8	2.3	2.6	0.3	0.4
T_{ex} = 5 K	1.0	4.3	1.5	11.5	1.9	16.7	2.3	2.6	0.3	0.4
YSO Region[b]										
Red & Blue	0.1	0.4	0.1	1.0	0.1	1.3	2.6	2.5	0.3	0.4
East & West[c]	0.3	0.1	0.8	0.3	1.1	0.4	2.5	3.2	0.4	0.2
Sin(i) Correction[d]										
East & West[c] i=80°	0.3	0.1	0.8	0.3	1.2	0.4	14.4	18.3	0.4	0.2
East & West[c] i=89°	0.3	0.1	0.8	0.3	1.1	0.4	143.3	181.9	0.4	0.2

[a]These results use the method of de Vries et al. 2002: whole cloud T_{ex} = 30 K; outflow mass calculated by averaging the integrated intensities from 2 to 11 and 12 to 22 km s^{-1} over the spatial extent; P and E_k calculated using the total outflow masses and maximum velocities.
[b]The YSO region is shown in Fig. 5.8 and is comprised of the east and west regions.
[c]Read east and west in place of red and blue, respectively, for all parameters.
[d]A trigonometric correction is applied to the velocity and length assuming the outflow orientation is 89 or 80°to the line-of-sight.

TABLE 5.3 CONTINUED. Physical characteristics of the outflows using a distance of 400pc to the cloud and the ^{12}CO $J = 3 \rightarrow 2$ transition. The total mass of the observed region, including the quiescent cloud and outflows, is 28.6 $\pm$14.3 $M_\odot$. The mass uncertainties are dominated by the systematic error in the ^{12}CO:H_2 ratio ($\sim$50 per cent). The velocity and length uncertainties are 0.15 km s^{-1} and 0.01 pc.

	$\tau_{\rm dyn(red)}$	$\tau_{\rm dyn(blue)}$	$\dot{M}_{\rm red}$	$\dot{M}_{\rm blue}$	$\dot{P}_{\rm red}$	$\dot{P}_{\rm blue}$	$L_{\rm red}$	$L_{\rm blue}$
	(10^5 yr)		(10^{-6} $M_\odot$ yr^{-1})		(10^{-6} $M_\odot$ km s^{-1} yr^{-1})		(10^{-4} $L_\odot$)	
Whole Cloud								
de Vries et al., 2002	0.37	0.39	11.	13.	65.	63.	330.	250.
de Vries Method[a]	0.47	0.57	2.9	10.5	118.6	195.2	579.5	1196.5
$T_{\rm ex}$ = Calculated	1.21	1.61	1.1	3.7	1.5	9.6	2.7	21.7
$T_{\rm ex}$ = 30 K	1.21	1.61	1.2	3.8	1.8	10.1	3.7	24.2
$T_{\rm ex}$ = 10 K	1.21	1.61	1.0	3.5	1.6	9.2	3.1	21.0
$T_{\rm ex}$ = 5 K	1.21	1.61	8.6	26.9	12.6	71.1	25.7	169.8
YSO Region[b]								
Red & Blue	1.06	1.72	0.6	2.1	0.9	5.6	1.7	12.4
East & West[c]	1.69	0.64	2.0	1.6	4.9	4.0	10.9	9.4
Sin(i) Correction[d]								
East & West[c] i=80°	0.29	0.11	11.3	23.4	28.5	23.4	64.8	55.6
East & West[c] i=89°	0.03	0.01	112.0	89.3	279.3	229.2	625.1	536.6

[a]These results use the method of de Vries et al. 2002: whole cloud $T_{\rm ex}$ = 30 K; outflow mass calculated by averaging the integrated intensities from 2 to 11 and 12 to 22 km s^{-1} over the spatial extent; P and $E_{\rm k}$ calculated using the total outflow masses and maximum velocities.
[b]The YSO region is shown in Fig. 5.8 and is comprised of the east and west regions.
[c]Read east and west in place of red and blue, respectively, for all parameters.
[d]A trigonometric correction is applied to the velocity and length assuming the outflow orientation is 89 or 80°to the line-of-sight.

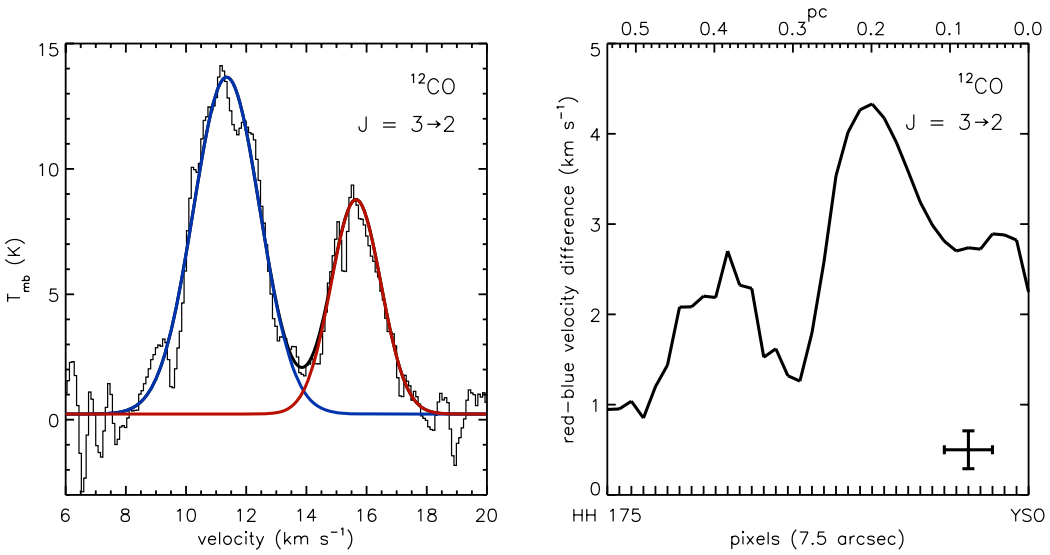

FIGURE 5.9. Left: Spectrum showing red and blue components within the outflow. Right: Difference between red and blue velocity components along the outflow. The position–velocity spur structure, where the velocity increases rapidly towards the position of the internal and leading bow shocks, closely resembles that of the jet-driven bow shock model (Arce et al., 2007).

5.3.3 MODELS

The left panel in Fig. 5.9 shows a typical spectrum from the IRAS 05417+0907 eastern outflow with Gaussian profiles fitted to the red and blue emission. To make full use of the small line-of-sight velocity component, the blue peak velocity is subtracted from the red peak velocity. The resulting velocity for this pixel and 35 others along the outflow are plotted in the right panel of Fig. 5.9. It is reasonable to assume that the perpendicular velocity component varies with the line-of-sight component. The distinctive jagged spur structure of the jet-driven bow shock model is clearly evident. A visual analysis of the outflow (e.g. Fig. 5.5) agrees with this model, where a collimated jet extends into the quiescent cloud producing a thin outflow shell around the jet (Masson & Chernin, 1993; Raga & Cabrit, 1993). Episodic variations in the mass-loss rate have lead to the double-spur structure seen in the position–velocity diagram. A similar analysis of the temperature was not possible due to the significant heating in the bright-rim of B35A, where the YSO is situated. Interferometric observations would provide the spatial resolution required for comparison to the models.

5.4 CLUMPS

An arc of clumps of enhanced emission are evident equidistant from the YSO. Rectangular regions around the clumps were selected by eye based on their appearance in the ^{12}CO ($J = 3 \rightarrow 2$) 12.25 to 13.5 km s^{-1} channel maps (see Fig. 5.3). The emission was integrated over 12 – 15 km s^{-1} and all pixels with less than 11 K km s^{-1} were discarded from the clump regions. A nearby similar sized region (0.23 $\times$ 0.23 pc) was defined for comparison. The integrated intensity over the same range in this region is less than 9 K km s^{-1} in every pixel. The resulting clump outlines are shown in Fig. 5.10. Clump 4 has a square north-western boundary where it merges with a denser region of the cloud. It is not possible to better define this edge so the derived properties of this clump are estimates. As the clumps are not observed in the ^{13}CO maps, the ^{12}CO emission can be assumed to be optically thin. Temperatures, column densities and masses are determined using equations 5.1 to 5.3.

Clump 4 lies directly ahead of HH 175, suggesting that the enhanced emission may be due to photo-desorption of CO ice from the surface of dust grains, induced by the UV radiation produced in the HH shock. Extrapolating this theory to explain the arc of clumps suggests that the outflows are precessing. Although clump 1 may simply be part of the dense cloud edge, clumps 2 – 4 indicate that the jet has moved through at least 45°in the plane of the sky.

Fig. 5.10 and Table 5.4 show that the maximum ^{12}CO column densities in the clumps (4.9 $\pm$ 0.5 to 6.2 $\pm$ 0.6 $\times$ 10^{15} cm^{-2}) are higher than the quiescent region (2.7 $\pm$ 0.3 $\times$ 10^{15} cm^{-2}). These values are 2 – 3 orders of magnitude lower than those found by Viti et al. (2006) for clumps ahead of HH objects ($\sim$3 $\times$ 10^{17} – 3 $\times$ 10^{18} cm^{-2}). As the B35A clumps are evident only at higher velocities, they may be located near the far surface of the cloud. This could account for the relatively low column density. The maximum ^{12}CO column density for the entire cloud is 1.2 $\times$ 10^{18} near the position of the YSO (see Fig. 4.3).

The clump masses are 1.4 $\pm$ 0.7 to 4.2 $\pm$ 2.1 $\times$ 10^{-2} M$_{\odot}$ but as the clumps have a range of sizes a more effective comparison can be made using the mass per parsec^2. These values are 7.1 $\pm$ 3.5 to 7.5 $\pm$ 3.7 $\times$ 10^{-1} M$_{\odot}$ / pc^2 for the clumps and 4.2 $\pm$ 2.1 $\times$ 10^{-1} M$_{\odot}$ / pc^2 for the quiescent region. The mass errors are due to the uncertainty in the N(H$_2$):N(^{12}CO) ratio so changing this value scales all the results in the same direction. The clumps therefore have a significantly higher mass per

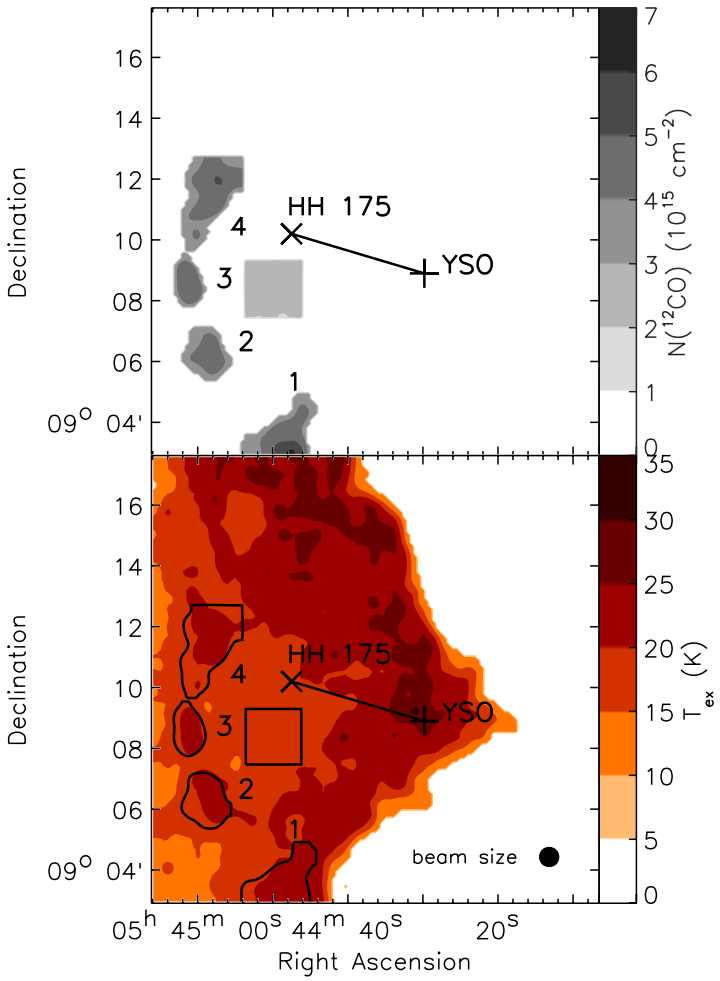

FIGURE 5.10. The upper map shows that the ^{12}CO column density of the clumps (across 12.0 – 15.0 km s^{-1}) is higher than that of the nearby quiescent region (square). The column density of the rest of the cloud is not shown. The lower map shows that the clump temperature is slightly higher than the quiescent region, more similar to the warm cloud edge.

parsec^2 than the quiescent region. These masses and column densities are consistent with a precessing outflow sweeping clean a segment of the cloud (where the quiescent region lies) and causing CO photo-desorption ahead of a series of HH objects (which are now extinct).

A visual analysis of the channel maps in Fig. 5.3 shows that the quiescent region has emission across most of the cloud's velocity range (10.50 – 13.25 km s^{-1}). The clumps, however, are only evident in the higher velocity channel maps (12.00 – 13.50 km s^{-1}). This suggests that these clumps of enhanced emission were produced when the eastern outflow was oriented, to a small degree, away from the observer during its precession.

Clumps of enhanced emission are not expected to have a higher temperature than their surroundings. The clump peak temperatures range from 22 $\pm$ 1 to 26 $\pm$ 1 K, greater than the quiescent region (19 $\pm$ 1 K), but still falling broadly within the expected range of 10 – 25 K (Viti et al., 2006). The clumps are slightly warmer than the CO sublimation temperature ($\sim$20 K (Sandford & Allamandola, 1988)), so CO ice is leaving the surface of the dust grains. Although the third dimension of this cloud cannot be viewed, it is possible that the clumps lie at a slightly greater line-of-sight distance than the majority of the cloud (as they are evident only at higher velocities). If this is the case, then the clumps may be exposed to the same UV flux from nearby O8III star λ Ori that causes heating in the western edge of the cloud (see Fig. 5.10). This may explain why the clumps have a similar temperature to the warm cloud edge.

The upper panel of Fig. 5.11 is a 93.9 $\times$ 93.9 arcmin 12 μm image from the Wide-field Infrared Survey Explorer (*WISE*) which traces warm gas and shows B35A in a wider context. The 12 μm emission extends well beyond the CO survey area (black box) to the east and the arc of clumps is a dominant feature at this wavelength. The lower panel of this figure shows the outlines of the CO clumps overlaid on the 12 μm emission. The arcs match well, indicating that both gas and dust are warm at these locations.

Terquem et al. (1999) show that outflow precession may be due to a non-coplanar binary companion. As jets are driven from the circumstellar disk, any tidal interaction between misaligned disks will induce precession of the disk and also the jet. The outflowing YSO in B35A is known to have a companion. It is not resolved in the CO observations as they are separated by only 1.21 arcsec (Connelley et al., 2008). This translates to 484 AU, although the actual separation may be greater depending on their relative distance in the line-of-sight. No data is available on the mass of the secondary, but it appears that the outflowing YSO is the more massive of the two. A rough estimate of the orbital period (T) can be made using,

$$T = \sqrt{\frac{separation}{m_1 + m_2}} \text{ yr.} \tag{5.11}$$

Assuming the mass of the secondary is equal to that of the primary, m_1 and m_2 = 1.15 $M_\odot$ (Morgan et al., 2008), gives an orbital period of 7,012 years. This is a lower limit as the secondary is less massive than the primary and the separation may greater than 484 AU. The orbital period is therefore much longer than the calculated dynamical age of the outflow (3,000 – 29,000 years), suggesting that the jet

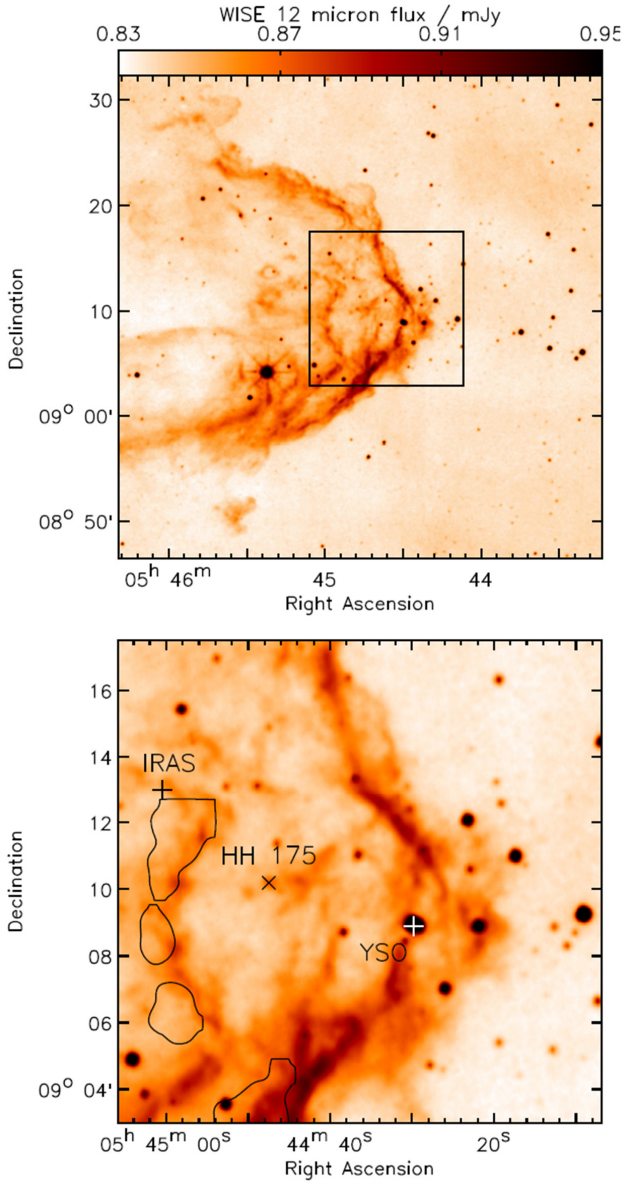

FIGURE 5.11. The upper map shows a *WISE* 12 μm 93.9 × 93.9 arcmin (10.9 × 10.9 pc) region centred on B35A. This 12 μm emission traces warm dust, YSO envelopes and disks. The black square and the lower map show the CO survey area. The CO clump outlines are overlaid and match the arc of enhanced emission, which is clearly visible at this wavelength.

has not yet completed a full precession.

Clumps of enhanced emission ahead of HH objects are continuously evolving transient phenomena. However, the slow precession of this outflow means that clumps with a range of ages are present. This cloud is therefore an excellent candidate for studying the evolving chemistry in post HH object clumps.

TABLE 5.4. Properties of clumps selected by eye in the ^{12}CO $J = 3 \rightarrow 2$ transition. Propagation of observational errors gives a statistical error of 10 per cent. The mass uncertainties are dominated by the systematic error in the ^{12}CO:H_2 ratio ($\sim$50 per cent).

Region	$d_{\text{YSO-Region}}$ (pc)	$N(^{12}\text{CO})$ (10^{15} cm^{-2})	M (10^{-2} M$_\odot$)	M / A (10^{-1} M$_\odot$ pc^{-2})	T_{ex} (K)	v (km s^{-1})
Clump 1	0.86 ± 0.04	6.2 ± 0.6	3.0 ± 1.5	7.5 ± 3.7	25 ± 1	12.00 – 13.50
Clump 2	0.87 ± 0.04	4.9 ± 0.5	2.1 ± 1.0	7.1 ± 3.5	23 ± 1	12.00 – 13.50
Clump 3	0.90 ± 0.04	4.9 ± 0.5	1.4 ± 0.7	7.4 ± 3.7	24 ± 1	12.00 – 13.50
Clump 4	0.86 ± 0.04	5.1 ± 0.5	4.2 ± 2.1	7.3 ± 3.6	25 ± 1	12.00 – 13.50
Quiescent	0.48 ± 0.04	2.7 ± 0.3	2.1 ± 1.1	4.2 ± 2.1	19 ± 1	10.50 – 13.25

5.5 SUMMARY AND CONCLUSIONS

This chapter explored the theory that a precessing outflow, originating from YSO IRAS 05417+0907, influences the morphology and kinematics of B35A. Observations of three isotopologues and two transitions of CO (^{12}CO, ^{13}CO and C^{18}O; $J = 3\rightarrow2$ and $J = 2\rightarrow1$) across a 1.7 $\times$1.7 pc region of B35A were used to investigate the impact of this unusual outflow on the cloud.

The cloud velocity was found to be 12.42 km s^{-1}, by averaging the peak velocities of the two transitions of ^{12}CO in a quiescent region of the cloud. The emission in the YSO region is broad ($\sim$3 km s^{-1}, three times the width of the quiescent region) with both red- and blue-shifted components evident in the eastern outflow. This is unusual and indicates that the outflows are oriented perpendicular to the line-of-sight and the presence of red and blue emission in one outflow is due to its opening angle. Relatively low intensity emission in the region of the HH object ($\sim$11 K, half the intensity of the quiescent region) suggests that the CO molecules may have been dissociated by the shock or the local UV radiation field. Observations of enhanced C I would confirm this.

Channel maps show the CO gas entrained by the jet extending from the YSO towards the HH object at red and blue-shifted velocities (13.25 – 13.75 and 10.25 – 10.75 km s^{-1}, respectively). The co-location of these red and blue-shifted structures with typical collimated morphologies provides further evidence for the outflow orientation in the plane of the sky. The outflow is estimated to lie at 80 – 89°to the line-of-sight with an opening angle of $\sim$20°. The channel maps clearly show a triangular hole extending to the southeast of the YSO and terminating with an arc of clumps spanning $\sim$45°. This morphology suggests that the gas has been swept out by the eastern jet, implying that it is precessing.

Velocity maps show a protrusion in the western edge of the cloud with the same velocity as the eastern outflow. As the outflows are oriented in the plane of the sky, the eastern and western outflows will have very similar line-of-sight velocities. This suggests that the protrusion is caused by the western jet entraining gas as it ploughs through the dense ridge at the cloud edge.

Variations in velocity along the eastern outflow, along with the collimated structure seen in the channel maps indicate that the jet-driven bow shock model is the best description of this outflow.

The eastern outflow is found to have typical properties: a mass of 0.3 $M_{\odot}$; a length of 0.4 pc and a velocity of 14 – 143 km s^{-1}, which result in a dynamical age of 3,000 – 29,000 years. Although similar velocities (18 – 182 km s^{-1}) are found in the western outflow, it is much shorter (0.2 pc) and less massive (0.1 $M_{\odot}$) due to the YSO's location at the western edge of the cloud.

A clump of enhanced CO emission is found ahead of HH 175. This may be caused by photo-desorption of CO ice from dust grains by the UV radiation produced in the shock. An arc of several similar clumps bordering an empty segment in the high velocity (13.0 – 13.5 km s^{-1}) channel maps suggest that the outflow has undergone a significant precession, sweeping out a region of at least 45°in the plane of the sky. The clumps have excitation temperatures of 23 – 25 K and masses of 0.01 – 0.04 $M_{\odot}$. The precession may be induced by tidal interactions as the YSO is in a close binary system with an orbital period estimated at over 7,012 years.

This is cloud an excellent candidate for studying the evolving chemistry in post HH object clumps. Interferometric observations are required to fully understand the interactions of the outflow with the cloud on a smaller scale. Further observations of molecules such as HCO^{+}, which are known to be enhanced in post HH object clumps, will help constrain their chemical and physical nature.

REFERENCES

Arce H. G., Goodman A. A., 2001a, ApJ, 554, 132 107

Arce H. G., Goodman A. A., 2001b, ApJL, 551, L171 107

Arce H. G., Shepherd D., Gueth F., Lee C., Bachiller R., Rosen A., Beuther H., 2007, in B. Reipurth, D. Jewitt, & K. Keil ed., Protostars and Planets V Molecular Outflows in Low- and High-Mass Star-forming Regions. pp 245–260 118, 125, 128

Bontemps S., Andre P., Terebey S., Cabrit S., 1996, A&A, 311, 858 125

Bussmann R. S., Wong T. W., Hedden A. S., Kulesa C. A., Walker C. K., 2007, ApJL, 657, L33 107

Claussen M. J., Wilking B. A., Benson P. J., Wootten A., Myers P. C., Terebey S., 1996, ApJS, 106, 111 116

Connelley M. S., Reipurth B., Tokunaga A. T., 2008, AJ, 135, 2496 107, 131

Davis C. J., Dent W. R. F., Matthews H. E., Coulson I. M., McCaughrean M. J., 2000, MNRAS, 318, 952 107

De Vries C. H., Narayanan G., Snell R. L., 2002, ApJ, 577, 798 109

Eisloffel J., Smith M. D., Davis C. J., Ray T. P., 1996, AJ, 112, 2086 108

Girart J. M., Rodriguez L. F., Anglada G., Estalella R., Torrelles J. M., Marti J., Pena M., Ayala S., Curiel S., Noriega-Crespo A., 1994, ApJL, 435, L145 108

Goodman A. A., Benson P. J., Fuller G. A., Myers P. C., 1993, ApJ, 406, 528 113

Goorvitch D., 1994, ApJS, 95, 535 121

Gueth F., Guilloteau S., Bachiller R., 1996, A&A, 307, 891 108

Gueth F., Guilloteau S., Bachiller R., 1998, A&A, 333, 287 107, 108

Hatchell J., Fuller G. A., Ladd E. F., 1999, A&A, 344, 687 107

Hatchell J., Fuller G. A., Richer J. S., 2007, A&A, 472, 187 107

Jørgensen J. K., Hogerheijde M. R., Blake G. A., van Dishoeck E. F., Mundy L. G., Schöier F. L., 2004, A&A, 415, 1021 108

Klaassen P. D., Mottram J. C., Maud L. T., Juhasz A., 2016, MNRAS, 460, 627 107

Knee L. B. G., Sandell G., 2000, A&A, 361, 671 107

Lee C., Ho P. T. P., Palau A., Hirano N., Bourke T. L., Shang H., Zhang Q., 2007, ApJ, 670, 1188 107

Li B., Pei C.-C., Ma H.-J., 2007, Chinese Astronomy and Astrophysics, 31, 372 116

Lommen D., Jørgensen J. K., van Dishoeck E. F., Crapsi A., 2008, A&A, 481, 141 109

Maddalena R. J., Morris M., Moscowitz J., Thaddeus P., 1986, ApJ, 303, 375 116

Masson C. R., Chernin L. M., 1993, ApJ, 414, 230 128

Morgan L. K., Thompson M. A., Urquhart J. S., White G. J., 2008, A&A, 477, 557 131

Myers P. C., Heyer M., Snell R. L., Goldsmith P. F., 1988, ApJ, 324, 907 107, 110

Olmi L., Testi L., 2002, A&A, 392, 1053 113

Parise B., Belloche A., Leurini S., Schilke P., Wyrowski F., Güsten R., 2006, A&A, 454, L79 120

Pineda J. E., Caselli P., Goodman A. A., 2008, ApJ, 679, 481 121

Raga A., Cabrit S., 1993, A&A, 278, 267 128

Sandford S. A., Allamandola L. J., 1988, Icarus, 76, 201 131

Terquem C., Eislöffel J., Papaloizou J. C. B., Nelson R. P., 1999, ApJL, 512, L131 131

van Kempen T. A., van Dishoeck E. F., Güsten R., Kristensen L. E., Schilke P., Hogerheijde M. R., Boland W., Nefs B., Menten K. M., Baryshev A., Wyrowski F., 2009, A&A, 501, 633 107, 109

Viti S., Girart J. M., Hatchell J., 2006, A&A, 449, 1089 108, 129, 131

Winnewisser G., Belov S., Klaus T., Schieder R., 1997, Journal of Molecular Spectroscopy, 184, 468 121

Yeh S. C. C., Hirano N., Bourke T. L., Ho P. T. P., Lee C., Ohashi N., Takakuwa S., 2008, ApJ, 675, 454 107

CHAPTER 6

CONCLUSIONS AND FURTHER WORK

SYNOPSIS

This thesis is an integral part of the 'gas-solid mapping project', which aims to better understand the early stages of star and planet formation by defining the physical and chemical conditions in a sample of starless and star forming clouds.

Three key questions were addressed by the work presented in this thesis:

- *How is CO gas distributed?*
- *What are the temperature and density structures?*
- *How are the morphology and kinematics of CO gas influenced by embedded and nearby stars?*

CO observations were made of nine starless and star forming molecular clouds. A suite of software, COROLINE, was written to analyse the data and constrain the physical parameters of clouds. Particular emphasis was placed on B35A, a bright-rimmed cloud with an outflowing YSO which has a significant influence on the morphology and kinematics of the gas.

This chapter summarises the main results and presents the first combined gas-solid maps of a molecular cloud. Future work that would provide further insights into the interactions between the gas and solid constituents of molecular clouds is proposed.

6.1 SUMMARY OF OBSERVATIONS AND ANALYSIS

A total of 206 hours of observing time were awarded to the author to make high resolution, large scale maps of CO gas in a sample of starless and star forming molecular clouds. The observations were conducted over six observing runs at three world-class telescopes. The author became familiar with their operating procedures and is now considered an experienced observer.

Analysis software written in the course of this PhD to analyse the resulting large dataset produces temperature, density and velocity maps of the clouds. This COROLINE software is available for analysis of the remaining CO data and any subsequent CO observations.

6.2 CONCLUSIONS

This thesis focused in particular on molecular cloud B35A: a bright-rimmed cloud containing several embedded YSOs, one with a bipolar outflow resulting in an HH-object. The observations presented in Chapter 4 constitute the first large scale (14.6×14.6 arcmin) multi-transition ($J = 3 \rightarrow 2$ and $J = 2 \rightarrow 1$) survey of three CO isotopologues (^{12}CO, ^{13}CO and C^{18}O) in B35A.

The major results of this chapter are:

- The first observational evidence for a correlation between the intensity of the PAH emission near 8 μm and gas excitation temperature.
- The offset between the maxima of PAH and ^{12}CO emission in PDRs is found to depend on the enhanced UV flux, G_0.

Chapter 5 explored the theory that an outflow, originating from YSO IRAS 05417+0907, influences the morphology and kinematics of B35A.

The major results of this chapter are:

- The outflows in B35A are oriented perpendicular to the line-of-sight.
- Low intensity emission in the region of the HH object suggests that the CO molecules may have been dissociated by the shock or local UV radiation field.

- Enhanced CO emission found ahead of HH 175 may be caused by photo-desorption of CO ice from dust grains by UV radiation produced in the shock.
- An arc of several clumps of enhanced emission bordering an empty segment in the high velocity channel maps suggest that the outflow has undergone a significant precession.

Analysis of the CO gas kinematics and excitation temperatures has shown that embedded YSOs and nearby massive stars can dramatically affect the temperature, density and velocity of the gas. A detailed understanding the physical parameters of the star forming clouds is therefore critical to the wider gas-solid mapping project.

6.3 FURTHER WORK

Potential areas of further work to complement and extend the work presented in this thesis are proposed in this section.

6.3.1 MOLECULAR CLOUD OBSERVATIONS

High resolution ALMA imaging (such as in Friesen et al. (2014)) may be required to confirm the 'starless' designation of several clouds in the gas-solid mapping project. Condensations in high extinction environments may harbour young, low mass protostars.

ALMA CO observations of turbulent regions of the molecular clouds would reveal the gas kinematics on a much smaller scale. This would better constrain the influence of bipolar jets on the surrounding gas.

The Mid-InfraRed Instrument (MIRI) on the James Webb Space Telescope (JWST) heralds a new era of infrared astronomy. Due for launch in 2018, JWST will provide unparallelled spectral sensitivity and resolution between 5 and 28 μm (Wright et al., 2004). It will be sensitive enough to observe ice species other than water and may provide direct detections of complex organic molecules in protoplanetary disks for the first time.

6.3.2 BARNARD 35A

PDR codes and maps of similar coverage of B35A in the main cooling lines C II at 157 μm and O I at 63 and 145 μm would help to understand the shape of the correlation between the intensity of the PAH emission and gas excitation temperature and its relationship with the PAH heating efficiency. In particular, fine structure line ratios will better constrain the UV enhancement G_0 and gas density. A survey of similarly oriented PDRs (i.e. IC 63, Thi et al. (2009)) would determine whether other PDRs also show two distinct regimes with comparable δT/δ(8 μm flux).

Further interferometric observations of CO and PAHs in PDRs with similar hydrogen densities (10^4 cm^{-3}) would better define the relationship between the offset and G_0.

B35A is an excellent candidate for studying the evolving chemistry in post HH object clumps. Interferometric observations are required to fully understand the interactions of the outflow with the cloud on a smaller scale. Further observations of molecules such as HCO^+, which are known to be enhanced in post HH object clumps, will help constrain their chemical and physical nature. Observations of enhanced C I would also confirm whether CO molecules have been dissociated in the HH object shock.

6.3.3 COROLINE SOFTWARE

The COroline software described in Chapter 3 can be extended to incorporate the data reduction steps outlined in Section 3.1 which currently must be done manually. Automating this will make the software significantly more user friendly, producing CO emission maps with minimal user interaction. The addition of a Graphical User Interface (GUI) would improve accessibility for inexperienced IDL users, allowing the software to be used by a wider audience. The user could select the cloud and CO transition and the software would import the relevant observation files. The full analysis would then be performed and all maps described in Section 3.3 would be saved to a user-specified directory. Alternatively, the GUI could be used to select, for example, a subsection of the map or spectrum for analysis.

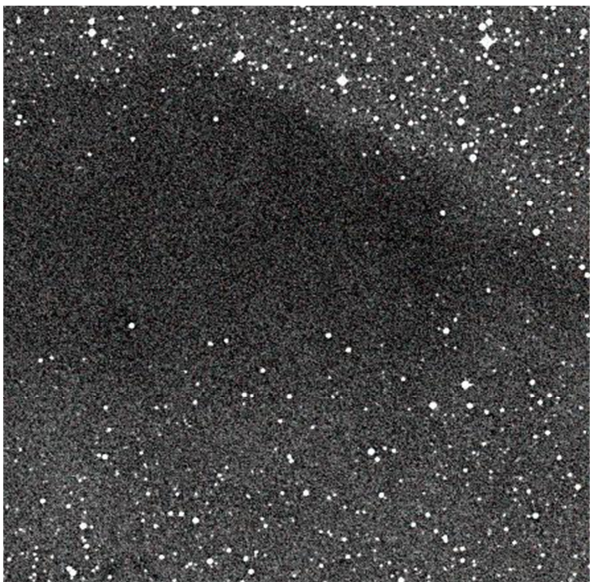

FIGURE 6.1. Visible wavelength Hubble Space Telescope image of molecular cloud L158 obscuring the light from background stars.

6.3.4 CO MAPS

The aim of the CO gas mapping project is to produce column density, temperature and velocity channel maps for all nine molecular clouds. The extent of analysis required for each cloud will depend on the of complexity of its gas structure. Star forming clouds and those near massive stars are likely to exhibit more complicated features than starless clouds.

L158 (shown in Fig. 6.1) is a starless cloud at a distance of 165 pc in Ophiuchus (Chini, 1981), receding at a velocity of 4.3 km s^{-1}. Visser et al. (2002) observed it as part of a SCUBA survey of Lynds dark clouds. They found its peak density, n(H_2), is 8 $\times$ 10^{11} m^{-3} and its total mass is 9.5 M$\odot$. The integrated emission in the ^{12}CO $J = 3 \rightarrow 2$ and ^{13}CO $J = 3 \rightarrow 2$ channel maps in Fig. 6.2 confirm that L158 is quiescent, with a recession velocity of 3.0 – 4.5 km s^{-1}.

6.3.5 COMBINED GAS-ICE MAPS

The goal of the gas-solid mapping project is to combine gas and ice maps for several starless and star forming molecular clouds. The first combined gas-ice map is presented in Fig. 6.3 for B35A (Jennifer Noble, *private communication*). The H_2O ice

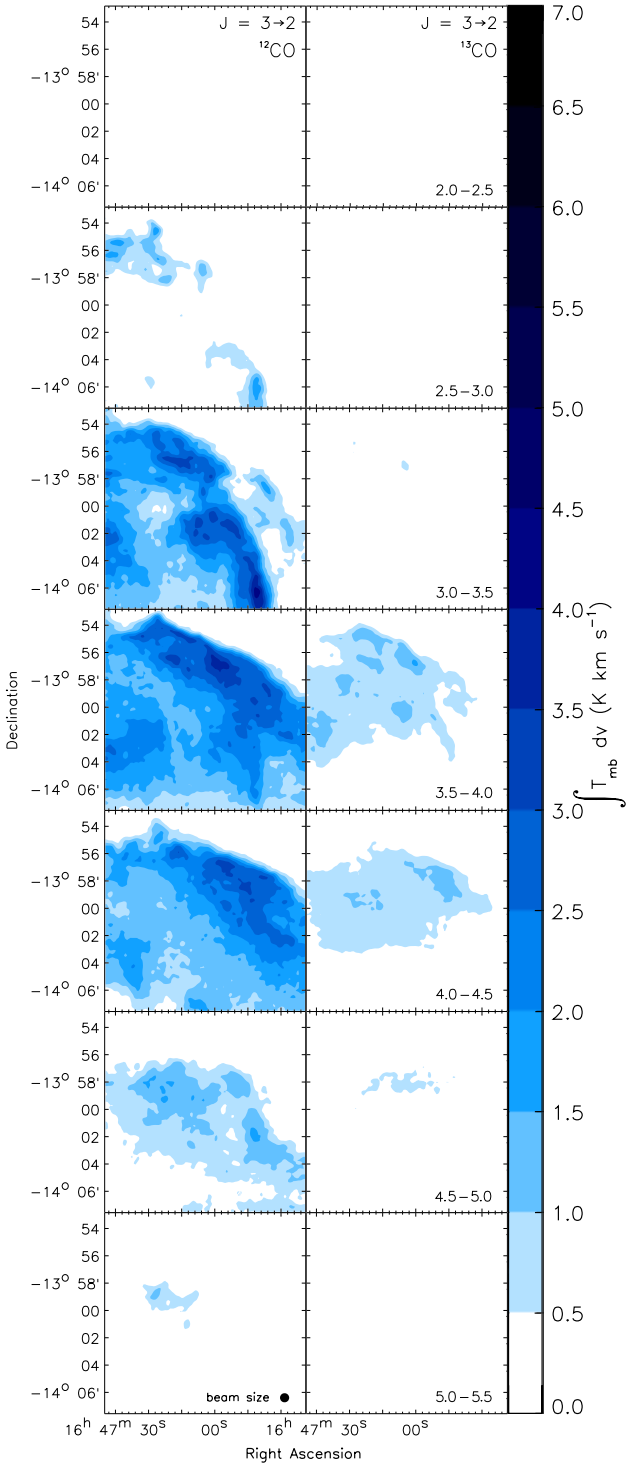

FIGURE 6.2. From left: channel maps of L158 in ^{12}CO 3→2 and ^{13}CO 3→2. Integrated emission from 2.0 to 5.5 km s^{-1} in channels of 0.5 km s^{-1}. The cloud appears to be quiescent with no embedded molecular outflows.

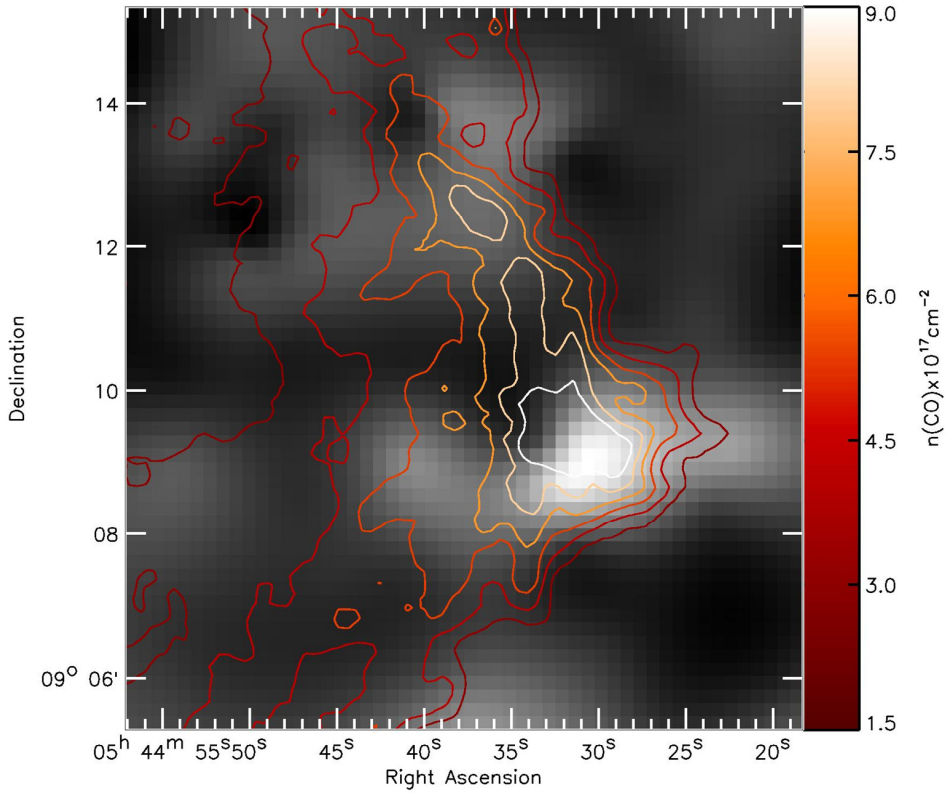

FIGURE 6.3. The first combined gas-ice map of B35A. H_2O ice abundance, n(H_2O), is shown in greyscale (scale runs from 0.4 – 5.2 $\times$ 10^{18} cm^{-2}). The gas map (red contours) is derived from the CO $J = 2 \rightarrow 1$ observations. Ice map from Jennifer Noble (*private communication*).

abundance map was produced from the *AKARI* 9.5 $\times$ 10 arcmin NP data using the ARF pipeline, originally written for analysing the *AKARI* 1 $\times$ 1 arcmin NG fields of view (Noble et al., 2013). It has been convolved to the separation of the two closest sources in the field of view. The gas-phase ^{12}CO column density, derived from the $J = 2 \rightarrow 1$ observations and analysis described in Chapters 2 and 3, is overlaid in shades of red. The regions of highest CO gas and H_2O ice abundance coincide at the densest region of the cloud, where the YSO is located.

Fig. 6.4 is the result of the most recent analysis of the *AKARI* 9.5 $\times$ 10 arcmin NP data for B35A, using the ARF2 pipeline (Suutarinen, 2015). It shows the column density of H_2O ice towards several background sources in the form of a bubble plot (Aleksi Suutarinen, *private communication*). This is an effective way of displaying the sparse, non-uniformly distributed data. Dark blue circles are centred on the observed background sources and their diameters indicate the detected column density. Light blue circles show the associated uncertainties and red dots depict non-detections from which it was possible to extract only upper limits from the observations. Blue dots

show the locations of background sources where the spectra did not contain enough points around the 3 μm feature, making baseline fitting impossible and optical depth estimates unobtainable. No conclusions can be drawn about the column densities of H_2O ice in these locations. The column density of gas-phase ^{12}CO calculated via the $J = 3 \rightarrow 2$ transition using the COROLINE software is shown in purple. To give context to these plots, they are overlaid on a variety of archival *Spitzer* and *Herschel* images. *Herschel* SPIRE 250 μm data is commonly used to trace cold dust and, as discussed in Chapter 4, the *Spitzer* IRAC 8 μm map traces PAHs. The *WISE* 3.4 μm map also traces PAHs and the *WISE* 12 μm map (as used in Fig. 5.11) traces warm dust, YSO envelopes and disks. Although the uncertainty in the H_2O column densities is of the order of ∼50 per cent, mainly due to incomplete calibration data, correlations are possible. The H_2O ice column density peaks at 2.96×10^{18} cm^{-2} in the region of the YSO where the CO gas column density is also at its maximum. Its abundance drops significantly outside this region, with column densities at least three times lower along ten other lines of sight and non-detections in nine further locations. H_2O ice is seen both inside the cloud and outside beyond the cloud's bright rim, where the cloud edge is defined by the 5σ detection of ^{12}CO gas (Fig. 4.1).

The CO_2 ice absorption feature at 4.3 μm, while strongly detected in certain lines of sight (e.g. Fig 2.2), was found in very few of the *AKARI* spectra (Aleksi Suutarinen, *private communication*). It was therefore not possible to produce useful maps of the CO_2 ice distribution for any of the gas-solid mapping project clouds. However, a correlation was found between detections of CO_2 ice and the presence of the H_2O ice feature.

6.4 A FUTURE PHD PROGRAMME

The large number of CO gas observations and the COROLINE software could form the basis of a PhD programme. Maps of CO gas distribution and physical parameters are to be produced for the remaining data and combined with the existing ice maps of the same clouds. This will allow an exploration of the relationships between density, temperature, gas and ice abundance across a variety of starless and star forming clouds.

The work could be expanded in a variety of directions, such as further observations to investigate the abundance, morphology and kinematics of gas and ice at higher resolution using ALMA and JWST. Alternatively, the combined gas-solid maps could

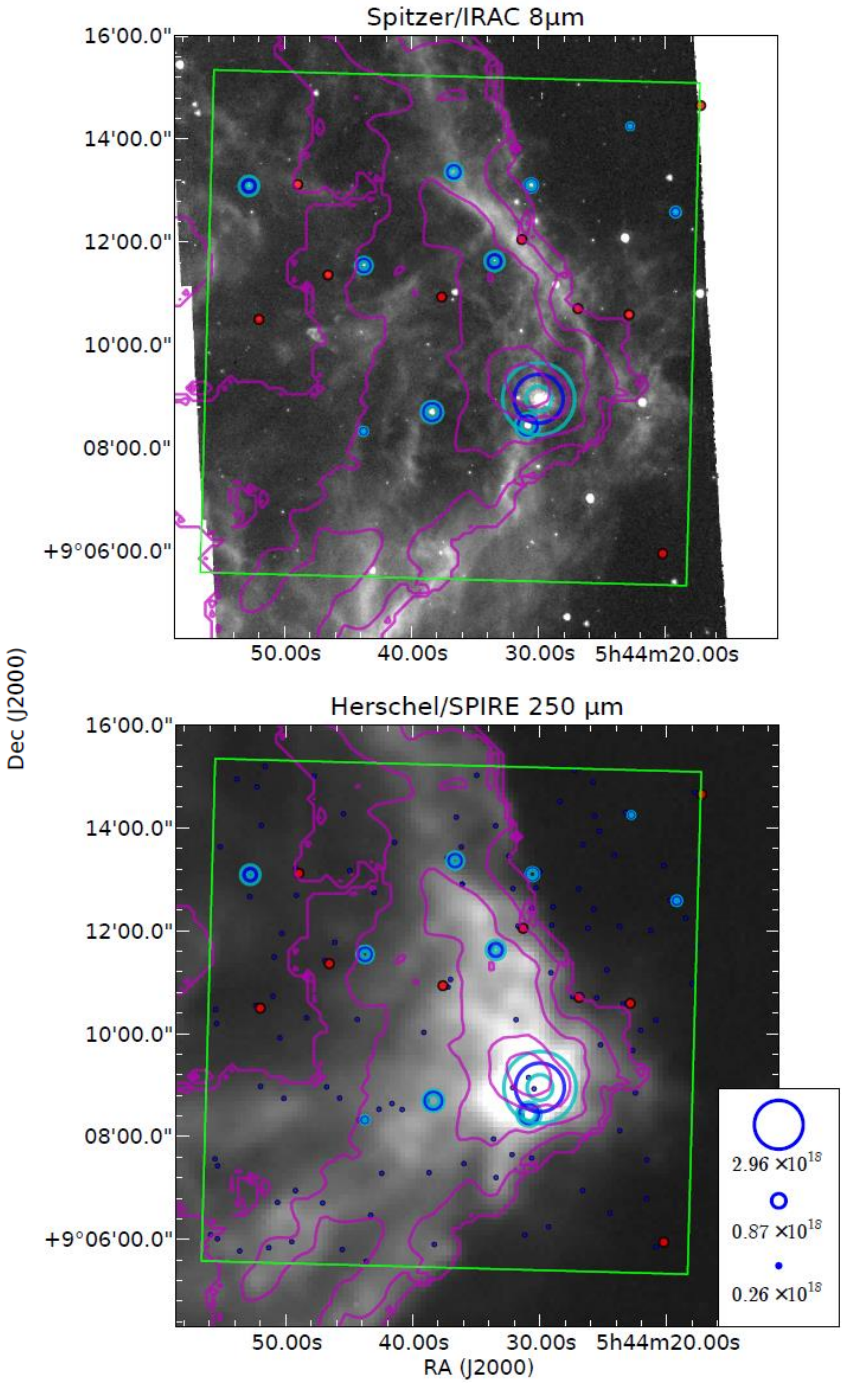

FIGURE 6.4. A combined gas-ice map of B35A overlaid on two background images (Aleksi Suutarinen, *private communication*). Upper: a *Spitzer* IRAC 8 μm map which traces PAHs, as discussed in Chapter 4. Lower: a *Herschel* SPIRE 250 μm map, commonly used to trace cold dust. The dark blue circles are a bubble plot showing ice abundances in the line-of-sight to several background sources; light blue circles indicate the uncertainties. The red dots represent non-detections. Blue dots are locations with insufficient spectral points for analysis. The field of view of the *AKARI* frame is outlined in green. The column density of gas-phase ^{12}CO calculated via its $J = 3 \rightarrow 2$ transition is shown in purple contours with levels from 0 to 5.29×10^{17} cm^{-2} in increments of 1.32×10^{17} cm^{-2}.

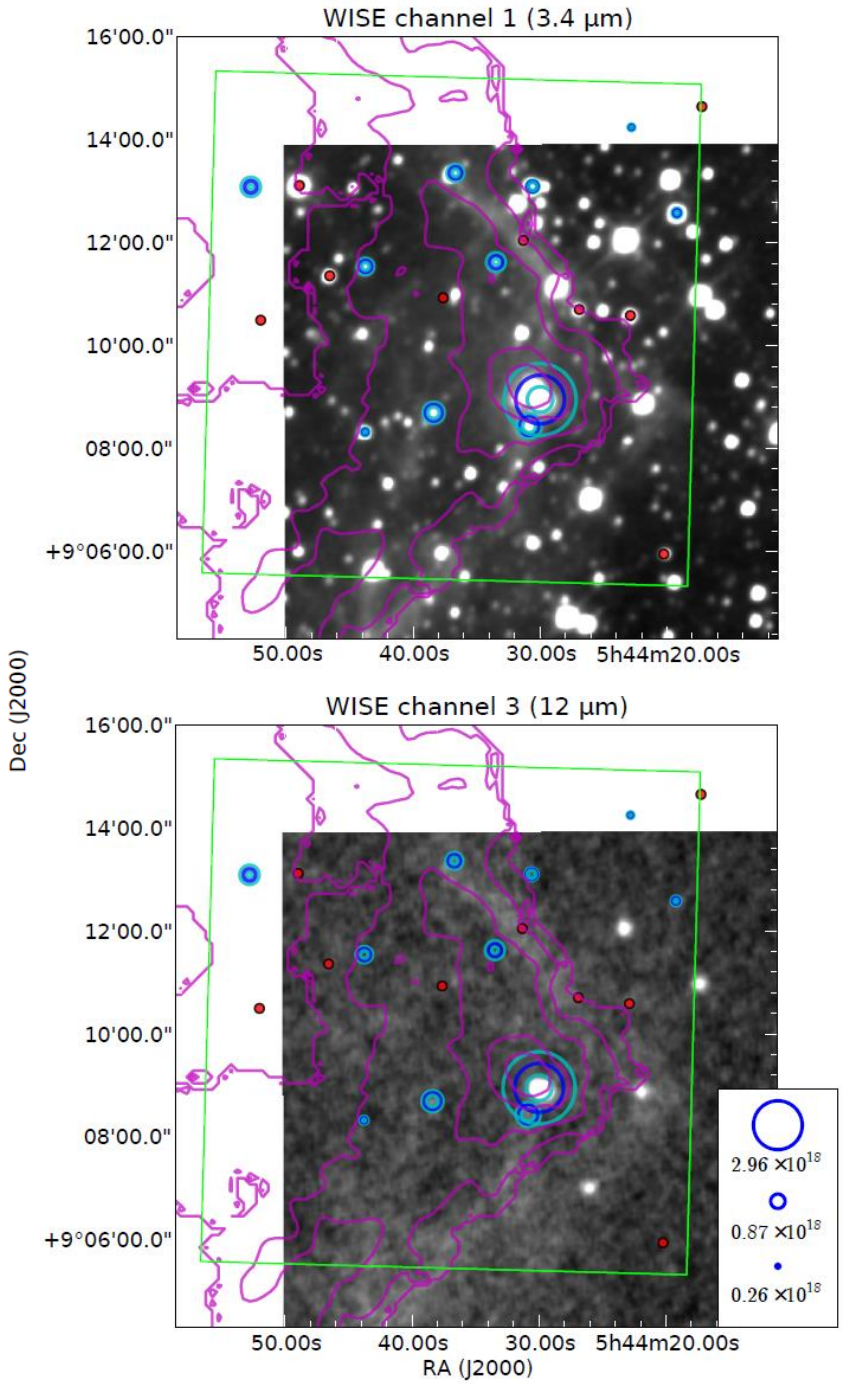

FIGURE 6.4 CONTINUED. A combined gas-ice map of B35A overlaid on two background images (Aleksi Suutarinen, *private communication*). Upper: a *WISE* 3.4 μm map which traces PAHs. Lower: a *WISE* 12 μm map (as used in Fig. 5.11), which traces warm dust, YSO envelopes and disks. The dark blue circles are a bubble plot showing ice abundances in the line-of-sight to several background sources; light blue circles indicate the uncertainties. The red dots represent non-detections. Blue dots are locations with insufficient spectral points for analysis. The field of view of the *AKARI* frame is outlined in green. The column density of gas-phase ^{12}CO calculated via its $J = 3 \rightarrow 2$ transition is shown in purple contours with levels from 0 to 5.29×10^{17} cm^{-2} in increments of 1.32×10^{17} cm^{-2}.

inform modelling of the chemical processes in molecular clouds and protoplanetary disks. This project could also move into the laboratory with experiments to investigate the interactions between the observed molecules.

6.5 CONCLUDING REMARKS

The large CO maps of molecular clouds presented in this thesis are a major step towards the end goal of the gas-solid mapping project. Coupled maps of gas and solid species will inform models of star, disk and planetary system formation and could provide insights into the constituents from which life may form.

REFERENCES

Chini R., 1981, A&A, 99, 346 142

Friesen R. K., Di Francesco J., Bourke T. L., Caselli P., Jørgensen J. K., Pineda J. E., Wong M., 2014, ApJ, 797, 27 140

Noble J. A., Fraser H. J., Aikawa Y., Pontoppidan K. M., Sakon I., 2013, ApJ, 775, 85 144

Suutarinen A., 2015, PhD thesis, The Open University, Department of Physical Sciences, Astronomy Division 144

Thi W., van Dishoeck E. F., Bell T., Viti S., Black J., 2009, MNRAS, 400, 622 141

Visser A. E., Richer J. S., Chandler C. J., 2002, AJ, 124, 2756 142

Wright G. S., Rieke G. H., Colina L., van Dishoeck E., Goodson G., Greene T., Lagage P.-O., Karnik A., Lambros S. D., Lemke D., Meixner M., Norgaard H.-U., Oloffson G., Ray T., Ressler M., Waelkens C., Wright D., Zhender A., 2004, in Mather J. C., ed., Optical, Infrared, and Millimeter Space Telescopes Vol. 5487, The JWST MIRI instrument concept. pp 653–663 140

Thanks to Canelo the fox for keeping me entertained while the IRAM 30 m Telescope was shut down during a very snowy week in the Sierra Nevada mountains.